FIRST-PRINCIPLES CALCULATIONS ON SBA-15 MESOPOROUS SILICA WALL SURFACE FOR SUPPORTED HYDROPROCESSING CATALYSTS

SAÚL PÉREZ BELTRÁN

UNIVERSIDAD INDUSTRIAL DE SANTANDER

FACULTAD DE INGENIERIAS FISICOQUIMICAS

ESCUELA DE INGENIERIA QUIMICA

MAESTRÍA EN INGENIERÍA QUÍMICA

BUCARAMANGA

2015

FIRST-PRINCIPLES CALCULATIONS ON SBA-15 MESOPOROUS SILICA WALL SURFACE FOR SUPPORTED HYDROPROCESSING CATALYST

SAÚL PÉREZ BELTRÁN

Trabajo de Grado Presentado como Requisito para
Optar al Título de Magister en ingeniería Química

Director:

Gustavo Emilio Ramírez Caballero, PhD.

Codirectora:

Sonia Azucena Giraldo Duarte, PhD.

UNIVERSIDAD INDUSTRIAL DE SANTANDER

FACULTAD DE INGENIERIAS FISICOQUIMICAS

ESCUELA DE INGENIERIA QUIMICA

MAESTRÍA EN INGENIERÍA QUÍMICA

BUCARAMANGA

2015

A mis padres y a mi hermano

AGRADECIMIENTOS

A la Universidad Industrial de Santander y a la escuela de Ingeniería Química por ofrecerme la oportunidad de una formación íntegra en el ámbito profesional y personal.

A COLCIENCIAS por el apoyo económico mediante la beca la beca de Jóvenes investigadores.

A los integrantes del Centro de Investigaciones en Catálisis (CICAT) por su apoyo y aportes al desarrollo de este trabajo.

A los integrantes del centro de supercomputación y cálculo científico de la UIS por su disponibilidad y soporte técnico.

Al doctor Gustavo Emilio Ramírez Caballero por su confianza, incondicional apoyo, y orientación durante el desarrollo de este trabajo de investigación.

A la doctora Perla B. Balbuena por la oportunidad de formar parte de su grupo de investigación, por su orientación e incondicional apoyo.

TABLE OF CONTENTS

pág.

LIST OF TABLES

pág.

LIST OF FIGURES

pág.

RESUMEN

TITULO: FIRST-PRINCIPLES CALCULATIONS ON SBA-15 MESOPOROUS SILICA WALL SURFACE FOR SUPPORTED HYDROPROCESSING CATALYSTS*

AUTOR: Saúl Pérez Beltrán**

PALABRAS CLAVE: SBA-15, DFT, Al-SBA-15, Ti-SBA-15, propiedades acidas superficiales

En este trabajo se modela la superficie de la sílica mesoestructurada SBA-15 (Santa Barbara Amorphous No. 15). Se reproducen las principales características estructurales del SBA-15 y la dependencia de la temperatura. Se estudió la incorporación de Al y Ti mediante sustituciones isomorfas y se observó que estas substituciones son energéticamente favorables. La incorporación de Al y Ti provocó distorsiones estructurales que inducen interacciones tipo puente de Hidrogeno en los grupos hidroxilo sobre la superficie. Así se concluye que no solo la estructura electrónica de valencia del Al es importante para modificar la acidez de la superficie, la diferencia en el radio atómico entre el Si y el Al también juega un papel determinante.

Se observó que la distribución de tipos de silanol no influencia la acidez de los grupos hidroxilos de la superficie. Más bien, se observó que las interacciones tipo puente de Hidrogeno entre los grupos hidroxilos y los átomos de O de la estructura inducen un incremento en la fuerza ácida tipo Brönsted, efecto que es favorecido en superficies con un número de silanol mayor.

Se realizaron cálculos de adsorción de clústeres de Pt en superficies con diferentes números de silanol y contenido de Al. La incorporación de Al no modificó el mecanismo de enlace Pt-O. Las superficies con un número mayor de silanol facilitaron una distribución más uniforme de los clústeres en la superficie, lo que se atribuyó a la disponibilidad de una mayor cantidad de grupos hidroxilos en las superficies modificadas. El valor promedio del número de coordinación de los átomos de Pt se redujo, comportamiento similar que se observó con el valor promedio de la distancia interatómica Pt-Pt. Finalmente se realizaron cálculos de transferencia de carga electrónica entre la superficie y clúster, observándose una distribución no uniforme en los clústeres adsorbidos.

---

*Trabajo de investigación de Maestría en Ingeniería: Área Ingeniería Química

** Facultad de Ingenierías Físico Químicas, Escuela de Ingeniería Química. Director: Gustavo Emilio Ramírez Caballero, Ph.D. Directora: Sonia Azucena Giraldo, Ph.D. .

ABSTRACT

TITLE: FIRST-PRINCIPLES CALCULATIONS ON SBA-15 MESOPOROUS SILICA WALL SURFACE FOR SUPPORTED HYDROPROCESSING CATALYSTS*

AUTHOR: Saul Perez-Beltran**

KEYWORDS: SBA-15, PBC-DFT, Al-SBA-15, Ti-SBA-15, acidic properties.

Theoretical modeling of internal pore surfaces of the mesostructured silica material SBA-15 (Santa Barbara Amorphous No. 15) was addressed. The main structural features of the SB5-15's pore surface are and the temperature dependence are reproduced. Modeling of Al and Ti incorporation through isomorphic substitutions is performed. In both cases it was found that isomorphic substitutions are energetically favorable. Besides the creation of bridging hydroxyl groups with strong Brönsted acid properties, the Al and Ti incorporation also generates local structural distortions inducing additional H-bond interactions between surface hydroxyl groups and framework O atoms. From this it was concluded that not only the Aluminum electronic valence is relevant for changing the surface acidity properties, the differences in atomic radius also played an important role

It is observed that surface's chemical environment does not influence the acidity strength of surface hydroxyl groups. Rather, it was noticed that H-bond interactions between hydroxyl groups and surface O atoms strongly lowers the OH-stretching frequencies of surface hydroxyl groups, which indicate an increase in Brönsted acidity strength. This local effect was favored on surfaces with higher silanol number.

Adsorption calculations of Pt clusters on surfaces with varying degrees of silanol number and Aluminum content were also performed. Improvements on active phase dispersion after Al incorporation were better on surfaces with higher silanol number. Moreover, Al^{3+} incorporation did not changed the Pt-O bonding mechanisms. Rather, the improvement in Pt dispersion was attributed to the availability of bridging hydroxyl groups after isomorphic substitutions. In all cases we observed that after adsorption the average coordination number of Pt cluster was lowered, and the average Pt-Pt distance was reduced as the number of Pt-O bonds increased. Calculations of total electronic charge transfer between the surface and cluster were also performed; it was observed a non-uniform electronic distribution throughout the cluster.

---

*Thesis to obtain the Master degree of Engineering, Field: Chemical Engineering.

**Faculty of Physical-Chemical Engineering, Department of Chemical Engineering. Advisor: Gustavo Emilio Ramirez-Caballero, Ph.D. Coadvisor: Sonia Azucena Giraldo-Durate, Ph.D.

INTRODUCTION

Nowadays the petroleum industry faces more stringent requirements concerning the transportation fuels.[1-3] The quality of crude oil supply continuously diminish without feasible expectations to find new reserves of light crude oil, and the new environmental regulations require even lower content of sulfur and aromatics.[2, 4] In order to overcome these issues, the petroleum industry needs to improve the overall performance in its processes while saving still more energy, and also needs to achieve a better balance on the various hydroprocessing (HPC) reactions taking place. A better balance means higher conversions and selectivity to more valuable fractions while using less energy and more durable catalysts.

The interest in improve the overall performance in HPC reactions includes removal of heteroatoms, saturation of unsaturated compounds and cracking of long hydrocarbon molecules.[2, 5] The removal of heteroatoms and saturation of unsaturated compounds implies hydrogenolysis of carbon-heteroatom bonds, including reactions of hydrodesulfurization (HDS), hydrodenitrogenation (HDN), hydrogenation (HYD), and hydrodemetallation (HDM).

The catalyst deactivation is severe in HPC reactions of heavy oils.[6] In case of light oils, the commercial HPC catalysts present minimal deactivation and can operate for long periods before replacement. However, this situation changes because of the larger content of heteroatoms, asphaltene, paraffin and nitrogen compounds that heavy oils have. The current commercial catalysts based on alumina or zeolites suffer of severe limitations when large reactant molecules are involved.[4, 7-8] The pore channel structure is blocked and coke formation is promoted[9]. Attempts to improve the diffusion of reactants in these catalysts include use of high temperatures in order to enhance the desorption process, especially at the end of catalyst life,[2] however, the thermal and non-catalytic cracking is also favored and selectivity to more valuable liquid fractions is lost.

Current research efforts are focused on the enlargement of support's pore sizes into the mesoporous range, allowing larger molecules enter to the pore system to be processed, and to leave the pore system again.[9-10] The intensive work in ordered mesoporous materials can be traced to 1992, when scientists working for Mobil Oil Corporation synthesized and characterized a novel type of silica with a highly ordered hexagonal array of unidimensional pores and narrow pore size distribution (MCM-41 material).[9, 11] The discovery of this material was a breakthrough in materials engineering. Since then, an impressive progress in development of many other mesoporous silica materials is observed. Some of them are the MCM-48,[12] the MCM-50,[9] the HMS (Hexagonal Mesoporous Silica),[13] the MSU (Michigan State University material) and the SBA-15 (Santa Barbara amorphous No. 15).[14-16]

Besides the enlargement of size in pore structure, the feasibility of a new material as support for HPC catalysts depends on mechanical stability and hydrothermal stability.[4, 17] Mechanical stability of mesoporous materials is little influenced by the type of structural arrangement and can be considered sufficient for application in HPC catalysts. However, hydrothermal stability strongly depends on the wall thickness of pore structure and the degree of silica polymerization; a thicker wall means better hydrothermal stability.[9] Good compromise between wall thickness, pore size and specific surface area must be achieved for a successful use of mesoporous silica materials for HPC catalysts.

The SBA-15 material presents elevated hydrothermal stability and suitable textural properties for HPC catalysts.[15] The SBA-15 wall thickness has been measured between 3 and 5 nm, whereas other materials like the MCM-41, the MCM-48, the HMS, and the FSM-16 have an average wall thickness of 1.01 nm.[15, 17] Moreover, the SBA has specific surface area ranging between 690 and 1040 m^2/g, and a narrow pore size distribution with average pore diameter tunable between 5 and 30 nm. [9, 18] For these reasons, SBA-15 has been envisioned as a promising material for a new generation of HPC catalysts designed to handle heavy oils feeds.

Several works remark the potential of SBA-15-based mesoporous systems as supports for HPC catalysts.[19-22] NiW and NiMo supported on SBA-15 were proposed as catalysts with larger pore diameter and higher surface area than molybdenum-based hydroprocessing catalysts supported on γ-Al_2O_3.[21] For CoMo/Ti-SBA-15 catalysts it is reported that supported metal oxides only induce a minimal blocking of the host pore system.[23] For FeW/SBA-15 HPC catalysts it was found that pore diameters of 10 Å keeps a good compromise between diffusion of reactants and active phase dispersion. Supported NiMo catalysts on unmodified and Al modified SBA-15 were tested and compared with commercial catalysts for the hydrogenation of heavy oil derived from coal liquefaction process; it was found that catalysts supported on SBA-15 have the largest pore system and HDN and HDS activities for upgrading the heavy oil.[24] The effect of Al^{3+} and Ti^{4+} incorporation on catalytic activity of these catalysts was evaluated in the HDS of dibenzothiophene and biphenyl hydrogenation, and it was found that Al^{3+} and Ti^{4+} incorporation have an enhancement effect on surface acidity properties and dispersion of supported species.[21] From the differences in performance between catalysts supported on unmodified and modified SBA-15, it is observed that HPC catalysts based on pure siliceous SBA-15 suffer of poor catalytic activity,[4] which is attributed to the lack of Brönsted acid sites that pure SBA-15 have. The need of strong Brönsted acid sites on the SBA-15's surface is because they are the primary seat of catalytic activity in transformations of hydrocarbons.[25]

Several experimental works trying to enhance the population of surface Brönsted acid sites of the SBA-15 by isomorphic substitution of Si^{4+} atoms by Al^{3+} and Ti^{4+} atoms have been reported so far.[4, 17] Better active phase dispersion and better catalytic performance of HPC catalyst have been reported after incorporation of Al^{3+} and Ti^{4+}.[21, 23, 26] The Al^{3+} incorporation into the SBA-15 framework has been associated with creation of Bridging hydroxyl groups with strong Brönsted acid properties, whereas better adsorption properties has been associated with Ti^{4+} incorporation because of the presence of 3d electronic orbitals.[27]

The quantification of surface Brönsted acidity in SBA-15 materials has been performed by spectroscopic measurements after adsorption of probe molecules or by TPR-NH_3 profiles (Temperature Programed Reduction).[21] In case of Al^{3+} incorporation at an Al/Si ratio of 1/20, the spectroscopic measurements after pyridine adsorption indicate creation of Brönsted acid sites. In case of Ti^{4+} modified SBA-15, the TPR-NH_3 profiles suggest an increase in total acidity, which was correlated with better dispersion of NiMo and NiW phases and better catalytic activity for both HYD of biphenyl and HDS of dibenzothiophene. From this and other similar works,[4] it is observed that enhancements in surface acidity properties and better catalytic activities of SBA-15-based HPC catalysts have been indirectly quantified by using experimental techniques. To the best of our knowledge, no theoretical description of surface structural distortions and surface acidity properties after isomorphic substitution of Si^{4+} atoms by Al^{3+} and Ti^{4+} has been developed. No elucidation of the effects of these isomorphic substitutions on active phase – support interactions has been addressed.

Development of atomic level explanations for Brönsted acid properties of the SBA-15 is important for achieving a rational design of novel supported HPC catalysts. Nowadays, the computational methods have proved to be effective for understanding the surface chemistry at atomic level, providing a theoretical based interpretation of experimental results and even generating information that most of time is experimentally difficult or even impossible to obtain. [28-29] Molecular dynamics (MD) and density functional theory (DFT) have been successfully used for modeling catalytic surfaces and here these methods are envisioned for obtaining an explanation of the effect of isomorphic substitutions of Si^{4+} by Al^{3+} and Ti^{4+} in the SBA-15 framework.[30] Moreover, modeling of metal-support interactions before and after isomorphic substitutions is also addressed. The information obtained by using this approach is useful for pursuing a successful implementation of HPC SBA-15-based catalysts.

The MD and DFT methods have been used in a complementary way for modeling the inner pore surface of the SBA-15. The MD calculations were performed using the Universal Force Field (UFF) potential as implemented in AVOGADRO code,[31] whereas the DFT calculations were performed using Vienna Ab-initio Simulation Package (VASP).[32-34] For the DFT calculations, the generalized gradient approximation proposed by Perdew-Burke-Ernzerhof (GGA-PBE) is used for the exchange-correlation functional approximation.[35] A flat slab model with periodic boundary conditions (PBC model) was used for modeling the inner pore surface of the SBA-15. Modeling of the entire mesoporous channel was considered computationally expensive and is disregarded based on the assumption of absence of diffusional limitations and confinement effects.[27, 32] Using of a PBC model facilitated the control of basis set convergence and eliminates the need of artificial saturation of dangling bonds.[36] Moreover, an adequate representation of density and type of surface silanol groups (isolated, geminal, or vicinal) was facilitated,[37-39] being crucial for a representative study of Brönsted acidity properties.[36] Surface silanols (-Si-OH) are classified as isolated, geminal, and vicinal. A single OH group on a Si atom is an isolated silanol. Geminal silanols refer to two OH groups bound to the same Si atom, whereas vicinal silanols are those OH groups involved in H-bond interactions (either single or geminal).[37, 40]

The temperature dependence of silanol number (the number of silanol groups per unit area) is taken into account because this factor strongly influences the distribution and reactivity of surface silanol groups.[41] The OH-stretching frequency calculations are used for quantifying the acidity strength of surface silanol groups and bridging hydroxyl groups created upon Al^{3+} incorporation. The adsorption of a Pt-cluster is addressed in order to evaluate the effect of surface modification at two different temperatures, before and after modification with Al atoms.

It is demonstrated that a flat film with periodic boundary conditions can accurately represent the SBA-15's surface. This work contributes in proposing the use of PBC models for modeling the framework of mesoporous silica materials. The

advantages of this approach are evidenced in an adequate modeling of silanol type distribution, which determines the surface reactivity of amorphous silica. The temperature dependence of silanol number and silanol type distribution has been taken into account.[40] It is suggested that surface's chemical environment (the surface silanol type distribution) does not influence the acidity strength of surface hydroxyl groups. Isomorphic substitutions of Si atoms by Al or Ti atoms were found to be energetically favorable. However, we observe that both Al and Ti incorporation become increasingly less favorable as the Al/Si or Ti/Si ratios increase. Preferential sites for isomorphic substitution are identified for both Al and Ti species. Moreover, we noticed that differences in atomic size between Si atoms and Al or Ti atoms contribute to changes in surface acidity.

The adsorption calculations of Pt clusters on surfaces with varying degrees of silanol number and Al content were useful to infer that improvements on active phase dispersion after Al incorporation are better achieved on surfaces with higher silanol number. Al incorporation does no change the Pt-O bonding mechanisms. Rather, the improvement in Pt dispersion is mainly due to the availability of bridging hydroxyl groups after isomorphic substitutions. Significant charge depletion in Pt atoms around the cluster-silica interface was observed.

In all cases we observed that after adsorption the average coordination number of Pt cluster was lowered. Moreover, the average Pt-Pt distance was reduced as the number of Pt-O bonds increases, with the subsequence dependence of total electronic charge transfer between the Pt cluster and the surface.

1. BACKGROUND

A detailed understanding at atomic level of surface chemistry of SBA-15's inner pores is important for a rational design of novel supported HPC catalysts. Nowadays, computational methods are an effective way to understand surface chemistry at atomic level. The computational modeling provides a theoretical based interpretation of experimental results and also generates information that most of time is experimentally difficult or even impossible to obtain.[28, 42]

This chapter is intended to facilitate an accurate modeling of the inner pore surface of SBA-15. It is organized as follows: Section 2.1 presents details about the synthesis and characterization of the SBA-15, which is helpful for supporting the assumptions and findings of this work, whereas section 2.2 discusses earlier works on theoretical modeling of mesostructured silica materials, giving relevant insights for building a representative model for the inner pore surface of the SBA-15.**Synthesis and characterization of the SBA-15**

1.1.1 Synthesis procedure

The synthesis procedure of the SBA-15 remains almost invariant since its first publication.[15] Changes in morphology and textural properties can be induced by varying physical (aging and calcination temperatures, stirring conditions, and time elapsed in each step) and chemical parameters during synthesis (pH synthesis, silica source/surfactant ratio).[18, 43-45] However, concerning the nature and content of silanol groups, it is reported that most of differences are erased during the aging and calcination steps.[46]

The two main components for synthesis are the template and the silica source. The triblock copolymer ($PEO_{20}PPO_{20}PEO_{20}$) is used as the structure directing agent, whereas the tetraethyl orthosilicate (TEO) is the silica source.[15] The first synthesis step (ripening step) starts by mixing the two components at constant temperature (300 - 320 K) and strong acidic conditions (pH ~ 1). Then, the mixture is transferred to an oven for aging at 363 K for 24 h (second synthesis step). After

this, filtration and washing with distilled water is applied at 343 K for 48 h, and finally, for the third synthesis step, the template remotion is performed by calcination at 770 K for 4 h.

The enhancement of surface acidity properties of the SBA-15 requires of isomorphic substitutions of Si^{4+} by different cations (Al^{3+}, Ti^{4+}, Zr^{4+}, etc).[4] Isomorphic substitutions are achieved by using direct or post-synthesis methods.[4] The effectiveness of each method depends on the atomic specie to be incorporated. Incorporation of Al^{3+} atom is better achieved by post-synthesis methods; direct Al^{3+} incorporation is difficult because the high acidity required for the creation of the mesoscopic structure, whereas better Ti^{4+} incorporation is obtained via direct synthesis procedure. Details about incorporation of Al^{3+} and Ti^{4+} are given in following sections.

1.1.2 Textural properties of SBA-15

The mesoporous structure and other textural properties of the SBA-15 are measured using low- and wide-angle XRD, N_2 adsorption/desorption isotherms, and CO_2 chemisorption measurements, among others.[15, 18, 23 46] In general, it is reported that SBA-15 has a mesoscopic structure with a *p6mm* hexagonal symmetry,[15] a specific surface area ranging between 690 - 1040 m^2/g,[14, 46] a narrow pore size distribution with average diameters tunable between 5 nm and 30 nm, [14] and a pore wall thickness of approximately 5 Å.[15, 17-18] The pore wall thickness of the SBA-15 gives to this material improved mechanical stability and hydrothermal resistance, in comparison with other mesoporous materials like the MCM-41.[17]

The specific surface area and the average pore diameter are the key factors for placing the SBA-15 as a suitable support for catalysts with high diffusion rates for large molecules.[22] For CoMo/Ti-SBA-15 catalysts, it is reported that supported metal oxides only induce a minimal blocking of the host pore system.[23] For FeW/SBA-15 HPC catalysts, it was found that pore diameters of 10 Å keeps a

good compromise between diffusion of reactants and active phase dispersion.[16] Supported NiMo catalysts on unmodified and Al modified SBA-15 were tested and compared with commercial catalysts for the hydrogenation of heavy oil derived from coal liquefaction process; it was found that catalysts supported on SBA-15 have the largest pore system and HDN and HDA activities for upgrading the heavy oil.[24] NiW and NiMo supported on SBA-15 were proposed as catalysts with larger pore diameter and higher surface area than molybdenum-based hydroprocessing catalysts supported on γ-Al_2O_3.[21] The effect of Al^{3+} and Ti^{4+} incorporation on catalytic activity of these catalysts was evaluated in the HDS of dibenzothiophene and biphenyl hydrogenation. The Al^{3+} and Ti^{4+} incorporation have a direct effect on the surface acidity properties of the support and dispersion of supported species. Better catalytic performance for HDS and HYD reactions was measured for these modified supports, whereas lower catalytic performance was measured on the unmodified supports.

From the above it is observed that catalysts based on unmodified SBA-15 suffer of poor catalytic activity. This is because of the SBA-15 has an electronically neutral framework lacking of Brönsted acid sites.[4] In that sense, any successfully use of the SBA-15's textural properties relies on the improvement of the SBA-15's acidity properties.

The motivation of this work relies on understand the effect of isomorphic substitutions on the SBA-15's surface acidity properties. Hence, hereafter we are focused on reviewing data relevant for building adequate atomistic model for SBA-15's inner pore surface. The absence of diffusional limitations and confinement effects is assumed in our SBA-15 surface model because the observed pore diameter and high diffusion rates in SBA-15-based catalysts,.[4, 17]

1.1.3 SBA-15's wide-angle XRD diffraction patterns

Low angle XRD (X-Ray Diffraction) patterns are useful for measuring the mesoscopic structure of the SBA-15,[47] whereas the wide angle XRD patterns are

useful for determining the structural ordering of the SBA-15's framework.[23] The **¡Error! No se encuentra el origen de la referencia.**-a shows the wide angle XRD pattern of Mo (8 wt.%) catalysts supported on SBA-15 loaded with ZrO_2 (a - d; 10 - 50 wt.%).[48] The existence of an unique and broad peak between 15º and 35º 2θ degrees for all compositions of ZrO_2 confirms the amorphous nature of the SBA-15's framework, and also suggests high dispersion of Mo and ZrO_2 phases. The **¡Error! No se encuentra el origen de la referencia.**-b shows the wide angle XRD pattern for several noble metals supported on SBA-15 and SBA-15 modified with Al (Al-SBA-15).[49] Once again the framework's amorphous structure of the SBA-15 is observed even after modification with Al^{3+} and loading of noble metals. No Pt peaks were observed in the Pt/Al-SBA-15 system, whereas sharp peaks of Pt were observed in the Pt/SBA-15 system, which is an indicative that Pt particles are loaded with high dispersion only in the former case. Other works with NiMo and NiW catalysts supported on SBA-15, Al-SBA-15, and Ti-SBA-15 also suggest an amorphous arrangement of the support's framework even after modification.[50-52]

Figure 1: a: 1) 8%Mo-10%ZrO2-SBA-15; 2) 8%Mo-25%ZrO2-SBA; 2) 8%Mo-35%Zr-SBA; 4) 8%Mo-50%ZrO2-SBA. b: 1) Al-SBA-15; 2) Rh/Al-SBA-15; 3) Pd/Al-SBA-15; 4) Ru/Al-SBA-15; 5) Pt/Al-SBA-15; 6) Pt/SBA-15.

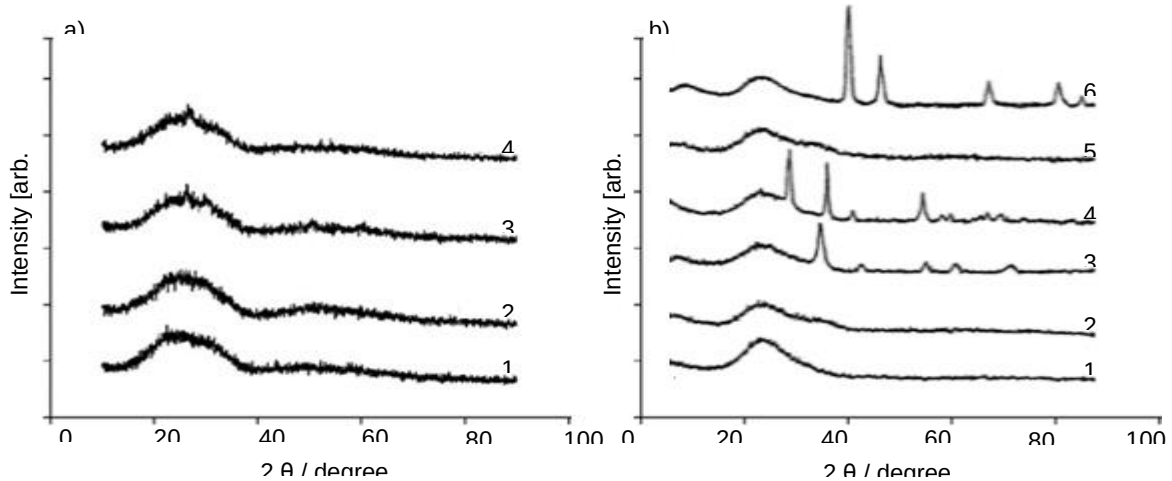

1.1.4 Acidic properties of unmodified and modified SBA-15

The SBA-15 in its pure siliceous form has an electronically neutral framework and lacks of Brönsted acidity sites,[4, 17] which hinders its use as catalytic support because strong Brönsted acids are the primary seat of catalytic activity for transformation of hydrocarbons.[25] Enhancements in population of Brönsted acid sites of SBA-15 have been associated with better dispersion of active phases[26] and better catalytic activity for HDS, HYD, and HDN reactions.[21, 26, 49, 53] Experimental works addressing the isomorphic substitution of Si^{+4} by Al^{3+}, Ti^{3+}, Zr^{4+}, Ce^{+4} have been reported.[4, 17] and improvements in catalytic performance of HPC catalysts supported on SBA-15 have been reported after support modification by incorporation of Al^{3+} and Ti^{4+}.[21, 23, 26] In this section we focus on reviewing the isomorphic substitutions of Si^{4+} by Al^{3+} and Ti^{4+}.

The incorporation of Al^{3+} and the subsequent protonation of an O atom bonded to the Al^{3+} atom give rise to bridging hydroxyl groups with stronger Brönsted acidity than isolated silanol groups,[30, 54] whereas the Ti^{4+} incorporation has been associated to an enhanced dispersion of supported active phases, which is in turn related to improvements of support's Brönsted acidity.[21]

Al^{3+} incorporation

The incorporation of Al^{3+} into the SBA-15 framework is better achieved by post-synthesis grafting with basic pH.[26, 49, 52, 54-55] The direct synthesis procedure usually ends in leaching of Aluminum incorporation into octahedral sites without observable enhancements in Brönsted acidity.[19, 56-57] Examples of precursors for post-synthesis grafting are aluminum isopropoxide in non-aqueous solution[54],[26] anhydrous aluminum chloride,[52, 55] or ammonium hexafluoroaluminate.[58]

Al-SBA-15 supported NiMo catalysts were prepared using the post-synthesis procedure with ammonium hexafluoroaluminate.[53] The creation of Brönsted acid sites for Al^{3+} incorporation at an Al/Si ratio of 1/20 was corroborated by pyridine adsorption; the appearance of a band at 1545 cm^{-1} and 1639 cm^{-1} in the IR

spectrum suggested the creation of strong Brönsted acid sites. Better catalytic properties for catalysts supported on Al-containing samples was evidenced by a higher S and N conversion in hydrotreating of heavy gas oil.

NiW/Al-SBA-15 catalysts were prepared using the post-synthesis procedure with aluminum isopropoxide. In this study the Al/Si ratio was varied between 1/15 and 1/30 and the catalytic activity was evaluated in the HDS of 4,6-DMDBT. The IR spectrum for pyridine adsorption experiments evidences the formation of Brönsted acid sites on the Al-SBA-15 samples. Better dispersion of metallic phase in Al-SBA-15 supports was also evidenced by HRTEM experiments. The enhanced catalytic activity of NiW/Al-SBA-15 supported catalysts was attributed to the formation of Brönsted acid sites and higher dispersion of WS_2 phase. The effect of increasing the Al content was not clarified.

The effect of Si/Al ratio in Al-SBA-15 prepared by the post-synthesis method using aluminum chloride was studied for the HDS of 4,6-dimethyldibenzothiophene (4,6-DMDBT) with supported NiMo catalysts.[52] Al/Si ratios of 1/50, 1/30, 1/20 and 1/10 were prepared and it was observed that tetrahedrally coordinated Al^{3+} cations predominated over those octahedrally coordinated; however, ^{27}Al MAS-NMR measurements revealed that the proportion of latter ones increased as the Al content was increased. Changes in population of Brönsted acid sites was measured by the IR spectrum of pyridine adsorbed; as the Al/Si increases, the intensity of bands at 1546 cm^{-1} and 1639 cm^{-1} also increases, indicating formation of Brönsted acid sites. Moreover, it was also found that Brönsted acid sites density decreases with thermal treatment.

Ti^{4+} incorporation

The Ti^{4+} is isovalent with the Si^{4+}, then protonation of an adjacent O is not expected. However, it is reported that the presence of 3d orbitals in Ti^{4+} cations could induce different adsorption properties on the surface.[59] In comparison with the Al^{3+} incorporation, the Ti^{4+} incorporation into mesoporous siliceous materials is

better achieved via direct synthesis procedure.[60] Typical precursors are titanium isopropoxide and titanium ethoxide.[61]

The catalytic activity for the HDS of dibenzothiophene and the HYD of biphenyl was evaluated for NiMo and NiW catalysts synthesized over Ti-SBA-15.[21] The ^{29}Si NMR measurements indicate that Ti incorporation into the SBA-15 framework was complete. Measured with TPD-NH_3, the total surface acidity of pure siliceous SBA-15 was 0.32 mmol NH_3/g_{cat}, whereas the for Ti-SBA-15 material, with a Ti/Si ratio of 1/40, the total acidity was 0.45 mmol of NH_3/g_{cat}. The increase in total acidity was attributed to an increase in population of Brönsted acid sites with medium and strong acidity. A correlation between support acidity and dispersion of supported species was found by H_2-chemisorption measurements, and it was determined that dispersion of supported phase on the SBA-15 was a function of surface acidity.

The desulfurization of dibenzothiophene was evaluated for CoMo catalysts supported on Ti-SBA-15.[23] The Ti^{4+} incorporation was performed by direct synthesis procedure using titanium butoxide at Ti/Si ratios of 1/80, 1/60, 1/40 and 1/20. The textural properties of the SBA-15 were preserved regardless the Ti/Si ratio. Moreover, after catalyst deposition a minimal pore blocking of the host pore systems was measured. For all Ti/Si ratios it was found that Ti incorporation provides better dispersion of the oxide and sulfide metal species, favoring the sulfidation of cobalt species. The TPR technique (Temperature Programed Reduction) was used for measure the effect of Ti incorporation on metal-support interaction and type of Co and Mo species formed. Regardless the Ti content, all the catalysts presented similar TPR profiles, which indicates that formed Co/Mo species are similar for all the catalysts and hence, Ti-incorporation do not involves significant changes in the metal-support interaction. However, the catalysts supported on Ti-SBA-15 reported more HDS activity, especially in those materials with a Ti/Si ratio lower than 1/60.

1.1.5 Noble metals supported on SBA-15

Noble metals have been potentially envisioned as new HDS supported catalysts for petroleum feedstocks.[62-64] Several noble metals supported on SBA-15 and Al-SBA-15 (Al/Si=1/15) have been prepared using the impregnation method with metal chloride aqueous solutions of H_2PtCl_6-$6H_2O$, $PdCl_2$, $RhCl_3$-$3H_2O$, and $RuCl_3$-$3H_2O$. Each of these catalysts has been tested for the HDS of thiophene at 623 K under 0.1 MPa. It was found that catalytic activity strongly depends on the kind of noble metal, being the Pt catalyst the most active. Moreover, the Pt catalyst also showed higher catalytic activity than commercial $CoMo/Al_2O_3$ catalysts. The catalytic activity was higher when supported on Al-SBA-15 than when supported on SBA-15. The Pt/Al-SBA-15 catalyst has high sulfur-tolerant properties, similar Pt catalysts supported on FSM-16 and MCM-41. Wide-angle XRD measurements indicate that Pt particles supported on Al-SBA-15 were highly dispersed, whereas the Pt supported on SBA-15 was loaded with large particle size. The differences in dispersion of Pt were associated with the high acidity properties of Al-SBA-15 material. However, a clear explanation about the Pt/Al-SBA-15 interaction was not given. The effect of Brönsted acid sites on morphology of Pt particles and hence of the catalytic activity is still unknown.

1.2 Theoretical modeling of mesostructured silica materials

A representative model for the inner pore surface of the SBA-15 is required for a theoretical elucidation of surface structural distortions and surface acidity properties after isomorphic substitution of Si^{4+} by Al^{3+} and Ti^{4+}, besides the understanding of metal-support interactions before and after modification.

The early modeling of mesoporous silica materials was focused in using molecular dynamics (MD) for studying the effect of changing the lattice constants and wall thicknesses on the stability of MCM-41 materials,[65] which was helpful for obtaining information concerning the density of tetrahedral sites, the concentration of silanols, and the distribution of ring sizes. Information regarding the relationship between pore size and wall thickness, useful for obtain catalytic supports without

diffusional limitations and hydrothermal stability, was also obtained. It was elucidated that structures formed with smaller micelle templates require thicker walls to achieve thermodynamic stability. Moreover, it was demonstrated that models with periodic boundary conditions (PBC models) are representative models of amorphous surfaces as long as the unit cell dimensions are much larger than the interatomic distances.

MD calculations have been also applied for other mesoscopic materials like MCM-41, MCM-48 and SBA-15.[66] Different assumptions have been used for each material. The MCM-41 is described as a regular cylindrical silica nanopore, whereas SBA-15 is modeled as cylindrical nanopores connected through lateral channels. These models were successful to generate information related with the mesoscopic structures (e.g., simulation of adsorption-desorption isotherms, diffusion of molecules inside the pore structure, etc...), however, nothing was mentioned about modeling of surface acidity and surface reactivity.

1.2.1 Representative models for the inner pore surface of mesoscopic materials

The density functional theory (DFT) method has been used for modeling mesoporous materials.[27, 47, 67] However, in comparison with molecular dynamics, the DFT method is not intended for studying mesoscopic features of silica based materials; rather the DFT is oriented to obtain information about the surface electronic distribution and its effect on local phenomena such as adsorption of molecules or clusters on specific sites and calculation of energy barriers.[58, 68] The number of atoms that DFT can handle is by far less than the number of atoms involved in molecular dynamics simulations,[37, 40] so it has been used only for flat film models representing the inner pore surface.[27, 47, 67]

The DFT method was used for modeling the internal walls of *p*-phenylenesilica and its interaction with CO, CO_2, and CH_4.[27] The *p*-phenylenesilica is a hexagonal mesoporous material with a lattice constant of 52.8 Å, a pore diameter of 38 Å, and

pore walls consisting of alternated organic and inorganic layers connected by Si-C bonds. The model representing the internal walls was constructed using periodic boundary conditions. Adsorption energies comparable with experimental data were calculated for each molecule (CO 14.3 kJ/mol, CO_2 13.3 kJ/mol, CH_4 9.2 kJ/mol) and preferential adsorption sites were identified. This work is an example of DFT use for modeling surface properties of mesoporous materials without reproducing the entire pore system, only flat films are enough for representing the internal pore surface.

DFT calculations have been already performed for the elucidation of SBA-15's surface properties.[47] Several cluster models with one and two silica rings of different sizes were used for modeling the amorphous nature of the SBA-15 framework. The Si-O bond lengths, the O-Si-O and Si-O-Si bond angles, and the IR spectrum for each model were calculated and compared with experimental data of amorphous silica. Structural details about the SBA-15 framework were inferred after comparison of each model with experimental data. The ring size distribution was determined as follows, from the most to the less common: 6-, 5-, 7-, 8-, 4-membered silica rings; with the 6-, and 5-membered rings as the main structural elements.[67] However, none of these models were able to reproduce the density and type distribution of silanol groups, neither the temperature dependence of silanol groups.[41]

A DFT PBC model of an amorphous silica surface with periodic boundary conditions was constructed by cutting a slab from an amorphous silica bulk model previously generated using classical molecular dynamics.[37] After the cleavage and before DFT optimization, the under-coordinated Si atoms on the surface were saturate with hydroxyl groups giving a silanol number of 5.9 OH/nm^2. Besides the experimental ring size distribution, the distribution of Si-O-Si and O-Si-O angles, and the Si-O bond lengths; this PBC model was able to reproduce the silanol density and the silanol type distribution (isolated, associate, geminals). Moreover, this model also meets the condition for modeling amorphous surfaces using

periodic models because the unit cell dimensions of about 13 Å x 17.5 Å x 25 Å are much larger than the interatomic distances Si-O of 1.63 Å.[69] However, nothing is mentioned about the temperature dependence of silanol number,[41] this model is representative only for fully hydroxylated surfaces; it is not able to reproduce partially dehydroxylated silica surfaces.

The temperature dependence of silanol content has been already addressed by using DFT PBC models.[40] A hydroxylated amorphous silica film of approximately 300 atoms was constructed in a similar fashion than the above mentioned case.[37] A thermodynamic-based approach was implemented by combined use of classical molecular dynamics and density functional theory.[40] The following section gives details about the protocol used for simulate the dehydroxylation process as a function of temperature.

1.2.2 Amorphous silica surfaces: Modeling of temperature vs. silanol number

The silanol number decreases as a temperature increases until the silica surface becomes completely dehydroxylated at 1373 K.[41] At approximately 463 K all the physisorbed water is removed and only silanol groups remain on the surface; above 463 K these silanol groups begin to react each other through condensation reactions where siloxane bridges and water are formed.[40] **¡Error! No se encuentra el origen de la referencia.** shows the experimental data of silanol number vs. temperature for 16 silica samples with different synthesis procedures and structural characteristics.[41] It is worth to note that all samples exhibit a similar dependence, following the same pattern for the range of temperatures evaluated. At 673 K the flattening in slope is attributed to an increase in dehydroxylation activation energy due to the requirement of proton mobility for condensation of isolated silanol groups.

Figure 2: Temperature vs. Silanol number for 16 different SiO2 samples. The dotted lines delimit the experimental data.

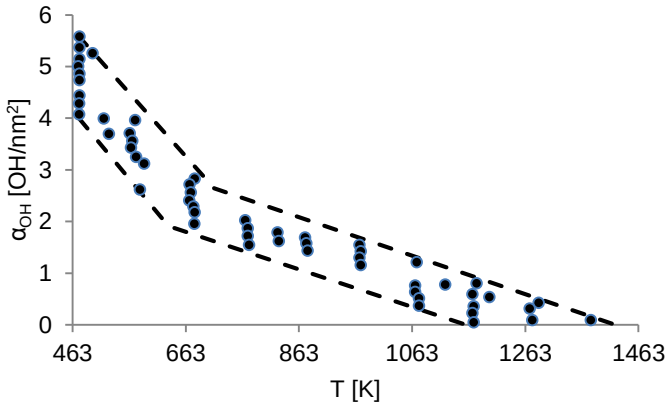

Both the wide range of temperatures required for complete dehydroxylation and the flattening in slope at 673 K indicate that silanol number strongly determines the surface chemistry properties. Otherwise, the dehydroxylation process would occur in a narrow temperature range at constant dehydroxylation rate.

The temperature dependence of silanol number has been simulated by condensation reactions between nearest silanol groups modeled on surface models based on a combination of several facets of β-cristobalite.[70] However, these type of models do not reproduce the actual structure of amorphous silica surfaces, and the condensation reactions between nearest neighbors are not always the more prone to occur.[40]

A recently proposed methodology where condensation reactions were simulated using a thermodynamic-base statistical approach is able to overcome the above mentioned issues.[40] This methodology simulates the dehydroxylation process by following the most energetically favorable path along a multistep procedure where the dehydroxylation energy is calculated for all silanol pairs with Si-Si and O-O distances less than 5.5 Å and 4.5 Å, respectively. At each step the pair of silanol groups giving the lowest dehydroxylation energy is removed and the resulting surface is used for a further calculation of dehydroxylation energy, then the

procedure is repeated until absence of silanol pairs available for further condensation reactions.

The dehydroxylation energy (ΔE_{DFT}) is calculated using the equation No. 1, where E_0 and E_f terms are the total DFT energies before and after the silanol pair condensation, respectively, and the E_{H_2O} term is the total DFT energy of an isolated water molecule. Complete details and assumptions regarding geometric constrictions for selecting each silanol pair prone to dehydroxylation are given in references.[40]

$$\Delta E_{DFT} = E_f - E_{H_2O} - E_0 \qquad \text{Eq. No. 1}$$

The approximated temperature for each surface is calculated by a Gibbs free energy balance as is stated in equation No. 2, where T corresponds to temperature, k is the Boltzmann constant, P_{H_2O} is the partial pressure of water, q_r is the rotational partition function of water, and Λ is the thermal de Broglie wavelength of water in the ideal gas state. Detailed derivation is found in references.[40]

$$\Delta G = \Delta E_{DFT} - kT \ln \frac{kTq_r}{P_{H_2O}\Lambda^3} \qquad \text{Eq. No. 2}$$

1.2.3 Modeling of noble metals supported on amorphous surfaces

There is considerable literature regarding the atomistic modeling of small metal clusters supported on crystalline surfaces.[71] However, references on modeling of metal clusters adsorbed on amorphous supports are scarce. Only the recent development of representative PBC models of amorphous surfaces have opened the way for theoretical study of adsorption of metal clusters, oxidized species, and organic molecules.[38, 72-73]

The DFT method has been used for studying the adsorption of chromium oxide on hydroxylated amorphous silica surfaces.[72] The chromium oxide - silica system (Cr/SiO_2) is an useful catalyst for polymerization of ethylene at low pressure. A

PBC model is used for modeling the surface,[37] whereas the chromium precursor (chromium coverage of 0.44 atoms/nm^2) is modeled by a H_2CrO_4 unit grafted to the surface by dehydration of silanols groups. The following reaction summarizes the adsorption of chromium oxide: $H_2CrO_4 + SiO_2(H_2O)_n(surface) \rightarrow O_xCr(OH)_y + SiO_2(H_2O)_{n-2x-y}(surface) + (2x+y)H_2O$, where n corresponds to the initial number of silanol groups, x the number of Cr=O bonds, and y the number of Cr-OH groups. The Cr species were systematically located on the surface in order to yield different modes of grafting (mono, n=1; di, n=2; tri, n=3; tetra, n=4). It was found that mono- and di-oxo monografted structures are the most stable. Moreover, it was concluded that nature of silanol groups (germinal, terminal) did not influence the geometry of grafted precursors.

A significant step forward in modeling of metal nanoparticles supported on amorphous surfaces was recently published.[38] Small metal nanoparticles were adsorbed on amorphous silica by following a multistep methodology addressing the diversity of features and roughnesses encountered on amorphous materials. A PBC model for the silica surface representative in terms of silanol number and the silanol distribution was used for the amorphous silica surface, whereas a small Pt cluster of 13 atoms with 7 Å as approximated diameter was used for the nanoparticle. The use of small Pt clusters is justified for studying the effect of surface features on metal-support interaction and cluster morphology while keeping a good computational compromise. The nature of nanoparticle-support binding interaction and its effect on nanoparticle structure and stability was elucidated. The changes in electronic structure due to nanoparticle reconstruction and metal-support interaction were also calculated. It was found that surface pretreatment temperature can be used for tuning the stability of silica-supported nanoparticles because the number of covalent cluster-surface bonds is function of pretreatment temperature.

2. COMPUTATIONAL METHODS

Here we briefly outline the mathematical framework of molecular dynamics (MD) and density functional theory (DFT) methods. The successful atomic modeling of materials relies on solving the Schrodinger equation in its time independent form.[46, 68] Unlike the classical equations of motion, the Schrodinger equation is able to describe the wave-like behavior that some particles describe at atomic scales. In its most general form the Schrödinger equation is expressed as follows:

$$\hat{H}\Psi(\vec{R},\vec{r}) = E\Psi(\vec{R},\vec{r}) \qquad \text{Eq. No. 3}$$

Where $\hat{H}$ is the Hamiltonian operator, $\Psi(\vec{R},\vec{r})$ is the wave-function, $\vec{R}$ and $\vec{r}$ are the space-spin coordinates of nuclei and electrons, respectively, and E is the total energy for the state described by the wave-function. The wave-function contains all information that can be known about the system. However, the wave-function has a complex nature and hence is not an observable, its physical interpretation can only be associated with the square of the wave function:[74]

$$\left|\Psi(\vec{R},\vec{r})\right|^2 d\vec{R}d\vec{r} \qquad \text{Eq. No. 4}$$

The functional dependence of the wave-function makes almost impossible the analytical solution of this equation in case of systems of practical interest. The interaction between many nuclei and electrons arises as a many-body problem, and the use of the Born-Oppenheimer approximation becomes an essential part of any scheme of solution.[46] The Born-Oppenheimer approximation relies on the difference in masses between electrons and nuclei. Only the electrons display a measurable wave-like behavior, and the heavier nuclei can be treated as classical particles having only a particle-like behavior. Based on this, the dynamics of electrons and nuclei can be separated and the wave-function is rewritten as a product of two functions:

$$\Psi(\overrightarrow{R},\vec{r}) = \chi(\vec{R}) * \varphi(\vec{r};\vec{R}) \quad \text{Eq. No. 5}$$

Where $\chi(\vec{R})$ corresponds to the wave-function of nuclei, and $\varphi(\vec{r};\vec{R})$ to the wave-function for the electrons which depends parametrically of nuclei positions. Now the particle-like behavior of nuclei is described using classical equations of motions, and only the wave-like behavior of electrons requires of solving the Schrodinger equation. Whereas the MD method is suitable for the first case,[75] the second case requires the use of quantum methods like the DFT method.[46] Details of each method are outlined in the following two sections.

2.1 Classical Molecular dynamics

The description of nuclei motion is addressed with the MD method. This enables the estimation of atomic structures and prediction of system observables through microscopic simulations.[75] The connection between the experimental measurements and the motion of nuclei is made via statistical mechanics.[76] Whereas MD calculates time averages, the averages in statistical mechanics correspond to experimental observables defined in terms of ensemble averages. Hence, the assumption of equality between time averages and ensemble averages makes possible the use of molecular dynamics for calculating macroscopic properties. Called Ergodic hypothesis,[77] this hypothesis is fundamental in statistical mechanics and is established as follows, where A corresponds to any given observable:

$$\begin{array}{ccc} \langle A\rangle_{emsemble} & = & \langle A\rangle_{time} \\ Ensemble\ average & = & Time\ average \end{array}$$

Because the assumption of particle-like behavior, the nuclei motions are followed by integration the classical equations of Newton:[75]

$$-\nabla_i V = m_i \frac{d^2 R_i}{dt^2} \qquad \text{Eq. No. 6}$$

Where m_i corresponds to the mass of the i-th nucleus, and V represent the potential of interatomic interaction. The potential of interatomic interaction plus the kinetic energy (K) give the total energy of system ($E = V + K$), whereas the initial

atomic positions are obtained from experimental data or calculations with a higher level of theory (e.g quantum methods). In most of cases the initial velocities are defined at thermal equilibrium according to the Maxwell-Boltzmann distribution.[78] The link between velocities and temperature is an example of using the Ergodic hypothesis. From statistical mechanics, the ensemble average of kinetic energy is defined as function of temperature (T) and the number of particles(N):

$$\langle K \rangle_{ensemble} = \frac{3}{2} k_b N T \qquad \text{Eq. No. 7}$$

Where k_b represents the Boltzmann constant. From molecular dynamics, the time average of kinetic energy is defined as follows:

$$\langle K \rangle_{time} = \frac{1}{2t_{max}} \int_0^{t_{max}} \sum_{i=1}^{N} m_i v_i v_i = \frac{1}{2} \langle \sum_{i=1}^{N} m_i v_i v_i \rangle \qquad \text{Eq. No. 8}$$

Hence, from the equality between ensemble averages and time averages we obtain an expression for temperature as a function of particle velocities:

$$T = \frac{1}{3k_b N} \langle \sum_{i=1}^{N} m_i v_i v_i \rangle \qquad \text{Eq. No. 9}$$

Other thermodynamic properties are obtained following the same procedure. The system pressure is defined as a function of kinetic energy and volume (V) as follows:

$$P = \frac{2}{3V} \langle K \rangle \qquad \text{Eq. No. 10}$$

Several cases are presented depending on what are the constraints applied on the system.[75] The microcanonical case (NVE) is presented if the number of particles, the volume, and total energy are held constant. In case of systems with constant number of particles and a constant volume, the control of temperature can be achieved by applying thermostat algorithms to the equation No. 9, giving place to the canonical ensemble (NVT). In the same way, an ensemble NPT is defined if volume changes are permitted and the pressure is controlled by using barostat algorithms in equation No. 10. The Nosé thermostat and its Hoover correction and

the generalized Langevin equation are examples of thermostats used in molecular dynamics simulations. The Nosé thermostat represents system's equilibrium energy in canonical ensembles, whereas the Langevin equation is used for non-equilibrium systems. Detailed derivation of these thermostats is found in references.[75, 79]

The **¡Error! No se encuentra el origen de la referencia.** shows the algorithm for numerical calculation of nuclei motions as a function of time.[80] For each stage it is required the calculation of forces on each nucleus. Calculation of a sufficient total time must be ensured for proper estimation of physical properties of interest. In general, this total time spans between 1 and 15 ns. Several algorithms are used for the integration of equations of motion which are expressed in function of Taylor expansions.[75] The simplest case is called Verlet algorithm. As is stated in equation No. 11, the Verlet algorithm uses the positions and accelerations at time t and the positions from time t-dt to calculate the positions at time t+dt. No explicit velocities are used. The advantages of Verlet algorithm relies in its simplicity and modest storage requirements. However, the precision of calculation is also low.

$$r(t+dt) = 2r(t) - r(r-dt) + a(t)dt^2 \quad \text{Eq. No. 11}$$

Other integration algorithms have been proposed in order to improve precision while enabling the use of larger time steps. Use of large time steps is essential to reduce computational cost and increase the total simulated time. Examples of these are the leap-frog algorithm, the velocity Verlet algorithm, the Beeman's algorithm and the predictor-corrector algorithms. Details about assumptions and derivation of each algorithm can be found elsewhere.

The formulation of an interatomic potential V is essential for a reliable molecular dynamics simulation.[75, 81] Besides the inclusion of all elements of periodic table, the interaction between nuclei must be described through inclusion of the electronic behavior between nuclei, the chemical and hybridization states, and bond types. In general this is grouped as follows: the valence of bond terms covers

the chemical bond stretching, the angles between three atoms, and the dihedral torsion angles. The energy distortions caused by the presence of nearby atoms are collected in the Cross terms, and the nonbonding terms includes the Van der Walls, the Coulomb and the Hydrogen bond interactions.

Figure 3: Algorithm for numerical calculation of nuclei motions as a function of time while positions and velocities.

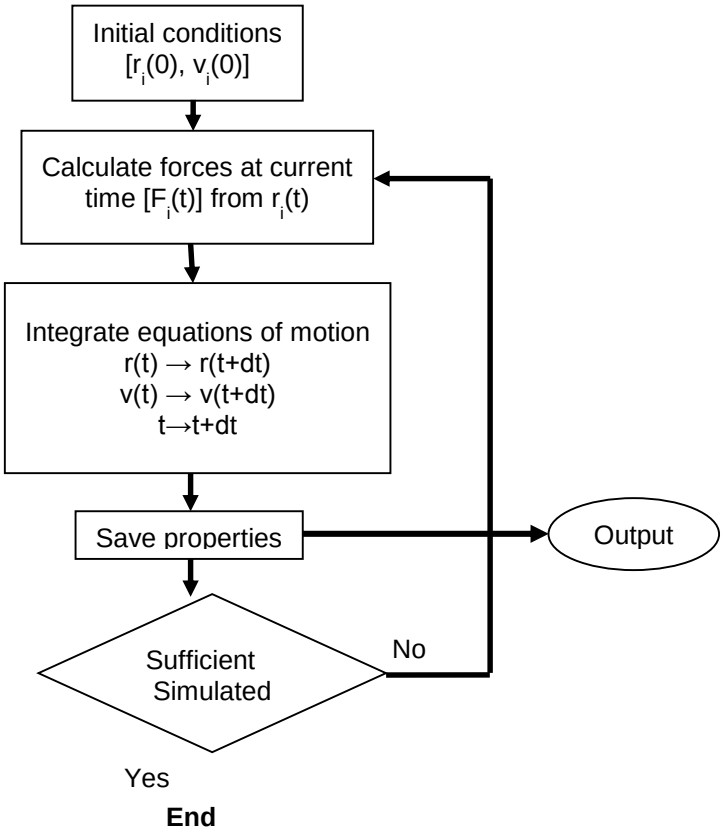

Inclusion of the about mentioned physics on a unique interatomic potential is a complex task and is currently an active research field. However, several approximations covering specific features have been developed depending of the properties of interest in a molecular dynamics simulation. The Sutton-Chen many-body potential is an example for an accurate description of transition metals. The reactive bond order potential (REBO)[82] and the Reax Force Field (ReaxFF)[83] are

especially suitable for reactive systems where bond formation and breaking events are present.

The universal force field (UFF) has been developed for modeling of materials where angular distortions near the linearity are present, as is the case of amorphous silica.[84] Based only on the nuclei specie, its hybridization, and connectivity, the UFF potential facilitates the study of a variety of atomic associations where bond formation and breaking events are not considered. Examples of these are optimization of zeolites structures which have equilibrium angles of approx. 150º and distort thermally to 180º with barriers to inversion of approx. 1 kcal/mol. The UFF potential has been successfully applied in structural relaxations in several types of atomic systems.[61, 84]

2.2 Density Functional Theory (DFT)

Now we turn to the electron dynamics which require solving the Schrodinger equation as is established in equation No. 12. For a given set of nuclei positions, solving of Schrodinger equation is finding a complete set of electronic wave-functions $\varphi(\vec{r};\vec{R})$ able to give the ground-state energy E_{elec} when the Hamiltonian operator $\widehat{H}_{elec}$ is applied on them.

Here we first discuss the framework required to perform an energy calculation for fixed nuclei, and then we discuss the methods for optimization of nuclei positions and cell dimensions.

$$\widehat{H}_{elec}\varphi(\vec{r};\vec{R}) = E_{elec}\varphi(\vec{r};\vec{R}) \qquad \text{Eq. No. 12}$$

The full expression in atomic units for the electronic Hamiltonian is written in equation No. 13. The first term defines the kinetic energy of electrons. The second is potential interaction energy between nuclei and electrons, whereas the third one corresponds to the electron-electron interactions. The existence of the electron-electron interaction term indicates the many-body problem that implies finding a solution for the equation No. 12. Any iterative scheme of solution based on

approximate expressions for the wave-function faces the many-body problem, so their use in most of practical related problems becomes almost unreachable in terms of computational costs.

$$\hat{H}_{elec} = -\frac{1}{2}\sum_{i=1}^{N}\nabla_i^2 - \sum_{i=1}^{N}\sum_{A=1}^{M}\frac{Z_A}{r_{iA}} + \sum_{i=1}^{N}\sum_{j>i}^{N}\frac{1}{r_{ij}} = \hat{T} + \hat{V}_{Ne} + \hat{V}_{ee} \qquad \text{Eq. No. 13}$$

A practical way for reduce the many-body problem to a 3-variable problem is realizing that a physical interpretation of the wave-function can be done through the definition of the electron density.[46] The electron density determines the probability of finding any electron of the system within a volume element:

$$\rho(\vec{r}) = \int \left|\varphi\left(\vec{r};\vec{R}\right)\right|^2 d\vec{r} \qquad \text{Eq. No. 14}$$

The idea behind DFT relies in finding an electron density minimizing the system energy. This idea is formally established by the two theorems of Hohenberg and Khon.[46] The first theorem states that the ground state energy of Schrodinger equation is a unique functional of the electron density, whereas the second indicates that Schrodinger equation is fully solved if and only if the electron density that minimizes the energy of the functional is the ground-state electron energy. The energy functional is expressed as follows:

$$E[\rho(\vec{r})] = \int \rho(\vec{r})\hat{V}_{Ne}(\vec{r})d\vec{r} + T[\rho(\vec{r})] + E_{ee}[\rho(\vec{r})] \qquad \text{Eq. No. 15}$$

Where the first term corresponds to the functional of potential energy between electrons and nuclei; the second term represents the functional of kinetic energy of electrons; the third term collects the Coulombic electron-electron interactions; the last term contains the non-classical portion due to the self-interaction correction. Because the last two terms are independent of nuclei positions, they are collected in a unique term called universal functional. All quantum effects are included in the universal functional; however its exact form is unknown so far.

The equation No. 16 shows the energy functional with an approximation proposed by Khon and Sham for the universal functional as the sum of three terms. The term $T_s[\rho(\vec{r})]$ describes the kinetic energy for a system of non-interacting electrons; $J[\rho(\vec{r})]$ corresponds to the electron-electron Coulombic energy for that system, and the exchange correlation term $E_{xc}[\rho(\vec{r})]$ contains all the unknown quantum contributions and the self-interaction corrections in the electron-electron Coulombic energy. The use of a non-interacting system relies on the inability of formulate exact expressions for the functional of kinetic energy of electrons and potential energy of electron-electron interactions. In that way, the residual part of the real system that is not covered by the non-interacting system is added to the exchange correlation term.

$$E[\rho(\vec{r})] = \int \rho(\vec{r})\hat{V}_{Ne}(\vec{r})d\vec{r} + T_s[\rho(\vec{r})] + J[\rho(\vec{r})] + E_{xc}[\rho(\vec{r})] \qquad \text{Eq. No. 16}$$

The practical use of the Kohn Sham approach is possible through definition of a set of single-electron functions $\psi_i(\vec{r})$ and use of variational principle for the reformulation of equation No. 16 as a function of these single-electron functions. The electron density now is expressed as a product of single electron functions:

$$\rho(\vec{r}) = \sum_{i=1}^{N} |\psi_i(\vec{r})|^2 \quad \text{Eq. No. 17}$$

The reformulated Kohn-Sham equations for a single-electron function now have the form:

$$\left(-\frac{1}{2}\nabla^2 + \left[\int \frac{\rho(\vec{r}\prime)}{|\vec{r}-\vec{r}\prime|} d\vec{r}' + V_{Ne}(\vec{r}) + V_{xc}(\vec{r})\right]\right)\psi_i(\vec{r}) = \varepsilon_i\psi_i(\vec{r}) \qquad \text{Eq. No. 18}$$

Where the first term represents the kinetic energy, and the three terms within brackets defines the effective potential which describes the interaction between particles and the quantum mechanical effects. The first term within the brackets defines the Coulombic interaction between electrons, whereas the second regulates the interaction between electrons and nuclei. The third potential within brackets is the exchange correlation term. Because the explicit form of this term is

unknown, it is simply defined as the functional derivative of $E_{xc}[\rho(\vec{r})]$ with respect to $\rho(\vec{r})$:

$$V_{xc}(\vec{r}) = \frac{dE_{xc}[\rho(\vec{r})]}{d\rho(\vec{r})} \quad \text{Eq. No. 19}$$

The dependence of the effective potential on the electron density suggests that Kohn-Sham equations must be iteratively solved. Thus, assuming an approximation for the exchange correlation term, an initial electron density must be guessed and then updated according to the iterative procedure outlined in **¡Error! No se encuentra el origen de la referencia.**. The effective potential is calculated for each electron density, and then the Kohn-Sham equations are evaluated in order to get the single-electron functions required for update the electron density. The new and old electron densities are compared to check if the criterion convergence is fulfilled. When this happens, the ground-state electron density for the nuclei positions is found and the other observables now can be calculated.

2.2.1 Approximations for the exchange correlation functional

Several approximations for the exchange-correlation functional have been proposed.[46] The absence of an analytical expression for the exchange-correlation functional hinders a straightforward comparison between approximations, so the reliability of an approximation mostly relies on the degree of approximation of data obtained from experimental or methods of higher level of theory. The local density approximation (LDA) is the first and simplest approximation. This approach considers that nuclei exert a constant potential on the electrons, maintaining also constant the electron density along the space. Although the irregularity of electron density at chemical bonds makes the LDA approximation unrealistic, the assumption of a uniform electron gas facilitates an adequate expression for the exchange-correlation functional at specific atomic positions. The generalized gradient approximation (GGA) includes a dependence of the exchange correlation functional on the local gradient of the electron density. A family of functional has

been derived based on different descriptions for the electron density gradient. The Perdew-Burke-Erzenhorf (GGA-PBE) functional is the most common of this family. Other functional is the RPBE, which compared to the PBE gives superior chemisorption energies for bonding of atoms and molecules to surfaces but worse results for bulk properties.

Figure 4: Iterative procedure for applying the DFT method.

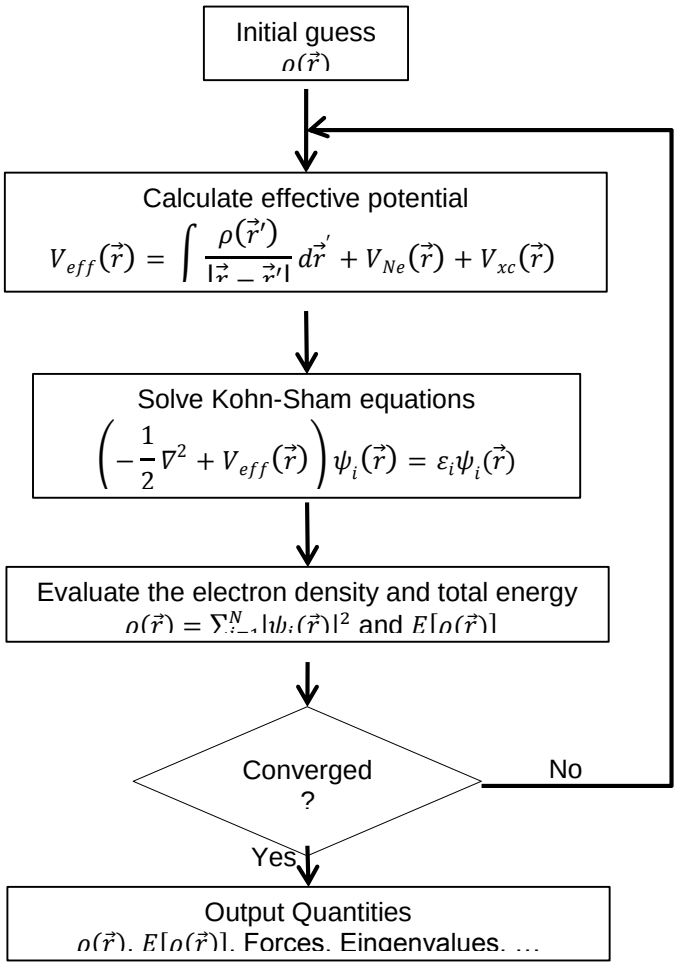

2.2.2 Periodic boundary conditions

Use of atomic models with periodic boundary conditions is common in surface science modeling.[32] The DFT calculations with periodic boundary conditions are performed using a set of solutions satisfying the Bloch theorem. The Bloch theorem states that total solution is expressed as a sum of plane-wave functions

defined in the reciprocal space. The advantage of working in reciprocal space relies on the reduction of numerical integration of the effective potential of the Brillouin zone. This numerical integration requires the space discretization into a set of k points. A frequently used method for space discretization is the Monkhorst-Pack procedure, which balances accuracy and computational cost for each direction of the reciprocal space. This balance reduces the total number of *k* points within the Brillouin zone, which helps in the minimization of numerical effort.

The single-electron wave functions are now represented by an infinite sum of plane-wave functions and a function with system's periodicity also expanded in terms of plane-waves:

$$\psi_i(\vec{r}) = \sum_{\vec{G}} c_{i,\vec{k}+\vec{G}} \exp\left(j\left(\vec{k}+\vec{G}\right).\vec{r}\right) \quad \text{Eq. No. 20}$$

Here the reciprocal and direct vectors are represented by $\vec{k}$ and $\vec{r}$. $\vec{G}$ is defined as the sum of all vectors in reciprocal space. The $j\vec{k}$ component corresponds to the plane-wave function, whereas the $j\vec{G}$ to the periodic function in space. The numerical evaluation of equation No. 20 requires a truncation. As the energy of plane-waves increases they become less important for the system making possible its elimination above an energy cutoff. The relation between the energy cutoff and the set of reciprocal space vectors is defined as follows:

$$E_{cutoff} = \frac{\hbar^2}{2m} G_{cutoff}^2 \quad \text{Eq. No. 21}$$

Now the equation No. 20 is expressed as:

$$\psi_i(\vec{r}) = \sum_{\vec{G}}^{Ecutoff} c_{i,\vec{k}+\vec{G}} \exp\left(j\left(\vec{k}+\vec{G}\right).\vec{r}\right) \quad \text{Eq. No. 22}$$

2.2.3 Optimization of atomic positions

Finding the atomic positions and/or cell parameters of the ground-state energy is essential for the calculation of crystal structures, adsorption energies, reaction

energy barriers, etc.[68] The DFT method generally uses an iterative geometry optimization using two relaxation cycles. In the inner self-consistent cycle the electronic ground-state is calculated for a fixed configuration, whereas in the outer cycle (ionic update) the forces acting on each ion are calculated based on that electronic ground-state and the ionic positions are update.

Several methods are available for update the ionic positions, some examples are the quasi-Newton and the conjugate-gradient methods. The quasi-Newton method uses the forces and the stress tensor to calculate the new ionic positions without using the system total energy, whereas the conjugate-gradient method follows predictor-corrector algorithm. For the conjugate-gradient method, a first trial is guessed in the direction of energy gradient, and the energy and forces are reevaluated. By using cubic interpolation the minimum energy is hence calculated taking into account alterations to the energy and forces. The corrector step follows for update the minimum energy, followed by a recalculation of the energy and forces.[85]

2.2.4 Pseudopotentials – PAW method

The use of pseudopotentials eliminates the necessity of an explicit treatment of strongly bounded and chemically inert core-electrons, and is a prerequisite for a successful use of the plane wave basis-sets approach.[32] The theory of pseudopotentials is mature and has led to the development pseudopotential methods such as “non-conserving” pseudopotentials,[86] ultra-soft pseudopotentials (US-PP),[87] and the Projector Augmented Wave (PAW) method.[88]

Of especial interest is the PAW method which is able to reconstructs the full all-electron density and avoids the necessity of nonlinear core-corrections, as other pseudopotential methods need to do.[32] The relaxed-core version of VASP-PAW puts pseudopotential-based PW calculations at the same level of accuracy as the most accurate all-electron calculations such as the full-potential linearized

augmented plane-wave (FLAPW) method, which is computationally much less efficient.[89]

2.3 The Vienna Ab-initio Simulation Package

The Vienna Ab-initio simulation package (VASP) developed by Georg Kresse and co-workers is a successful initiative for using DFT in solid-state and materials science.[85] The VASP code is intended for modeling periodic systems using plane waves (PW) basis-set and pseudopotentials (PP).[32] The PW offers control of basis-set convergence and the ability of use the Hellmann-Feynman theorem to calculate the forces acting on the atoms and of the stresses on the unit cell, whereas the use of PP eliminates the need for an explicit treatment of the strongly bound and chemically inert core-electrons.

The VASP code uses two relaxation cycles. In the inner self-consistency cycle the electronic ground state for a fixed atomic configuration is calculated. In the outer one, a conjugate gradient optimization of the atomic structure is performed.[30] The VASP code solves the Kohn-Sham equations based on a band-by-band optimization of the eigenstates via minimization of the norm of the residual vector to each eigenstate. This has the advantage that it is free of orthogonality constrains. After updating all required eigenstates, re-orthogonalization by sub-space diagonalization is sufficient and easy to perform. The reduction of the number of orthogonalizations greatly improves the scaling of the computational effort with systems size, scaling remains $O(N^x)$ with $x < 2$ up to very large system size.

All levels of theory have been implemented in VASP for the exchange-correlation functional.[32] The LDA approximation, several gradient-corrected functionals (BP, PW91, PBE) and hybrid functionals are some examples of them.

The k-points in the irreducible part of the Brillouin zone are calculated using the Monkhorst-Pack method.[90] Several methods can also be used for handling the convergence with respect to the k-points sampling:[85] the linear tetrahedron

method, the smearing methods such as finite temperature approaches or improved functional form (Methfessel and Paxton method, and finite methods such as Gaussian or Fermi smearing). Detailed references about the development of VASP code can be found in elsewhere.[85]

2.3.1 Vibrational calculations using VASP

The VASP code uses the harmonic approximation for calculation of vibrational frequencies and the corresponding normal modes.[85] The finite differences method is used to calculate the Hessian matrix (matrix of the second derivatives of energy with respect to the atomic positions) and the vibrational frequencies of a system. Within this method, each atom is displaced from their equilibrium position on each Cartesian coordinated and the forces are calculated via the Hellmann-Feynman theorem. Hence, the Hessian matrix is determined from the forces. Frequency calculations are considered using only one k-point in each coordinate.[30, 85]

2.4 Theoretical descriptors of intrinsic Brönsted acidity

There is general agreement that catalytic activity of solid acid catalysts is related to the acidity strength of its Brönsted acid sites,[4, 25, 91] however, the quantification of this relation through theoretical descriptors is not trivial. At the best of our knowledge, three different approaches have been used: the deprotonation energy (DPE) calculations, the adsorption of basic molecules, and the OH-stretching frequency calculations.

The DPE calculations provide a measure of intrinsic acid strength.[92-94] However, the calculation of this quantity on PBC models faces two issues: First, the negative charge of the deprotonated acid site creates a diverging term in the potential energy; second, unphysical charge interactions could appear between neighboring deprotonated sites. Use of periodic boundary conditions implies that the deprotonation of a hydroxyl group means the existence of a copy of this deprotonated site in each of the neighboring cells.[68]

Adsorption of basic molecules such as ammonia, pyridine, and CO, has been reported as a straightforward method for theoretical calculation of surface acidity.[94-96] However, there is no general agreement about the validity of this calculation as a measure of intrinsic acidity strength as it contains contributions from the interaction between the adsorbted and the deprotonated acid site.[97]

The other theoretical descriptor for intrinsic acidity is the quantification of the OH-stretching frequency.[30, 37, 98-99] For this method the comparison between calculated OH-stretching frequencies and experimental data is direct and straightforward. Lower OH-stretching frequencies are associated with stronger Brönsted acidity.[30, 36-37] Moreover, the implementation of the finite-difference method for calculation of the OH-stretching frequencies is particularly suitable with PBC models; the forces acting on single atoms that are displaced from their equilibrium positions at a conserved framework structure are calculated via the Hellmann–Feynman theorem and the numerical derivatives of these forces are used to construct the partial dynamic matrix.

2.5 Bader charge analysis

The calculation of charge transfer between atoms is useful for describing the properties of a surface or material. For doing this, many different schemes have been proposed, some of them based on electronic orbitals and others solely based on the charge density.[100]

The Bader charge method is one of those methods based on the charge density.[101] This method performs the decomposition of the electronic charge density by dividing the space into regions limited by surfaces that run through minima in the charge density (Bader regions). Because this analysis is based solely on the charge density, it is rather insensitive to the basis set used in the electron wave-function calculation and can be used to analyze the plane wave based calculation as well as calculations using atomic basic functions. Each Bader region often contains one nucleus (although there are exceptions). The total charge on an atom

can be estimated by integration of the electronic density within the Bader region where a nucleous is located, and possibly adding the electronic charge in nearby regions that do not include a nucleus. The complete details about the algorithm for Bader decomposition of charge density is found in references.[50]

Examples of the use of Bader charge analysis are the calculations of geometric stability, electronic structure, and intercalation mechanism of Co adatom anchors on graphene sheets,[56] the characterization of Hexagonal Phosphorus Adlayers on Platinum (111),[102] the adsorption of metal adatoms on single-layer phosphoren,[103] and so on.[57]

2.6 The Radial Distribution function

The structure of amorphous materials is often characterized using the radial distribution function (RDF).[68] The radial distribution describes how, on average, the atoms in a system are radially packed around each other:

$$g(r) = \frac{\rho(r)}{4\pi r^2 \bar{\rho}} \qquad \text{Eq. No. 23}$$

Where $g(r)$ is the average density of atoms found in a thin shell at a radius r from an arbitrary atom in the material, and $\bar{\rho}$ is the average density of the entire material. The RDF function gives a number of important features: when r tends to zero then $g(r)$ tends to zero because the atoms cannot overlap each other. For large values of r the $g(r)$ tends to one because in a disordered material the atoms separated by large distances not influence each other. At intermediate distances a number of peaks appear, indicating that atoms are packed around each in 'shells' of neighbors. The occurrence of peaks at long range indicates a high degree of ordering. In general, at high temperature the peaks are broad, indicating thermal motion, while at low temperature they are sharp. The peaks are particularly sharp in crystalline materials, where atoms are strongly confined in their positions.[104]

3. RESEARCH DESIGN AND METHODOLOGY

It is established that structural features of the SBA-15 place this material as a feasible alternative for designing high performance HPC catalysts;[4] however, the lack of Brönsted acid sites on SBA-15's surface hinders the successful implementation of the SBA-15-based HPC catalysts.

This work is motivated for the need of novel HPC catalysts for producing fuels within the environmental regulations.[105] The current design strategies of novel HPC catalysts include variations in preparation methods, changes in active phase formulation, and support modification.[19] Here theoretical modeling using DFT is adopted as an alternative for achieving an atomic level explanation of Brönsted acid properties and an explanation of the enhanced catalytic activity observed in catalysts supported on SBA-15 modified through isomorphic substitution of Si^{4+} atoms by Al^{3+} and Ti^{4+}.[4, 17, 21, 23]

This research is outlined as follows: section 4.1 addresses the formulation of an adequate model for inner pore surface of the SBA-15; section 4.2 explains how the temperature dependence of silanol number has been taken into account; section 4.3 introduces the use of a theoretical descriptor for theoretical quantification of surface Brönsted acidity in pure and modified SBA-15; section 4.4 summarizes how to perform the isomorphic substitutions of Si^{4+} atoms by Al^{3+} and Ti^{4+}; and section 4.5 presents the methodology followed in order to elucidate an explanation for the catalytic activity observed in SBA-15-supported noble metals.

3.1 Modeling the inner surface pore of the SBA-15

A flat slab model with periodic boundary conditions (PBC model) is considered for modeling the inner pore surface of the SBA-15. Modeling of the entire mesoporous channel is computationally expensive and is disregarded based on the assumption of absence of diffusional limitations and confinement effects.[27, 32] Use of a PBC model facilitates the control of basis set convergence and eliminates the need of artificial saturation of dangling bonds.[36] Moreover, it facilitates an adequate

representation of density and type of surface hydroxyl groups,[37-39] which is crucial for a representative study of Brönsted acidity properties[36]

The amorphous structure of the SBA-15 frameworks is included in the PBC model.[21, 48-49, 67]. Although the translational symmetry of the PBC model,[69] the accurate reproduction of this amorphous structure is ensured by using a unit cell with larger dimensions than the interatomic distances (Si-O bond length = 1.63 Å).

4. Temperature dependence of silanol number

The temperature dependence of silanol number is taken into account because this strongly influences the distribution and reactivity of surface silanol groups.[41] The statistical-thermodynamic approach already outlined in section 2.2.3 is used for modeling the temperature dependence of silanol number. By doing this, several slab models are generated, each of them representative for a different temperature range.

4.1 Theoretical descriptor for surface Brönsted acidity

OH-stretching frequency calculations are used for quantifying the acidity strength of surface silanol groups and bridging hydroxyl groups. This method is particularly suitable for quantifying the effect of structural distortions on Brönsted acidity of hydroxyl groups after isomorphic substitutions in the SBA-15 framework.

4.2 Surface modification: Isomorphic substitutions of Si^{4+} atoms by Al^{3+} and Ti^{4+}

The Loewenstein rule has been taken into account for the calculation of isomorphic substitutions, in such a manner that existence of -Al-O-Al- bridges is avoided. The Loewenstein rule states that whenever two tetrahedra are linked by one Oxygen bridge, the center of only one of them can be occupied by aluminum; the other center must be occupied by silicon, or another small ion of electrovalence four or more.[106-107] Several works support the validity of Lowenstein rule.[107]

The stability of Al^{3+} incorporation and subsequent protonation of an O atom bonded to the Al atom is quantified through evaluation of formation energy (*ΔE*) as follows:

$$\Delta E = E(Al_nSi_{27-n}O_{65}H_{22+n}) + E_{Si} - E(Al_{n-1}Si_{27-n+1}O_{65}H_{22}) - E_{Al} - E_H$$

Eq. No. 24

The index *n* specifies the number of Al atoms in the model, whereas $E(Al_nSi_{27-n}O_{65}H_{22+n})$ and $E(Al_{n-1}Si_{27-n+1}O_{65}H_{22})$ refer to the DFT energies for the relaxed structures with *n* and *n-1* Al substitutions, respectively. E_{Si}, E_{Al} and E_H are the energies of Si, Al and H atoms, respectively.

The formation energy for the Ti^{4+} incorporation is evaluated in a similar manner:

$$\Delta E = E(Ti_nSi_{27-n}O_{65}H_{22}) + E_{Si} - E(Ti_{n-1}Si_{27-n+1}O_{65}H_{22}) - E_{Ti} \quad \text{Eq. No. 25}$$

Again, the index *n* indicates the number of Ti atoms, $E(Ti_nSi_{27-n}O_{65}H_2)$ and $E(Ti_{n-1}Si_{27-n+1}O_{65}H_{22})$ refer to the DFT energies for the model with *n* and *n-1* isomorphic substitutions, respectively, and E_{Si} and E_{Ti} are the DFT energies of the Si and Ti atoms, respectively. A negative value for the formation energy indicates an energetically favorable substitution.[30]

4.2.1 Formation of bridging hydroxyl groups after Oxygen protonation

The **¡Error! No se encuentra el origen de la referencia.** outlines the formation of ridging hydroxyl groups after Al incorporation. The H^+ proton is placed in a coplanar fashion with respect to the Aluminum, Oxygen, and Silicon atoms. The H-O distance is set at 0.915 Å, and the Al-O-H angle is set to be equal to the Si-O-H angle. A DFT optimization is applied after each proton H^+ addition.

For the Al^{3+} incorporation all the Al-O-Si bridges are tested as possible sites for protonation; the surface's amorphous nature hinders the possibility of use symmetric properties to reduce calculations. Use of symmetry properties to reduce calculations is evidenced in other works addressing the study of structural and acidity properties of zeolites.[30]

Figure 5: Oxygen protonation after Al incorporation, structure before relaxation. Red balls: O; purple ball: Al; yellow balls: Si; white ball: H.

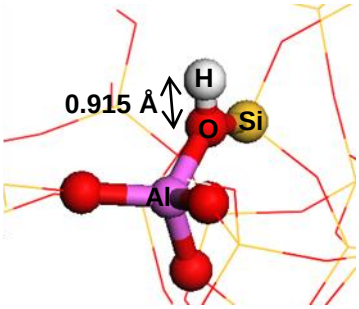

4.3 Noble metal cluster supported on the slab model surface

SBA-15-supported noble metals are envisioned as potentially new HDS catalysts.[26, 49] Here the adsorption of a Pt-cluster is addressed in order to evaluate the effect of surface modification at two different temperatures, before and after modification with Al atoms (four different surfaces). The Pt metal is selected as probe specie because of its catalytic activity and sulfur-tolerant properties for the HDS of Thiophene,[49] Dibenzothiophene,[62] and heavy oils.[108]

The generation of the initial structures for the adsorption of a Pt-cluster on an amorphous surface is not trivial because the diversity of surface features and atomic surface roughness; artificial restructuring can arise if the Pt-cluster is too close to the surface, whereas, if it is placed too far the relaxation will not occur because of the lack of long-range forces in DFT. In order to overcome this issue, here we adopted a methodology developed for studying the relaxation of catalytic nanoparticles on amorphous supports:[38]

- A Pt-cluster is selected as the metallic phase. The Pt-cluster size must be small enough in order to guarantee that metal-support interactions significantly affect the cluster morphology. The cluster initial geometry is not important. For small Pt-clusters it has been demonstrated that the energy of the final structure is independent of the initial unsupported cluster structure.[38]

- A 5-by-4 grid is generated over the support surface in such a way that 20 uniformly distributed adsorption sites are defined. A 5-by-4 grid is selected in such way that spacing between adsorption sites be smaller than the Pt-cluster size.
- The Pt-cluster is placed on each grid point in the xy plane above the silica surface.
- The Pt cluster is dropped onto the surface until the minimal distance between any of the Pt atoms and any of the O surface's atoms be equal to the Pt-O covalent distance (Pt-O bond distance approx. 1.98 Å)
- The formation of cluster-surface bonds is facilitated as follows:
    - It is assumed that Pt-Si bonds are not formed, and formation of Pt-O bonds is assumed as long as there is close contact between the Pt-cluster and a surface Oxygen atom (covalent distance). The formation of metal-Si bonds in silica materials is experimentally reported only at temperatures higher than calcination temperatures, whereas formation of Metal-Oxygen bonds is experimentally reported for noble metals supported on Silica.[109-111]
    - Pt-O bond formation is facilitated by remotion of hydrogen atoms from hydroxyl groups within the distance for a Pt-O bond. H_2 desorption is assumed for systems with even number of Pt-O bonds, whereas for systems with odd number of Pt-O bonds the remanent hydrogen atom is placed on top of Pt-cluster.
- Each of the 80 generated systems is optimized with DFT (20 systems per surface – 4 surfaces). All atoms are enabled to move in all calculations.

The correlation between the relaxed structures and possible catalytic activity is elucidated as follows:

- **Interaction energy (E_{int}):** The E_{int} between the metal cluster and the surface, as it is calculated with the equation below, is directly related with its adhesion energy and hence the cluster stability. The adhesion energy is

defined as the work required for separating the metal/support interface in vacuum per interfacial area. A stronger adhesion energy results in a lower chemical potential of the supported metal. The chemical potential is inversely related to the apparent activation energy of the sintering process, where the sintering process negatively affects the stability at high temperatures of supported metal nanoparticles.[112]

$$E_{int} = E_{Pt-Surf} - E_{Pt}^{fixed} - E_{Surf}^{fixed}$$ Eq. No 26

Where $E_{Pt-Surf}$ refers to the energy of the cluster-surface system, and E_{Pt}^{fixed} and E_{Surf}^{fixed} corresponds to the energy of the isolated cluster and surface after relaxation of the cluster-surface system, respectively.

- **Coordination number (CN):** The CN of supported metal nanoparticles has been strongly correlated with binding energy of molecules on the metal nanoparticle, which is related with catalytic activity.[113]
- **Pt-Pt bond distances:** The metal-metal bond length has been show to correlate with adsorbate binding strength and hence could significantly affect catalytic reaction rates.[114]
- **Electronic charge transfer between the cluster and the surface:** The magnitude of electronic charge exchange between supports and metal nanoparticles has an strong impact on catalytic reactions.[115]

5. COMPUTATIONAL SYSTEM AND DETAILS

A periodic flat film of hydroxylated amorphous silica is used for modeling the inner pore surface of the SBA-15.[37] The atomic coordinates were approximately extracted from an earlier work[92] by using a graphical method implemented in the G3DATA Graph Analyzer code.[116] The unit cell dimensions are 17.6 Å x 12.5 Å x 25.2 Å. The total number of atoms is 120 ($Si_{27}O_{67}H_{26}$), and the film's average density is 1.9 g/cm^3; the model density is in qualitative agreement with reported values for bulk silica (2.14 g/cm^3).[76-77] The film thickness is approximately 9 Å.

Both the MD and the DFT methods are used in tandem for structural relaxation calculations and dehydroxylation simulations. The MD calculations were performed using the Universal Force Field (UFF) potential as implemented in AVOGADRO code,[31] whereas the DFT calculations were performed using Vienna Ab-initio Simulation Code (VASP).[32-34]

For the DFT calculations, the generalized gradient approximation proposed by Perdew-Burke-Ernzerhof (GGA-PBE) is used for the exchange-correlation functional approximation;[35] the PBE functional is one of the most widely used in plane-wave DFT calculations, and its reliability for predicting structural and thermodynamic properties have been tested in several works.[117] The core-electron interactions are described using the Projector Augmented Wave (PAW) pseudopotential.[88, 118] Spin-polarized calculations are carried out. Because the large size of the unit cell, the surface Brillouin-zone integration is calculated using the gamma point Monkhorst-Pack mesh[90]. The ionic relaxation loop is performed until total energy differences were below to 10^{-3} eV and the electron self-consistent iteration was set to 10^{-4} eV. All atoms were enabled to move in both MD and DFT relaxations. For the DFT relaxations, a plane wave expansion up to 230 eV is used first. Afterwards, the plane-wave basis set is extended up to 400 eV for a final more exigent relaxation.

The surface acidity properties are studied by calculating the OH-stretching frequencies of the both the surface silanol groups and the Brönsted acid sites created due to Oxygen protonation after isomorphic substitution of Si atoms by Al atoms. The finite differences method within harmonic approximation as implemented in VASP is used for calculating the Hessian matrix. Only the O and H atoms are allowed to move for the OH-stretching calculations.

The Pt-cluster adsorption calculations are performed using DFT with a plane-wave basis set of 400 eV. The Pt-cluster is represented by a cluster having 13 atoms (Pt_{13}); the Pt_{13} has an icosahedral geometry with a central Pt atom and twelve surrounding Pt atoms arranged in such a manner that only 111 facets composed of three atoms are present.[119] The Pt_{13} cluster is the smallest stable cluster which follows the magic number rule for metallic Pt clusters.[120] Before adsorption calculations the unsupported Pt-13 cluster is subject to DFT relaxation using the same computational parameters used for the surface.

6. RESULTS AND DISCUSSION

6.1 Hydroxylated amorphous silica film: Structural parameters

The **¡Error! No se encuentra el origen de la referencia.** shows three different iews of the hydroxylated amorphous silica film. From the most to the less common, the obtained Si-membered ring size distribution is as follows: 6 > 7 > 4 > 5 > 8 > 9 > 10. The predominance of 6-membered rings is in agreement with other works.[37, 47] However, the ratio between 7- and 5-membered rings is inverted compared to the reference from which this model is based.[37] Regardless this discrepancy, which is attributed to the need of using a graphical method for extracting the atomic coordinates, this film can be still considered a valid representation of a hydroxylated amorphous silica surface, as is stated below.

Figure 6: PBC model of the hydroxylated amorphous silica film: a) Top view; b) Side view; c) Orthographic view.

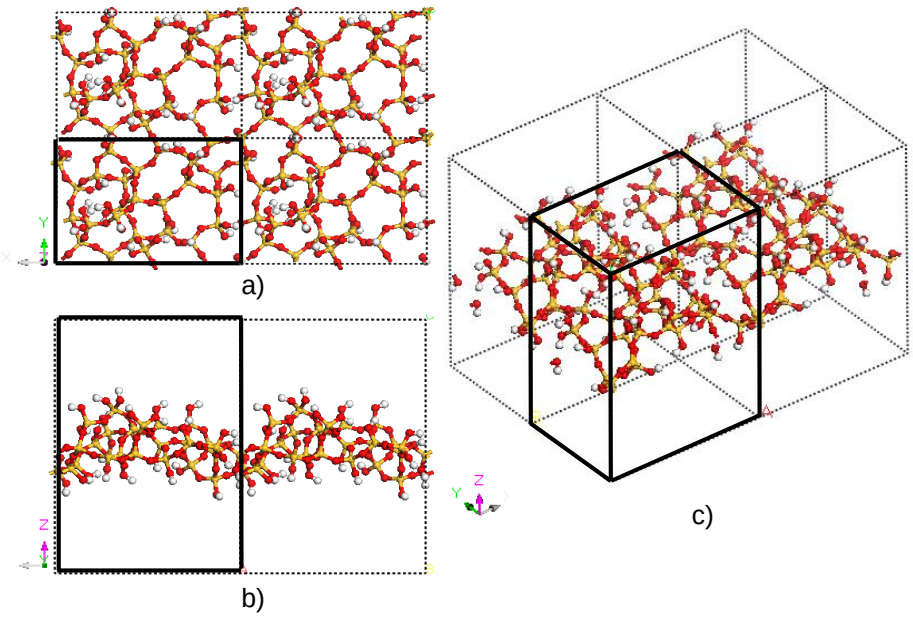

The Table 1 compares experimental data and average calculated values for the Si-O bond length and the Si-O-Si and O-Si-O angles,[121-123] whereas the **¡Error! No se encuentra el origen de la referencia.** shows the distribution for the Si-O-Si angle. The calculated average values are in good agreement with the experimental

and theoretical data. The standard deviation for the Si-O bond length and the O-Si-O angle indicate that SiO_4 tetrahedrons remain almost undistorted, whereas the Si-O-Si distribution spans from 125 to 165 degrees. These results are in agreement with earlier works on Si-based materials where is indicated that the amorphous nature of silica is due to the flexibility of the O-Si-O angle.[61, 124-125]

Table 1: Calculated structural parameters vs. experimental structural data for amorphous silica.

	This work (Average Value)	Standard Deviation (σ)	Experimental value
Si-O [Å]	1.639	0.01	1.61[121] 1.62[122]
O-Si-O angle [deg]	109.48	2.68	109.4[123] 109.5[122]
Si-O-Si angle [deg]	143.51	9.29	143[122] 153[122]

Figure 7: Computed Si-O-Si angle distribution.

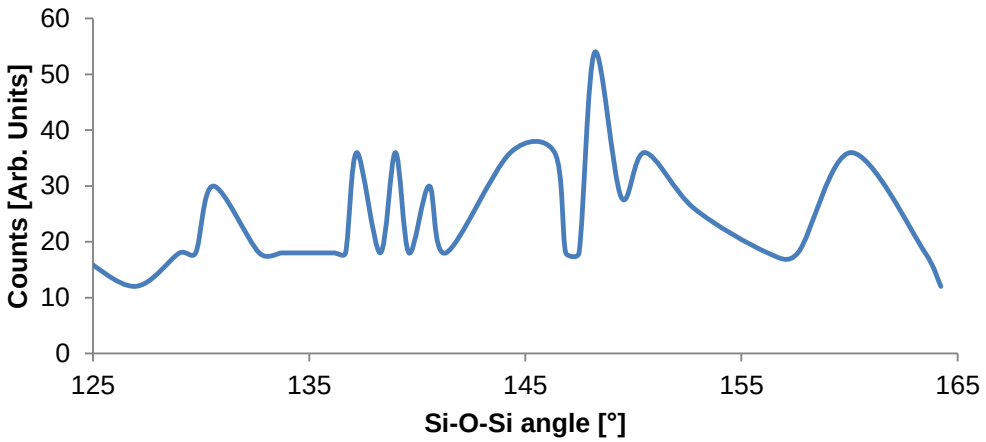

The **¡Error! No se encuentra el origen de la referencia.** shows the RDF function f our hydroxylated amorphous silica film compared with the RDF function of bulk crystalline α-SiO_2. The peak around 1.63 Å in both functions indicates the existence of short-range ordering, whereas the disagreement between both functions at Si-O distances above 3 Å evidences the absence of long-range ordering of our hydroxylated amorphous silica film. Moreover, at larger Si-O

distances the RDF of our hydroxylated silica film oscillates around the value of 1, being a characteristic feature of amorphous structures.[104] The narrow and small peak around 1.85 Å corresponds to silanol groups involved in strong H bond interactions.

Figure 8: Comparison between the RDF function of our slab model and the RDF function of bulk α-SiO2.

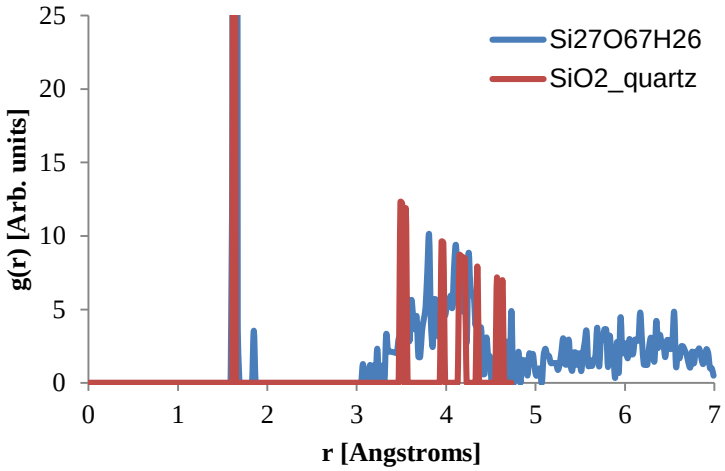

6.2 Silanol number vs. temperature

Our slab model has a silanol number of 6.31 OH/nm^2, whereas the experimental value for fully hydroxylated silica surfaces is 4.9 OH/nm^2. This difference is alleviated by performing a dehydroxylation simulation summarized in Table 2. We observe that silanol number is lowered in the following fashion: 6.31 OH/nm^2, 5.91 OH/nm^2, 5.45 OH/nm^2, and 3.18 OH/nm^2. The dehydroxylation simulation stopped at a silanol number of 3.18 OH/nm^2 because we did not observe any other silanol pair available for dehydroxylation. This is because the condensation reaction simulations do not include the migration of protons on the surface, as has been experimentally observed at temperatures above 673 K.[41]

Table 2: Summary of dehydroxylation energy calculations applied to our slab model.

ΔE_{DFT} (eV)

-	OH/nm^2 = 6.31	OH/nm^2 = 5.91	OH/nm^2 = 5.45	OH/nm^2 = 3.18
ΔE_{DFT} for each pair available for condensation	0.53	0.93	1.83	--
	0.74	2.14	--	--
	0.90	--	--	--
	1.29	--	--	--

The **¡Error! No se encuentra el origen de la referencia.** shows the obtained ilica surface models from the dehydroxylation simulations. The silanol number dependence of the dehydroxylation energy is also showed. The increase in dehydroxylation energy is an indicative of a higher surface reconstruction as the silanol number decreases, and could explain the flattening of slope in **¡Error! No se encuentra el origen de la referencia.**.[41]

Figure 9: Representative surface for each silanol number, dehydroxylation energy for each surface.

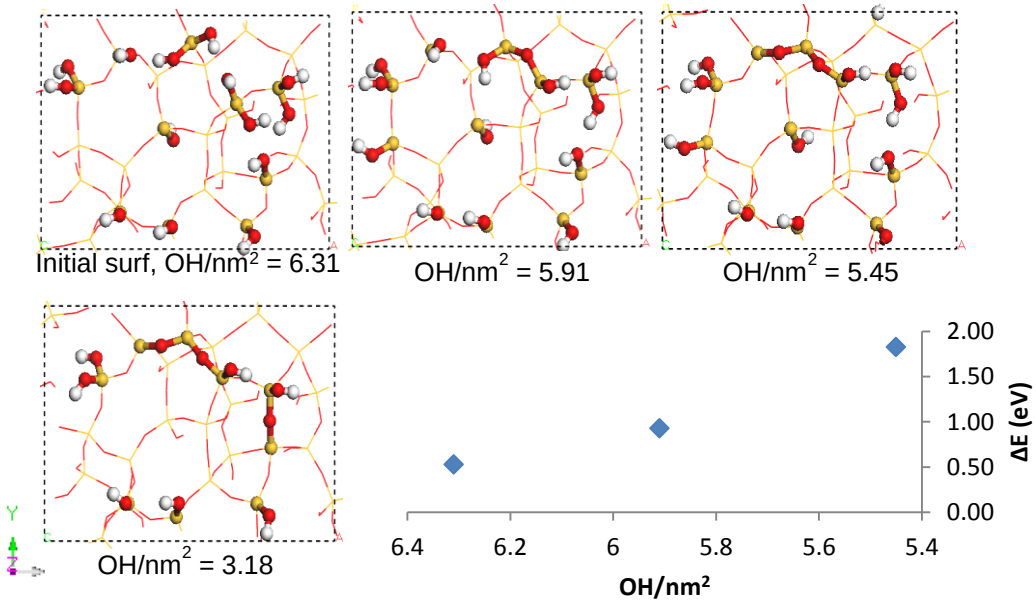

The **¡Error! No se encuentra el origen de la referencia.** shows the temperature s. silanol number dependence calculated using the equation No. 2 with partial water pressures of 10^{-6} bar and 0.01 bar, respectively. The **¡Error! No se ncuentra el origen de la referencia.** also shows the experimental data averaged

from 16 silica samples synthetized with different procedures and with different structural characteristics.[41] We observe excellent agreement between calculated values and experimental data. Moreover, for the range of temperatures evaluated we observe a weak effect of partial water pressures. Hereafter only the partial pressure of 0.01 bar is used for calculations. The partial water pressure of 0.01 bar is typical for HDS processes.[126]

Figure 10: OH/nm2 vs. temperature: ●, average experimental values; ▲, computed values @ 10-5 bar; ■, computed values @ 0.01 bar.

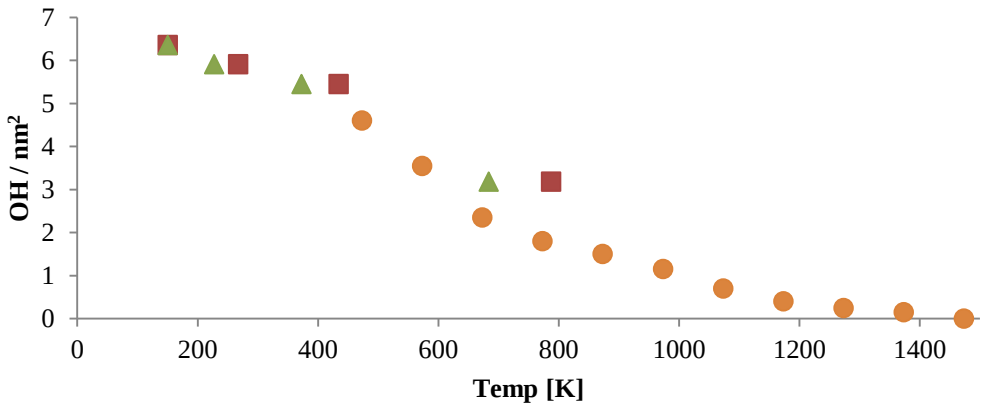

The silanol type distribution at each dehydroxylation step is presented in **¡Error! No se encuentra el origen de la referencia.**. Above 673 K only free isolated silanols and free geminal silanols remain on the surface. The disappearance of vicinal silanols at high temperatures has been also reported in other works.[41] The Table 3 shows the percentage of Si-type atoms at each silanol number: silicon atom bonded to only siloxane bridges (Si type Q_4), silicon atom bonded to three siloxane bridges and one hydroxyl group (Si type Q_3), and silicon atom bonded two siloxane bridges and two hydroxyl groups (Si type Q_2). Experimental data measured using ^{29}Si MAS NMR for as-synthesized SBA-15 and calcined SBA-15 is also presented.[45]

The as-synthesized SBA-15 and the slab model with a silanol number of 6.31 OH/nm^2 evidence similar percentage of Si type Q_3 atoms, whereas a significant

deviation is observed for the Si types Q_4 and Q_2. Both the calcined SBA-15 and the slab with a silanol number of 3.18 OH/nm^2 share a similar percentage of Si type Q_3 atoms, however, now a similar percentage of Si types Q_4 and Q_3 are also observed. From this can be inferred that physical accuracy of slabs models increased after applying the dehydroxylation simulations, the Si type distribution became increasingly approximated to experimental data.

Other fact to note is that the slab model with a silanol number of 6.31 OH/nm^2 is the less accurate in terms of silanol number and Si type distribution. From now and so on, only slab models with silanol numbers of 5.91 OH/nm^2, 5.45 OH/nm^2 and 3.18 OH/nm^2 are used for calculations.

Figure 11: Silanol type distribution as a function of temperature: ✳, isolated silanols; ●, geminal silanols; ◆, vicinal silanols. Lines are for eye-guiding.

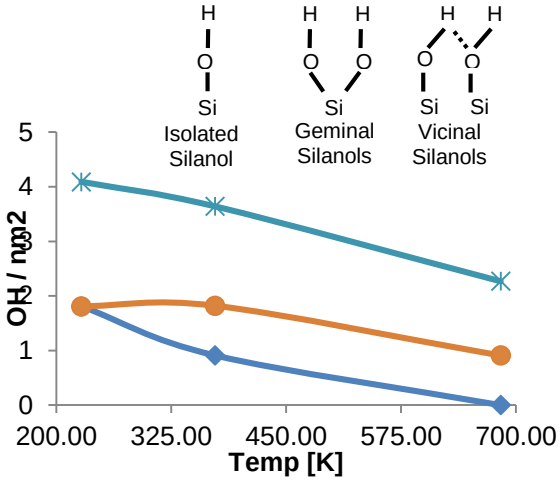

Table 3: Percentage of Si-type atoms bonded to only siloxane bridges.

Silanol number. (OH/nm^2)	Unit cell Formula	% Q_2	% Q_3	% Q_4
6.31	$Si_{27}O_{67}H_{26}$	28.6	42.8	28.6
5.91	$Si_{27}O_{66}H_{24}$	12.5	56.2	31.3
5.45	$Si_{27}O_{65}H_{22}$	11.8	47.0	41.2
3.18	$Si_{27}O_{64}H_{20}$	7.1	35.7	57.2
As-synth. SBA-15 (28ºC) [46]	-	8	41	51

Calcined SBA-15 (773 ºC) [46]	-	4	29	66

6.3 Isomorphic substitutions of Si^{4+} atoms by Al^{3+} and Ti^{4+} atoms

6.3.1 Al^{3+} incorporation

We begin with substitution of Si^{3+} atoms by Al^{3+} atoms (Al/Si ratio of 1/26) on the slab with the silanol number of 5.91 OH/nm^2. This enables us to understand the early stages of substitution of Si atoms by Al atoms in fully hydroxylated silica surfaces.

The Table 4 summarizes the Al^{3+} incorporation on three different Si type atoms: Q_4, Q_3 and Q_2. The Q_4 site has 4 Al-O-Si bridges available for protonation, whereas the Q_3 and Q_2 sites have 3 and 2 Al-O-Si bridges available, respectively. The Si/Al substitutions are listed in descending order of stability: the structure with the most negative value for the formation energy is listed first, whereas the structure having the less negative value for the formation energy is listed at the end.

The more favorable places for substitution are those where the protonated Al-O-Si bridge involves a Si atom type Q_3. This result indicates that Al^{3+} incorporation through post synthesis procedures could be facilitated at low temperatures because the Si atoms type Q_3 are more abundant in surfaces with a higher silanol number.

Table 4: Structural parameters for the isomorphic substitution of Si atoms by Al atoms.

	Structural arrangement	**ΔE (eV)**
Al_{Q3}-OH-Si_{Q3}	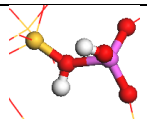	-5.144

Al_{Q4}-OH-Si_{Q3}	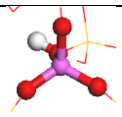	-5.030
Al_{Q4}-OH-Si_{Q3}	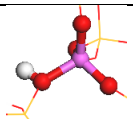	-4.661
Al_{Q2}-OH-Si_{Q3}	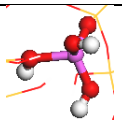	-4.609
Al_{Q4}-OH-Si_{Q3}	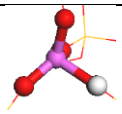	-4.522
Al_{Q3}-OH-Si_{Q4}	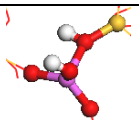	-4.421
Al_{Q2}-OH-Si_{Q4}	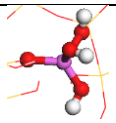	-4.408
Al_{Q4}-OH-Si_{Q4}	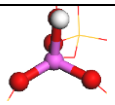	-4.296
Al_{Q3}-OH-Si_{Q3}	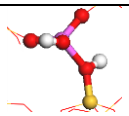	-4.223

Structural distortions are also observed after isomorphic substitution of Si^{4+} atoms by Al^{3+} atoms. The Al-O bond length in case of non-protonated O atoms is on average 0.0898 Å larger than the equivalent Si-O bond length, whereas for protonated O atoms this distance is on average 0.338 Å larger than the corresponding Si-O bond length. This is in quantitative agreement with structural distortions reported for (001) surfaces of modernite, where the Al-bond length is 0.08-0.11 Å and 0.27-0.29 Å larger for non-protonated and protonated Oxygens, respectively.[30]

The **¡Error! No se encuentra el origen de la referencia.** shows how the structure f slabs with silanol numbers of 5.45 OH/nm^2 and 3.18 OH/nm^2 evolve as the Al

content increases. Both surfaces show preference for isomorphic substitution in Q_3 and Q_4 sites. At low Al/Si ratios the O protonation tends to occurs in O atoms bonded to Q_2 and Q_3 sites, whereas at high Al/Si ratios the O atoms bonded to Q_4 sites are preferred for protonation.

The formation energy at different Al/Si ratios is shown in **¡Error! No se encuentra el origen de la referencia.** for the slabs with silanol numbers of 5.45 OH/nm^2 and 3.18 OH/nm^2. Despite the irregular behavior for the surface with a silanol number of 5.45 OH/nm^2; the Al^{3+} incorporation becomes increasingly less favorable as the Al/Si ratio increases. This is in agreement with experimental measurements for Al incorporation using the post-synthesis method on SBA-15,[52] where the Al incorporation at low Al/Si ratios was favored in tetrahedrally coordinated sites. However, it was also observed that octahedral incorporation becomes predominant as the Al loading increases.

Figure 12: Structural changes as the Al content increases: slabs with silanol numbers of 5.45 OH/nm^2 and 3.18 OH/nm^2.

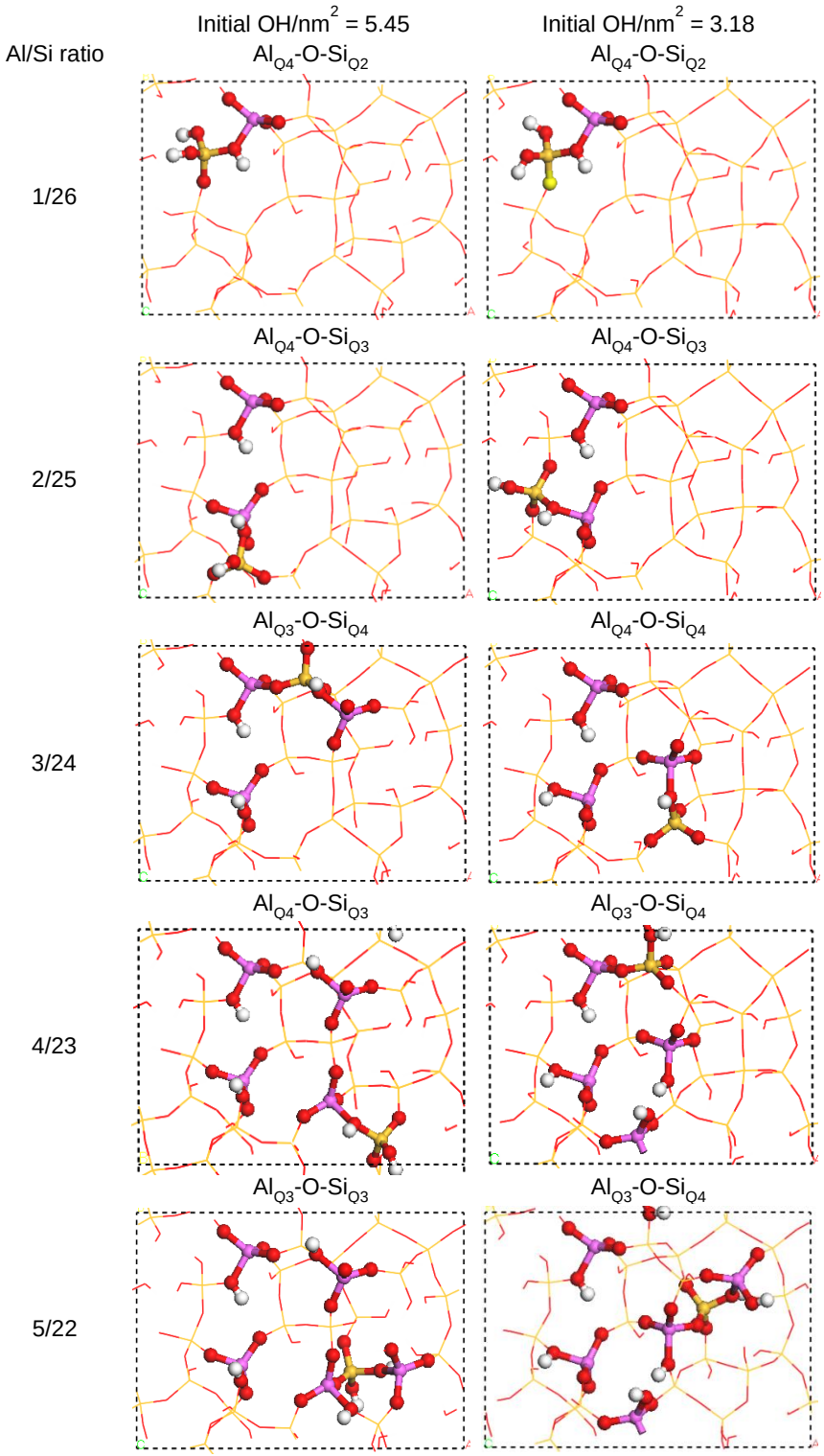

Figure 13: Formation energy as a function of Al/Si ratio: ■, initial silanol number of 5.45 OH/nm2; ◆, initial silanol number of 5.45 OH/nm^2.

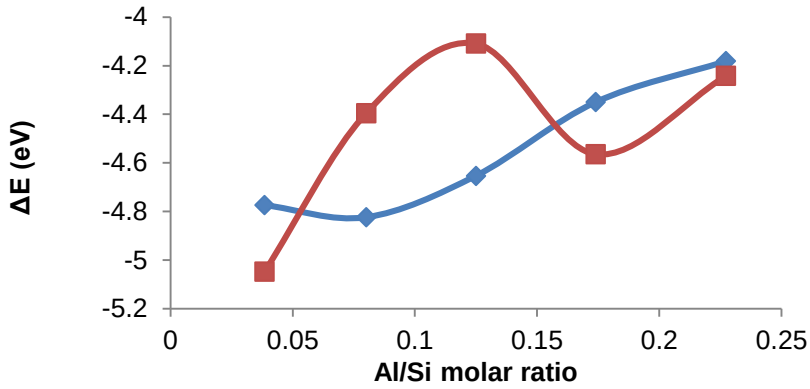

6.3.2 Ti^{4+} incorporation

Now we turn to elucidate the tetrahedral incorporation of Ti^{4+} cations. The surface with a silanol number of 5.45 OH/nm^2 is used for evaluate the Ti^{4+} incorporation at a Ti/Si ratio of 1/26. The **¡Error! No se encuentra el origen de la referencia.** hows the Ti incorporation by isomorphic substitution of Si atom types Q_4, Q_3, and Q_2. We observe that formation energy becomes less negative in the following pattern: $Q_4 < Q_3 < Q_2$, being the Q_4 the most stable site for substitution. This result indicates that at low Ti loadings the isomorphic substitutions are preferred in sites where the Ti^{4+} cation is bonded to four Ti-O-Si bridges.

Figure 14: Isomorphic substitution of Si atoms by Ti atoms in positions Q^4, Q^3, and Q^2 at a Ti/Si ratio of 1/26.

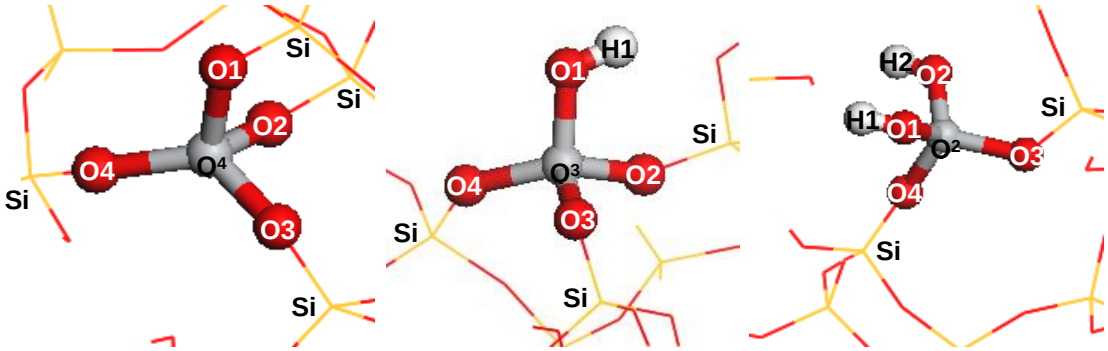

a) Q^4; ΔE = -3.530 eV b) Q^3; ΔE = -2.923 eV c) Q^2; ΔE = -2.367

The structural distortions for each substitution in **¡Error! No se encuentra el origen de la referencia.** are quantified in Table 5 where the column on the right quantifies changes in bond length and bridge angle after substitution. The structural distortions arise regardless the type of substituted Si atom (Q_4, Q_3, and Q_2). Moreover, the Ti-O bond length is on average 0.1976 Å larger than the equivalent Si-O bond length.

The structural distortions are attributed to differences in atomic radius between Ti and Si atoms (Ti atomic radius = 140 pm, Si atomic radius = 110 pm).[127]. For the substitution in the Q_3 site, the Ti-O1-H1 angle evidences a change of 0.183 deg. with respect to the same site before substitution; whereas the Ti-O2-Si2 angle has changed up to 10.92 deg.

Table 5: Ti incorporation on Q_4, Q_3, and Q_2 sites (Ti/Si ratio of 1/26): Ti-O bond lengths and Ti-O-Si angles (see figure 14 for nomenclature, angular changes are reported in absolute values).

	SBA-15 ($Si_{27}O_{65}H_{22}$)	**Ti-SBA-15 ($TiSi_{26}O_{65}H_{22}$)**	**Δ(Ti-SBA-15 - SBA-15)**
Ti in Q_4 site			
Ti-O1 [Å]	1.6352	1.8176	0.1824
Ti-O2 [Å]	1.6533	1.8445	0.1912
Ti-O3 [Å]	1.6530	1.8460	0.1930
Ti-O4 [Å]	1.6691	1.9001	0.2310
Ti-O1-Si1 [deg]	146.2560	149.0076	2.7516
Ti-O2-Si2 [deg]	137.9080	137.3841	-0.5239
Ti-O3-Si3 [deg]	170.9135	162.9062	-8.0073
Ti-O4-Si4 [deg]	147.3213	144.7713	-2.5500
Ti in Q_3 site			
Ti-O1 [Å]	1.6281	1.8231	0.1950
Ti-O2 [Å]	1.6488	1.8520	0.2032
Ti-O3 [Å]	1.6842	1.8806	0.1964
Ti-O4 [Å]	1.6560	1.8553	0.1993
Ti-O1-H1 [deg]	113.6304	113.4466	-0.1838
Ti-O2-Si2 [deg]	144.0747	133.1535	-10.9212

Ti-O3-Si3 [deg]	135.0277	135.7654	0.7377
Ti-O4-Si4 [deg]	139.2217	133.7661	-5.4556
Ti in Q_2 site			
Ti-O1 [Å]	1.6454	1.8385	0.1931
Ti -O2 [Å]	1.6427	1.8132	0.1705
Ti -O3 [Å]	1.6405	1.8639	0.2234
Ti -O4 [Å]	1.6253	1.8184	0.1931
Ti-O1-H1 [deg]	118.7773	126.6554	7.8781
Ti-O2-H2 [deg]	119.8219	125.6877	5.8658
Ti-O3-Si3 [deg]	131.8409	124.5200	-7.3209
Ti-O4-Si4 [deg]	154.1599	149.7869	-4.3730

At the best of our knowledge, the Ti incorporation into the SBA-15 framework has been successfully performed up to a Ti/Si ratio of 1/20 (approx. 0.05).[23] Here we evaluate the Ti incorporation into tetrahedral sites up to a Ti/Si ratio of 5/22 (approx. 0.22). However, the **¡Error! No se encuentra el origen de la referencia.** hows that Ti incorporation becomes less favorable as the Ti/Si ratio increases. This is in agreement with UV-vis diffused reflectance (DRS) measurements of SBA-15 materials modified with Ti by following the post-synthesis procedure with titanium butoxide. [23] The DRS spectra reveal that at a low Ti/Si ratio the Ti^{4+} cations are tetrahedrally incorporated into the SBA-15 framework. However, at Ti/Si ratios above 1/20 the formation of extraframework TiO_2 was detected.

The **¡Error! No se encuentra el origen de la referencia.** shows that preference or Ti^{4+} incorporation in Q_4 sites is conserved at high Ti/Si ratios. However, we also observe that Q_4 sites become less available as the Ti content increases, which could explain both the behavior in **¡Error! No se encuentra el origen de la referencia.** and the experimentally observed Ti incorporation into octahedral sites as Ti content rises.

Figure 15: Formation energy plot as a function of Ti/Si ratio. Line is for eye-guiding

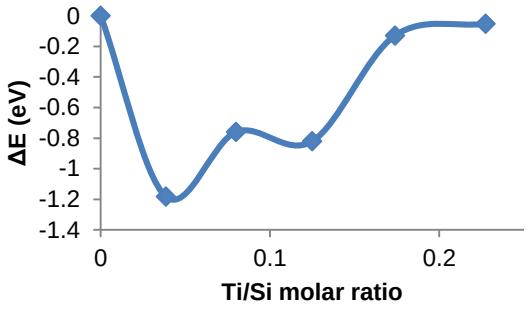

Figure 16: Structural evolution as the Ti/Si ratio increases from 0 to 5/22.

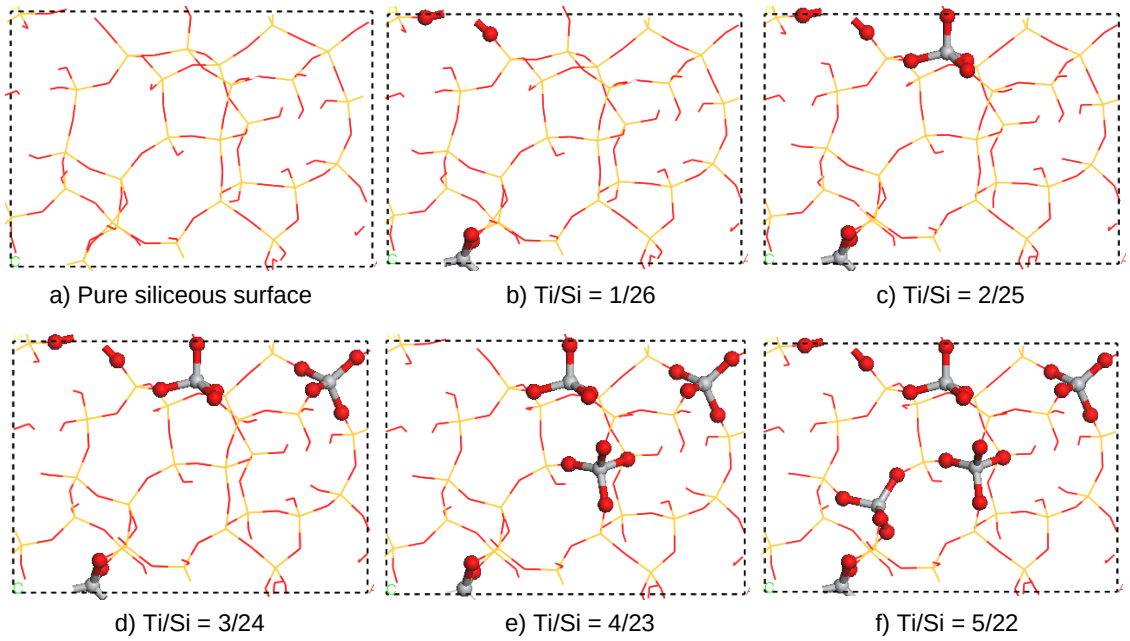

6.4 Brönsted Acid properties

6.4.1 Pure siliceous SBA-15 surface

The **¡Error! No se encuentra el origen de la referencia.** shows the OH-stretching requencies against the O-H bond lengths for the slabs with a silanol number of 5.45 OH/nm^2 and 3.18 OH/nm^2. The OH-stretching frequencies range from 3817 cm^{-1} to 3601 cm^{-1}. This is in qualitative agreement with FT-IR measurements on SBA-15 molecular sieves exhibiting a broad band between 3759 cm^{-1} to 3473 cm^{-1}

assigned to surface OH groups.[47] In agreement with previous works,[30, 37, 128] both surfaces show a linear relationship between the OH-stretching frequencies and the O-H bond lengths; the surface with a silanol number of 5.45 OH/nm^2 has a linear regression coefficient of 0.9839, whereas the surface with a silanol number of 3.18 OH/nm^2 has a regression coefficient of 0.9876. The similarities in slope for both surfaces indicates that chemical microenvironment on the surface (silanol types) not influences the OH-stretching frequency. We inferred that silanol type distribution does not have a significant impact on surface acidity properties. We observe that OH-stretching frequencies might be broadly divided in two domains: A first domain of high frequencies spanning between 3821 cm^{-1} and 3740 cm^{-1} including the isolated and H-bond acceptors silanols; and a second domain of low frequencies ranging from 3724 cm^{-1} and 3601 cm^{-1} corresponding to H-bond donor silanols. This result is in qualitative agreement with experimental IR measurements on silica surfaces:[129] a first band of high frequencies assigned to OH groups not involved in H-bond interactions and H-bond acceptors hydroxyl groups, and a second band of low frequencies assigned to H-bond donor hydroxyl groups.

Figure 17: OH stretching frequencies: ◆, OH/nm^2 = 5.45; ■, OH/nm^2 = 3.18.

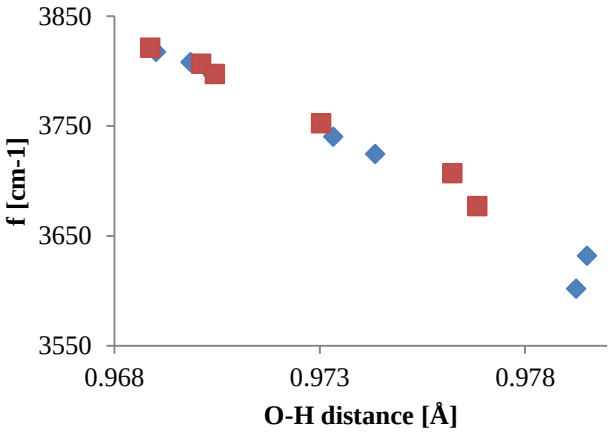

We observe a correlation between the minimal OH-stretching frequency and the silanol number. The lowest frequency for the surface with a silanol number of 5.45 OH/nm^2 is 3601 cm^{-1}, whereas the surface with a silanol number of 3.18 OH/nm^2

shows a minimum frequency of 3677 cm^{-1}. We explain this correlation based on H-bond interactions; the **¡Error! No se encuentra el origen de la referencia.** shows the hydroxyl groups with the two lowest OH-stretching frequencies for the surface with a silanol number of 5.45 OH/nm^2. Both hydroxyls groups are involved in H-bond interactions with surrounding Oxygen atoms, and the OH-stretching frequency decreases as the O-H distances becomes shorter. Compared to the OH-stretching frequency of 3749 cm^{-1} assigned to terminal silanols,[30] the hydroxyl groups with O-H distances of 2.07 Å and 2.04 Å shown a shift of 118 cm^{-1} and 148 cm^{-1} to lower frequencies, respectively. The OH-stretching frequencies of these hydroxyl groups are comparable to the OH-stretching frequencies of Brönsted acid sites (3608 cm^{-1}) in bulk modernite.[30]

Figure 18: H-bond interactions between hydroxyl groups on the surface: a) Hydroxyl groups connected through a siloxane bridge; b) Hydroxyl groups connected at least through a -Si-O-Si-O-Si- bridge.

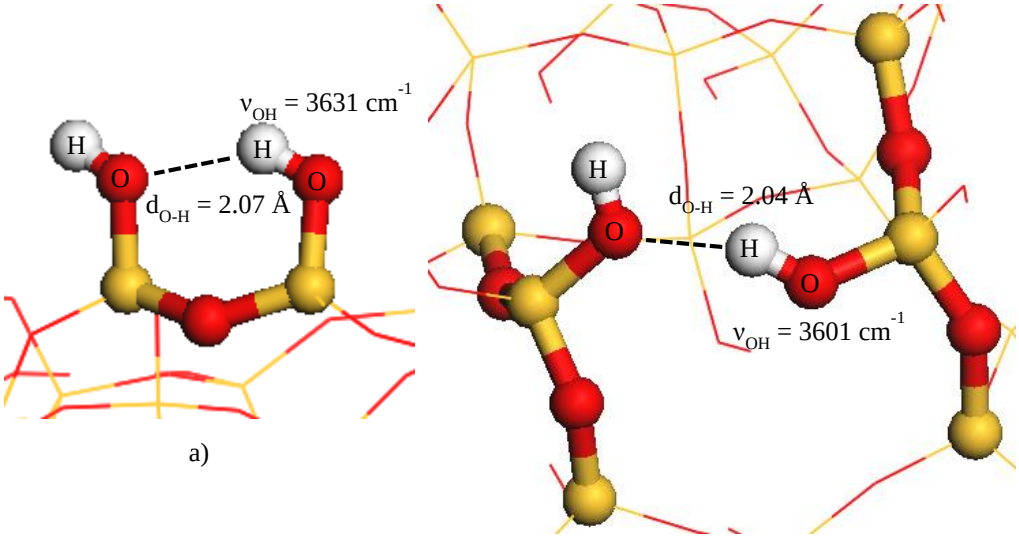

The **¡Error! No se encuentra el origen de la referencia.** shows the correlation etween O-H stretching frequencies and the length of the H-bond interactions for several hydroxyl groups on both surfaces (5.45 OH/nm^2 and 3.18 OH/nm^2); we

observe that OH-stretching frequencies are linearly correlated with the H-bond interaction, with a linear regression coefficient of 0.982.

We conclude that H-bond interactions between surface silanol groups can enhance the surface's acidity strength up to comparable values with the Brönsted acid sites created by Al incorporation in H-modernite zeolites.[130] Moreover, we inferred that use of lower pretreatment temperatures can contribute positively to produce SBA-15 materials with better acidity properties, because H-bond interactions are favored on surfaces with higher silanol numbers.

In previous studies the O-H stretching frequency of 3750 cm^{-1} has been assigned for isolated hydroxyl groups,[30] whereas a O-H stretching of 3608 cm^{-1} has been assigned for Brönsted acid sites.[130] We observe that H-bond interactions can change O-H frequencies of Hydroxyl groups toward those of Brönsted acid sites and hence, as function of H-bond length, the hydroxyl groups can become equally or even more acidic than Brönsted acid sites.

Figure 19: OH-stretching frequency as a function of O-O distance: ■, OH/nm^2 = 5.45; ◆, OH/nm^2 = 3.18.

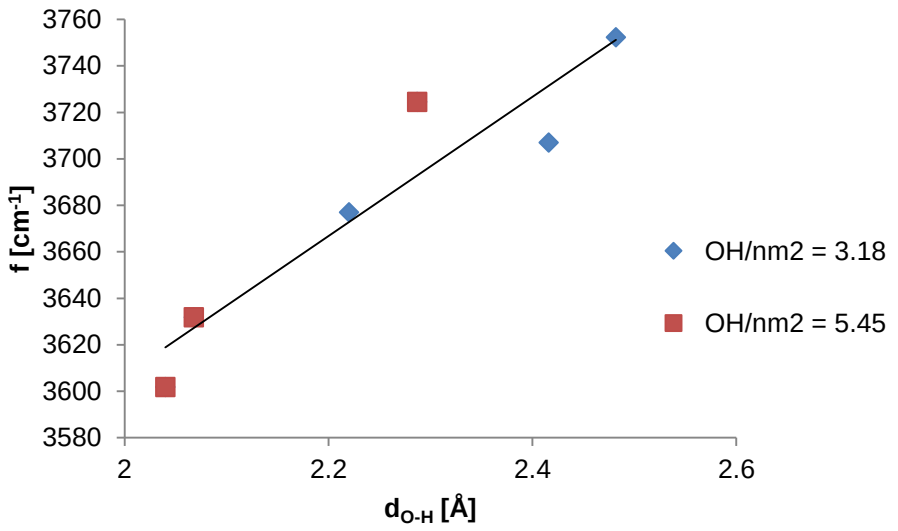

6.4.2 Al^{3+} incorporation

We first evaluate chances in the OH-stretching frequency of silanol groups before and after Al^{3+} incorporation (Al/Si = 5/22), as is shown in **¡Error! No se encuentra el origen de la referencia.**. Besides the silanol group labeled as *c*, no relevant changes in O-H stretching frequency were observed.

Figure 20: O-H stretching frequency in selected Hydroxyl groups on the surface: ◆, SBA-15; ■, Al-SBA-15 (Al/Si = 5/22).

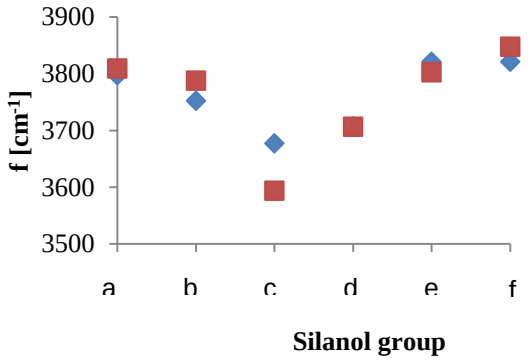

The **¡Error! No se encuentra el origen de la referencia.** offers an explanation for he behavior observed in silanol labeled as *c*, the structural distortion due to the Al^{3+} incorporation reinforces the H-bond interaction of the hydroxyl group with a surrounding O atom. The O-H distance after Al^{3+} incorporation (Al/Si) is 0.217 Å shorter than in the pure siliceous surface. It is concluded that the Al^{3+} incorporation does not significantly modify the acidic properties of silanol groups present in the surface before modification. Only small changes in OH-stretching frequencies are due to structural distortions that Al^{3+} incorporation causes.

Figure 21: Detailed view of site c on figure 20.

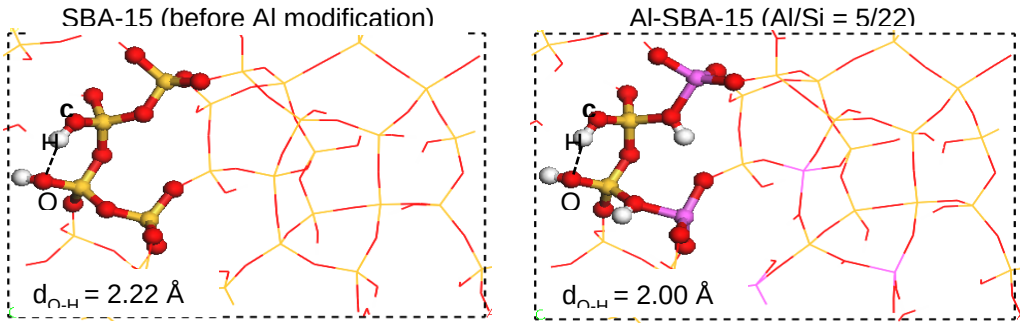

Now we turn to evaluate the OH-stretching frequencies of bridging hydroxyl groups created by the Al/Si substitution and subsequent protonation of an O atom bonded to Al atom. The **¡Error! No se encuentra el origen de la referencia.** shows the H-stretching frequency of a bridging hydroxyl group as the Al/Si content increases. At a Al/Si ratio of 1/26 (as is shown in frame a) the OH-stretching frequency of this hydroxyl group is 55 cm^{-1} higher than the OH-stretching frequency of strong Brönsted acid sites in Modernite zeolite (3608 cm^{-1}).[130] At an Al/Si ratio of 2/25 (frame *b*) the frequency is again lowered until 3431 cm^{-1}, which is 177 cm^{-1} lower than 3608 cm^{-1}.

The shift to lower frequencies is attributed to structural distortions caused by further Al^{3+} incorporation. At the Al/Si ratio of 2/25 the Al^{3+} is incorporated into the same ring containing the Al^{3+} already incorporated (see frames *a* and *b* in **¡Error! No se encuentra el origen de la referencia.**), which induces a significant structural distortion that reinforces the H-bond interaction between the bridging hydroxyl group and a framework O atom. The correlation between OH-stretching frequency and the O-H distance for this bridging hydroxyl group as a function of the Al content is also evidenced in **¡Error! No se encuentra el origen de la referencia.**. However, at higher Al/Si ratios we also observe that further Aluminum incorporation does not changes significantly the OH-stretching frequency. In frames *c*, *d* and *e* the Al^{3+} incorporation occurs in tetrahedral sites not included in

the same ring having the bridging hydroxyl group under study. This clearly indicates that Aluminum incorporation only induces local distortions affecting nearby hydroxyl groups.

We conclude that Al^{3+} incorporation not only creates bridging hydroxyl groups with better acidity properties than silanol groups, but also creates local distortions that induce H-bond interactions between hydroxyl groups and framework Oxygen atoms. It is inferred that not only the electron valence of Al^{3+} atoms is important for modifying the surface acidity properties; the differences in atomic radius between Si and Al are also relevant.

Figure 22: OH-stretching frequency as a function of Al content: Al/Si = 1/26, b) Al/Si = 2/25, c) Al/Si = 3/24, d) Al/Si = 4/23, and e) Al/Si = 5/22.

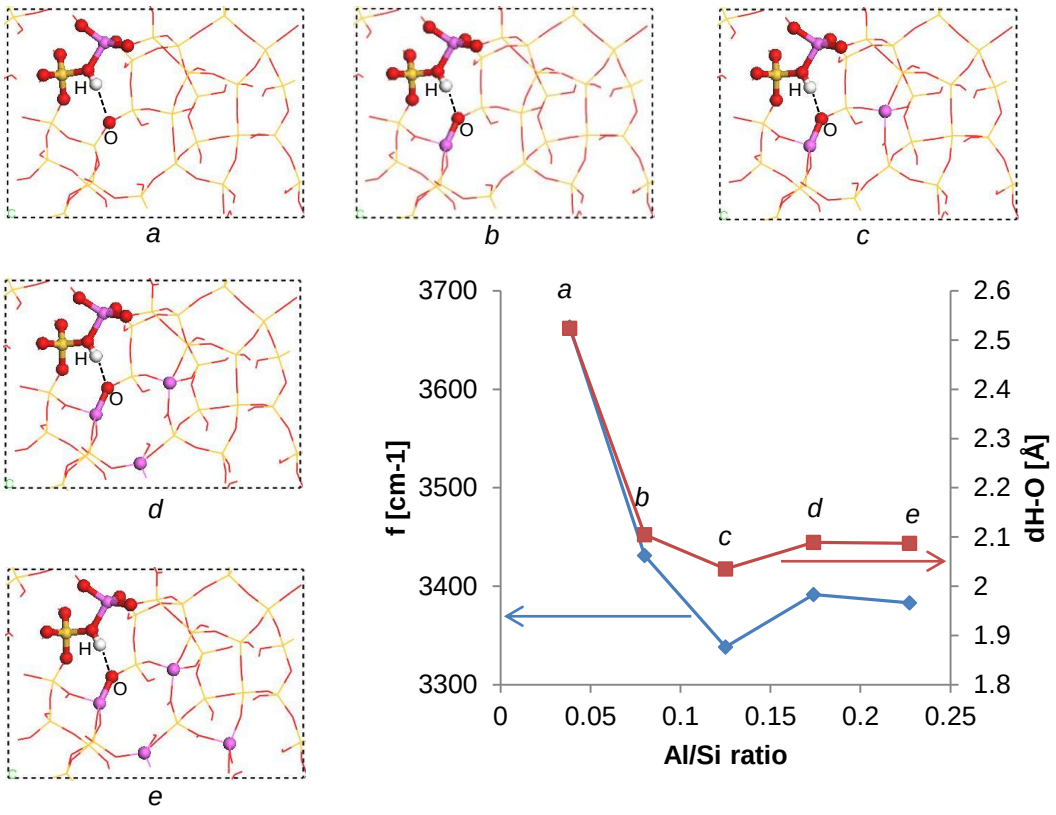

The **¡Error! No se encuentra el origen de la referencia.** presents the OH-tretching frequencies of all bridging hydroxyl groups (frames *a* to *e*) created after

Aluminum incorporation at an Al/Si ratio of 5/22. The OH-stretching frequencies oscillate between 3700 cm^{-1} to 3080 cm^{-1}, which is 49 cm^{-1} and 669 cm^{-1} lower than the OH-stretching frequency of isolated silanol groups (3749 cm^{-1}), respectively. This is in agreement with previous studies where it is reported that Brönsted acid sites formed by Al substitution have stronger acidity properties than silanol groups in pure siliceous materials.[30, 91]

Figure 23: OH-stretching frequency of hydroxyl groups on protonated O at a Al/Si ratio of 5/22.

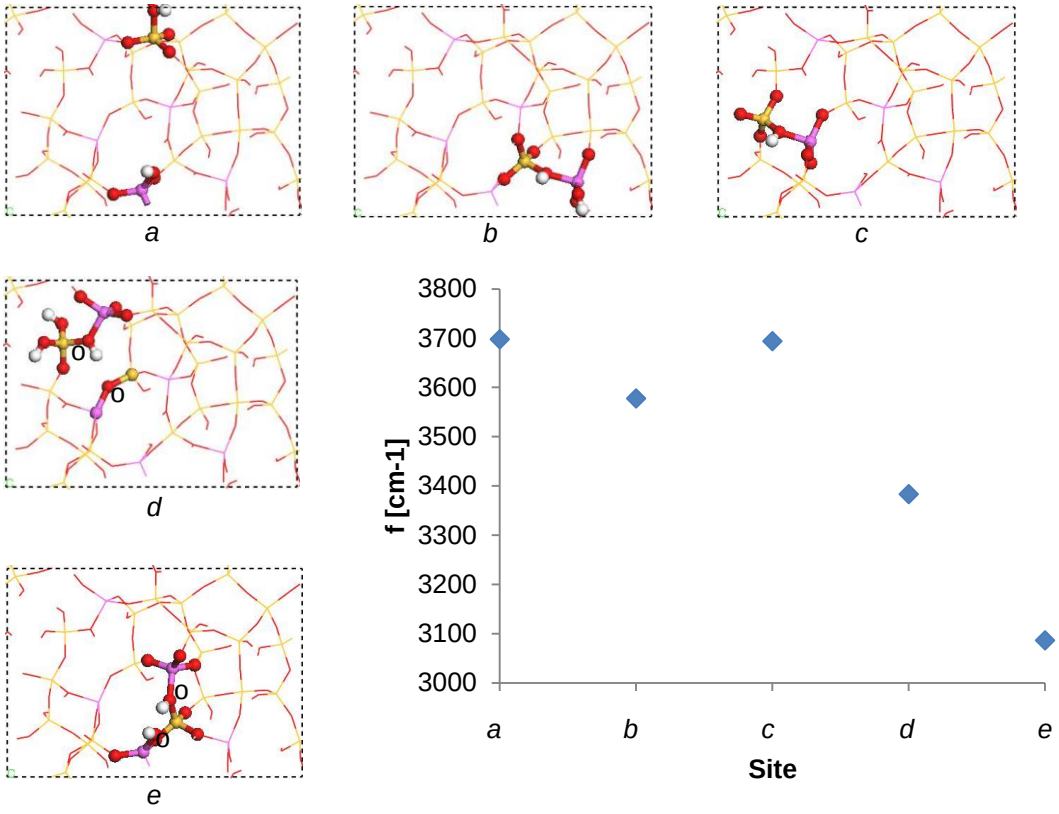

6.4.3 Ti^{4+} incorporation

The **¡Error! No se encuentra el origen de la referencia.** shows how the OH-tretching frequency of one hydroxyl group changes as the Ti content increases. Before Ti^{4+} incorporation the hydroxyl group vibrates at 3817 cm^{-1}. At a Ti/Si ratio the OH-stretching frequency of this hydroxyl group drops to 3808 cm^{-1} and remains nearly constant around this value up to a Ti/Si ratio of 4/23. Finally, at a Ti/Si ratio of 5/22 the vibrational frequency is again lowered until 3801 cm^{-1}.

Significant changes in vibrational frequency are observed when Ti^{4+} incorporation occurs in tetrahedral positions located on the first coordination sphere of the silanol group under study. We see how Ti^{4+} incorporation induces local structural distortions because differences in size between Ti and Si atoms, and this affects the vibrational frequency of surrounding hydroxyl groups, even in absent of H-bond interactions as occur here.

Figure 24: OH-stretching frequency as a function of Ti content: Ti/Si = 1/26, b) Ti/Si = 2/25, c) Ti/Si = 3/24, d) Ti/Si = 4/23, and e) Ti/Si = 5/22.

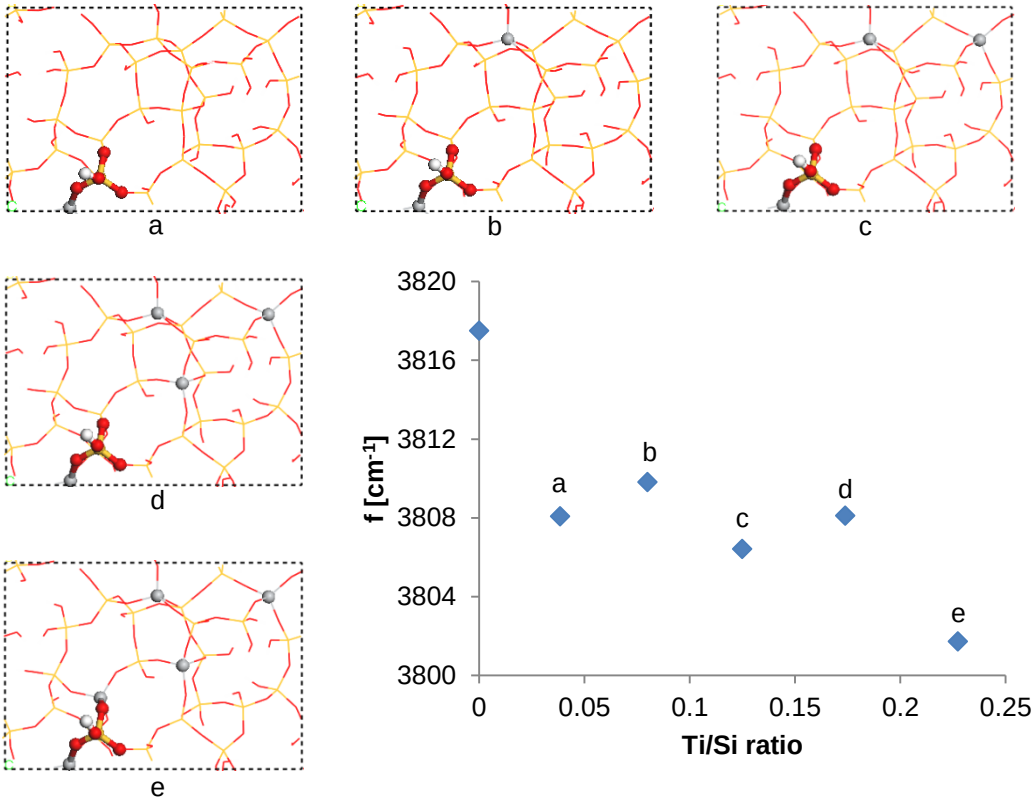

For a surface with a silanol number of 5.45 OH/nm^2, the **¡Error! No se encuentra el origen de la referencia.** shows the surface structure before and after Ti^{4+} incorporation at a Ti/Si ratio of 5/22. Besides local distortions induced by the difference in atomic size between Ti and Si atoms, we do not observe significant structural changes; no rupture neither formation of rings is evidenced.

Figure 25: Surface before and after Ti incorporation at a Ti/Si ratio of 5/22.

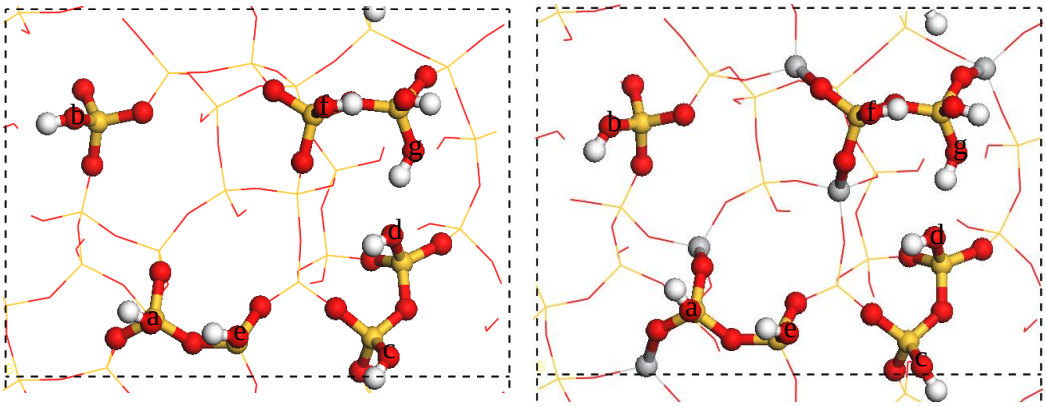

The Table 6 shows a comparison of OH-stretching frequencies before and after Ti^{4+} incorporation for the hydroxyl groups as are labeled in **¡Error! No se encuentra el origen de la referencia.**. The column Δf quantifies the changes in OH-frequency after Ti^{4+} incorporation. After Ti^{4+} incorporation most of hydroxyl groups suffer a decrease in their OH-stretching frequency. In most of cases this is possibly due to local distortions induced by substitution of nearby tetrahedral sites. This generalized decrease in frequency could explain the observed increment on acidity strength in supported SBA-15 catalyst after Ti^{4+} incorporation.[21, 23]

Table 6: Changes in OH-stretching frequency of silanol groups after Ti incorporation (Ti/Al = 5/22).

Hydroxyl group	**f [cm^{-1}]**			
	Pure SBA-15	Ti-SBA-15 (Ti/Si = 5/22)	Δf = $f_{Ti\text{-}SBA\text{-}15} - f_{SBA\text{-}15}$	
a	3817.50	3801.72	-15.78	Decrease
b	3807.98	3515.28	-292.70	Decrease
c	3797.03	3680.85	-116.18	Decrease
d	3740.34	3694.60	-45.74	Decrease
e	3724.52	3771.99	47.47	Increase
f	3631.88	3688.12	56.24	Increase
g	3601.86	3593.92	-7.94	Decrease

The **¡Error! No se encuentra el origen de la referencia.** shows a detailed view of ydroxyl groups labeled as *b* and *c* in **¡Error! No se encuentra el origen de la referencia.**. We observe that H-bond interactions play an important role in decreasing the OH-stretching frequency of these hydroxyl groups. The hydroxyl groups *b* and *c* have a vibrational frequency of 3515 cm^{-1} and 3680 cm^{-1}, respectively. The vibrational frequency of hydroxyl b is just 72 cm^{-1} above the OH-stretching frequency of Brönsted acid sites in Modernite, whereas the vibrational frequency of hydroxyl *c* is 93 cm^{-1} lower than vibrational frequency of Brönsted acid sites in Modernite.[30] This is other indicative that Ti incorporation effectively enhances the acidity properties of the surface, as has been reported in other works.[21, 23]

Figure 26: Detailed view of hydroxyl groups labeled as b and c in Figure 25.

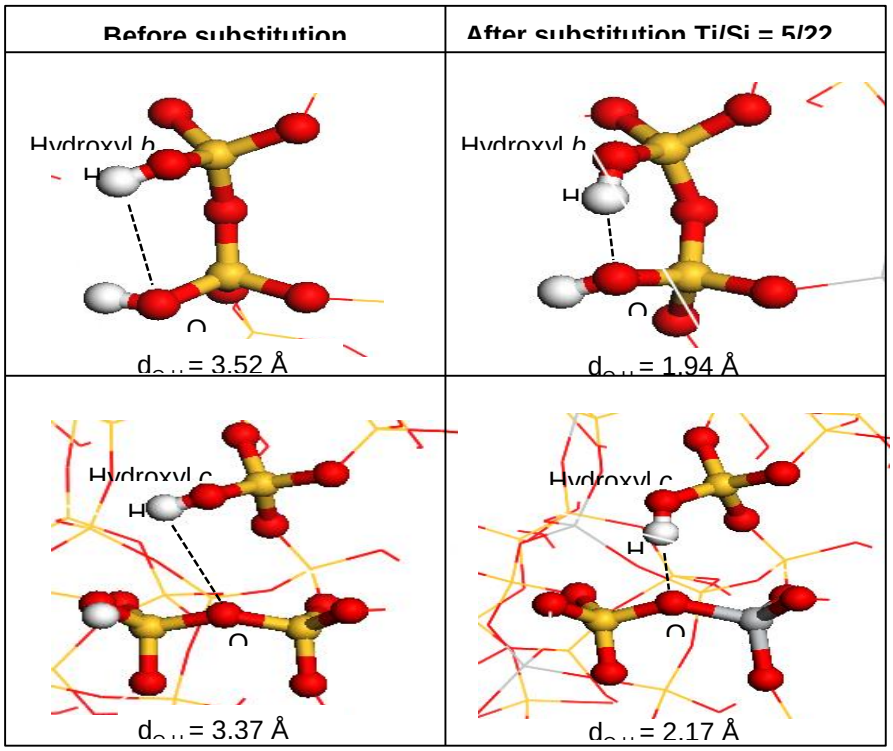

6.5 Adsorption of noble metal cluster

Here is addressed the effect of Al^{3+} incorporation (Al/Si = 5/22) on the metal-support interaction for the adsorption of a Pt-13 (Platinum cluster of 13 atoms). The Table 7 summarizes the four slabs subject to Pt-13 adsorption: the cases 1 and 1-b refer to the slab with silanol number of 5.45 OH/nm^2 before and after Aluminum incorporation, whereas the cases 2 and 2-b correspond to the slab with silanol number of 3.18 OH/nm^2 before and after Aluminum incorporation as well. As mentioned in section 4.3, twenty Pt-13 adsorption sites are evaluated for each slab, giving a total of 80 systems for the four surfaces.

Table 7: Slabs subject to adsorption of Pt-13 clusters.

	Case 1	Case 1-b	Case 2	Case 2-b
Silanol number	5.45	-	3.18	-

Al/Si ratio	0	5/22	0	5/22

The **¡Error! No se encuentra el origen de la referencia.** shows for each slab the verage distribution of covalent bonds between Pt atoms and framework Oxygen atoms. A significant change in distribution is observed after Aluminum incorporation into the surface with a silanol number of 5.45 OH/nm^2 (cases 1 and 1-b). The number of adsorption sites is uniformly distributed in sites with one and three covalent bonds, which indicates better dispersion of supported clusters. However, this effect is not evidenced in the surface with a silanol number of 3.18 OH/nm^2 (cases 2 and 2-b). From this can be inferred that improvements on active phase dispersion after Al^{3+} incorporation are better achieved on surfaces with higher silanol numbers (lower pretreatment temperature), which is in agreement with experimental data reported earlier.[21, 26, 49]

Figure 27: istribution of the number of Pt−silica bond, each case is an average of 20 adsorption sites.

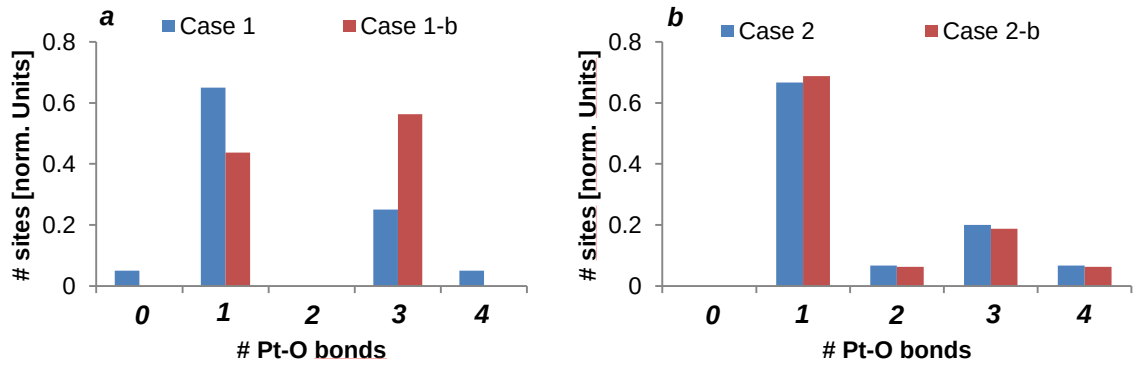

The stability of supported clusters on each surface is plotted in **¡Error! No se encuentra el origen de la referencia.**. In all surfaces we observe a linear dependence of the interaction energy (E_{int}) against the number of Pt-O covalent bonds. The average slope of -3.45 eV per Pt-O bond gives us an estimate of the energy released after formation of a Pt-O bond, being slightly smaller than the

bond energy of a neutral Pt-O dimer (-4.5 eV).[131] The similarity in slopes indicates that Al^{3+} incorporation does not impact the Pt-O bonding mechanism. We inferred that the experimentally reported improvement in Pt dispersion over SBA-15 after Al^{3+} incorporation[26] is mainly due to the availability of hydroxyl groups for Pt-O bond formation. Moreover, the bridging hydroxyl groups formed after Al^{3+} incorporation are more prone to be involved in Pt-O bonds because of their O-H bond distances; longer O-H bond distances are associated to lower dissociation energies.[68]

Figure 28: Cluster−slab interaction energy as a function of the number of Pt-O bonds: a) case 1, b) case 1-b, c) case 2, d) case 2-b.

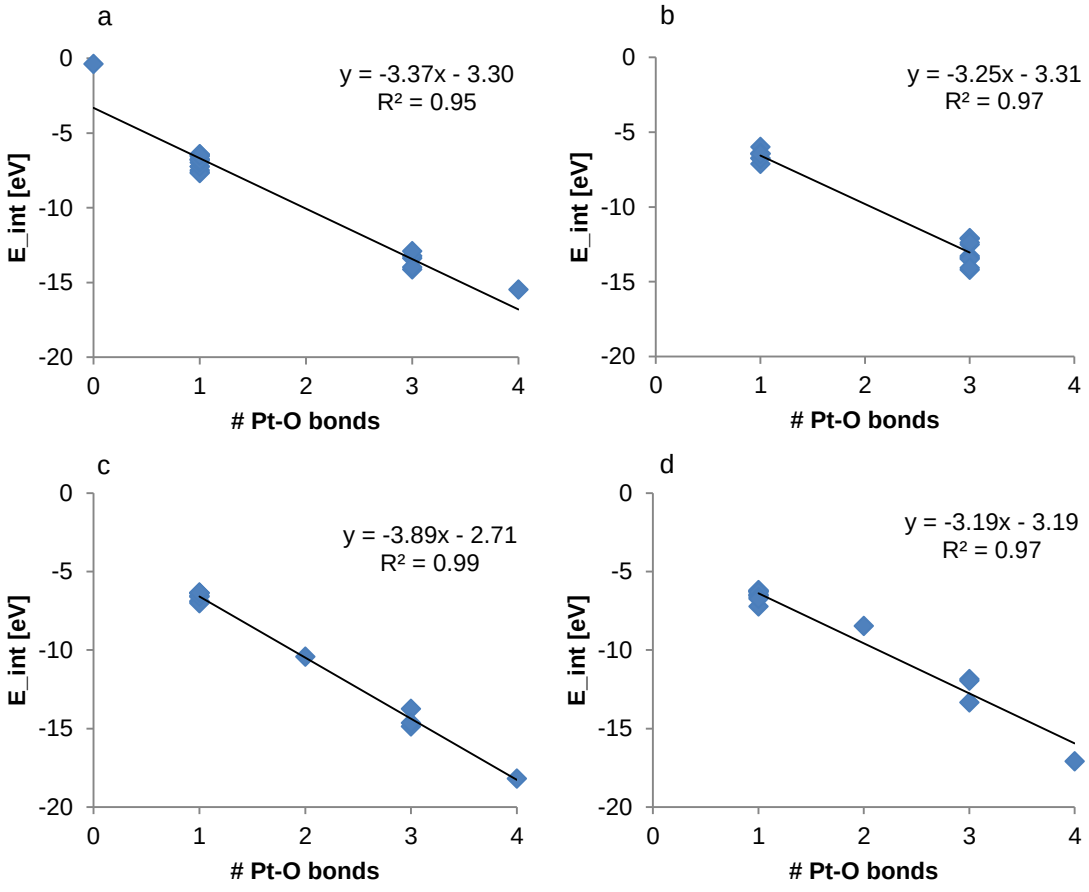

The **¡Error! No se encuentra el origen de la referencia.** shows the average Pt-* N for each slab (where * means Pt-Pt and Pt-O bonds). Compared to the

unsupported Pt-13 cluster, the CN distribution is subject to significant changes in all cases. We do not observe significant effects of Al^{3+} incorporation on the average CN. The number of 5-coordinated Pt atoms is superior in all cases, and the number four coordinated Pt atoms is also significant. The appearance of sub-coordinated Pt atoms increases the ratio of Pt atoms available for binding, this is an indicative of enhanced catalytic activity due to the interaction cluster-support.[113]

Figure 29: Distribution of average CN for Pt 13 clusters averaged over all 20 adsorption sites for each slab. The green bar corresponds to the CN distribution of the unsupported Pt-13 cluster.

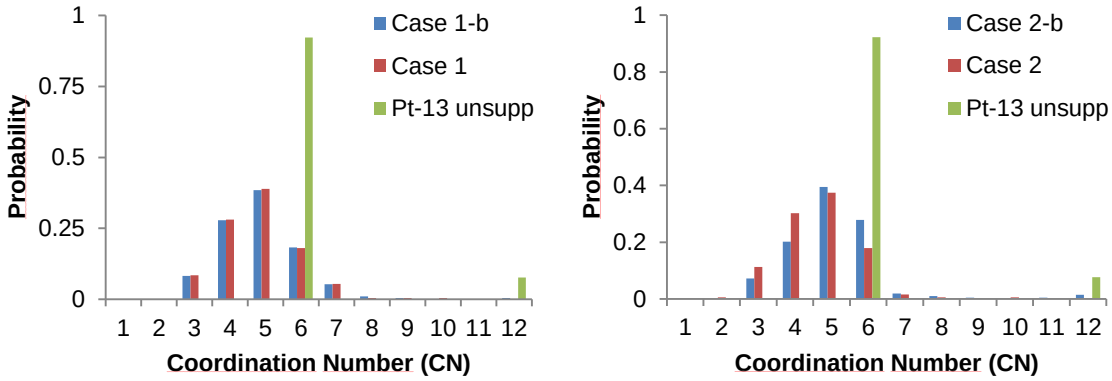

The **¡Error! No se encuentra el origen de la referencia.** shows the averages of t-Pt coordination and the Pt-Pt bond distance as a function of number of Pt-O bonds. From references is known that a decrease in the average coordination number improves the adsorbate binding energy,[113] whereas an increase in bond compression is associated with a weaker adsorbate binding energy.[114] These two competing phenomena arise here because both the average coordination Pt-Pt and the average Pt-Pt distance decrease as the number of Pt-O bonds increase. The bond compression may be attributed to the reduction of coordination number. This result gives place to a complicated composite effect that may involve other variables like cluster size, the surface density of hydroxyl groups, and electron density around the active site, among others.

The electronic charge exchange between the cluster and the support also helps to elucidate the effect of the number of Pt-O covalent bonds.[115] The **¡Error! No se ncuentra el origen de la referencia.** indicates that the Pt cluster linearly becomes more cationic as the number of Pt-O bond rises; this linear behavior is observed for each slab. It is known that adsorbate binding energy also depends on the local electronic density,[132] the electron acceptors compounds preferentially adsorb on negatively charged sites, whereas electron donors ones tend to bind on positively charged sites.

We already indicated that cluster stability depends on the number of Pt-O bonds, which in turn depends on the surface density of hydroxyl groups. We found that Aluminum incorporation influences the cluster stability, with a stronger effect at low temperatures. It is confirmed that more Brönsted acidic surfaces have better interaction with metallic clusters, as the bridging hydroxyl groups are more easily dissociated to form metallic-O bonds. However, we also observe that a complicated effect could also arise as the number of metallic-O bonds increases. We inferred that a compromise between the number of metallic-O bonds must be found in order to obtain and adequate binding strength for an adsorbate. Moreover, the number of metallic-O bonds also determines the charge transfer between the cluster and the adsorbate.

Figure 30: a) average coordination number and b) average Pt-Pt distance of Pt-13 clusters as a function of the number Pt-O bonds. The average is taken over all the 80 systems under study (20 systems per each slab)

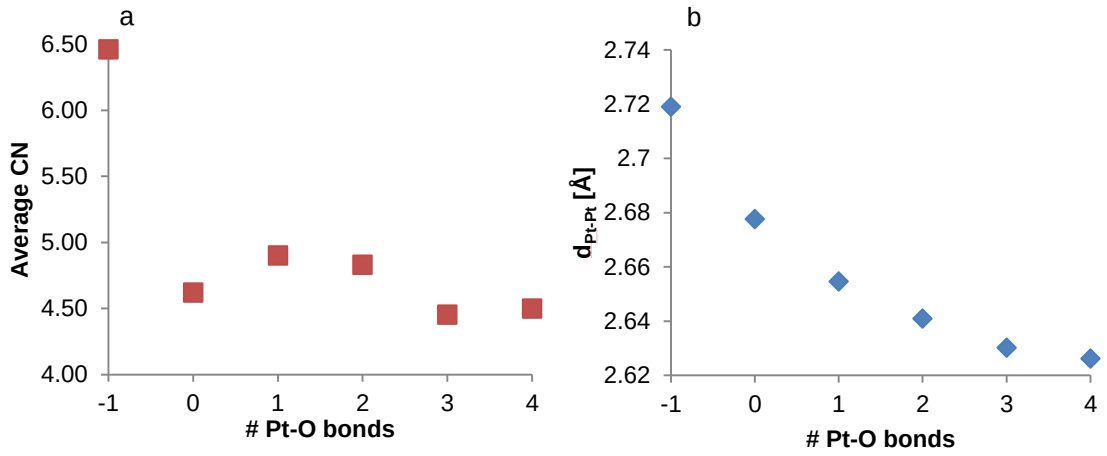

Figure 31: Electronic charge transfer between Pt-13 cluster (Bader charges) and the slab as a function of the number of O atoms bonding to the Pt-13 cluster.

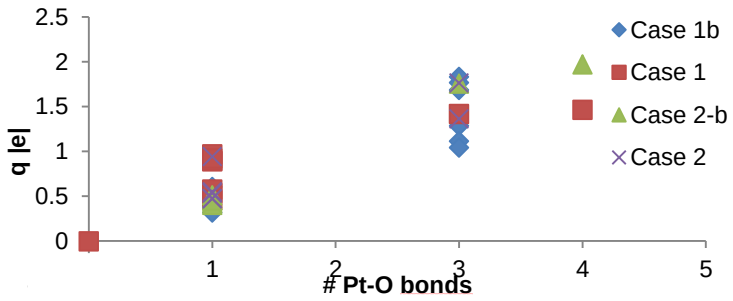

Details of electronic charge distribution of the Pt-13 clusters adsorbed on selected sites for each surface are evidenced in **¡Error! No se encuentra el origen de la referencia.**. We observe that electronic transfer from cluster to support is concentrated on Pt atoms bonded to O atoms and Pt atoms near the cluster-slab interface. This stratified distribution of electronic charge indicates that adsorbate molecules could preferentially bind at the top of cluster or at the cluster-support interfaces, being function of the molecular capability of receive or donate electrons.

Figure 32: Electronic charge for each Pt atom.

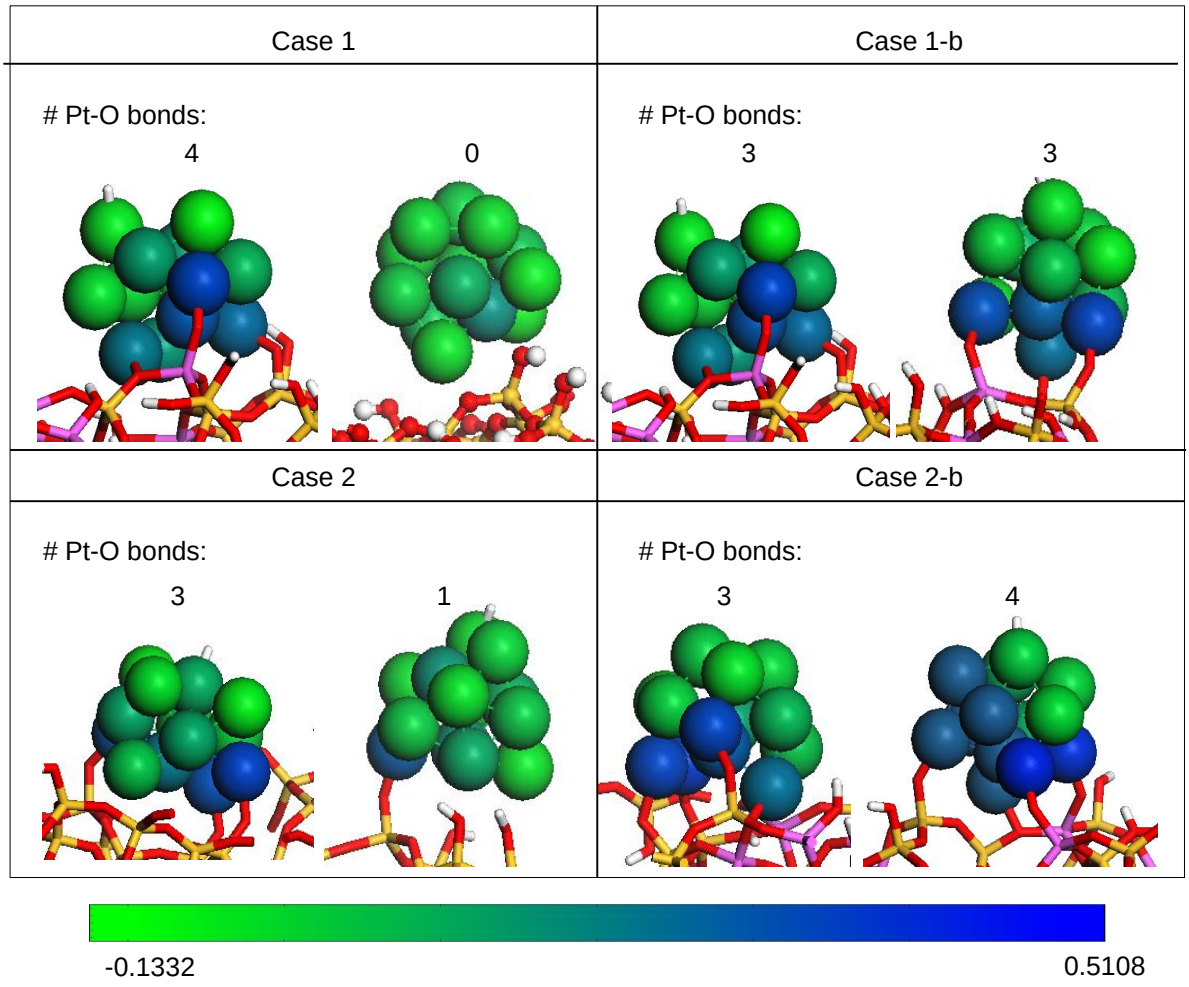

7. CONCLUSIONS AND RECOMMENDATIONS

In this work we have accomplished the theoretical modeling of the internal pore surface of the SBA-15. It is demonstrated that a flat film with periodic boundary conditions can accurately represent the SBA-15's surface. No modeling of the entire pore channel was required for getting information about surface structural features. The main structural motifs of pore surface of the SBA-15 are reproduced: the Si ring size distribution, the silanol surface density, and the silanol type distribution. Compared with earlier works using DFT for addressing the SBA-15's structural units, this work contributes in proposing the use of PBC models for modeling the framework of mesoporous silica materials. The advantages of this approach are evidenced in an adequate modeling of silanol type distribution, which determines the surface reactivity of amorphous silica.

The temperature dependence of silanol number and silanol type distribution has been taken into account. Representative surfaces for different temperatures have been obtained. In future work these surfaces will be useful for elucidation of temperature effects on HPC reaction mechanisms.

Regardless the silanol number and the surface modification, all studied cases showed a linear relationship between the OH-stretching frequency and the O-H bond length. This behavior suggests that surface's chemical environment (the surface silanol type distribution) does not influence the acidity strength of surface hydroxyl groups. Rather, it is noticed that H-bond interactions between hydroxyl groups and surface O atoms strongly lowers the OH-stretching frequencies of surface hydroxyl groups, which increase their acidity strength. Moreover, this local effect is favored on surfaces with higher silanol number. Hence, we inferred that surface acidity of SBA-15 materials is better at lower temperatures. Lower calcination temperatures could be suggested in order to obtain SBA-15 structures with better acidity properties, even without isomorphic substitution with Al or Ti atoms.

Isomorphic substitutions of Si atoms by both Al and Ti atoms were energetically favorable. However, we observe that both the Al and Ti incorporation becomes increasingly less favorable as the Al/Si or Ti/Si ratios increase. This behavior explains the appearance of substitutional species in octahedral sites, which do not contribute to enhance the Brönsted acid surface properties.

Preferential sites for isomorphic substitution are identified for both Al and Ti species. In case of Al incorporation, the more favorable places for substitution are those where the protonated Al-O-Si bridge involves a Si atom type Q_3, which suggest that Al^{3+} incorporation through post synthesis procedures could be facilitated at low temperatures because the Si atoms type Q_3 are more abundant in surfaces with a higher silanol number. In case of Ti incorporation, the Q_4 site is identified as the preferred site for substitution. This result indicates that at low Ti loadings the isomorphic substitutions are preferred in sites where the Ti^{4+} cation is bonded to four Ti-O-Si bridges.

We noticed that differences in atomic size between Si atoms and Al or Ti atoms contribute to changes in surface acidity. The Al^{3+} incorporation not only creates stronger Brönsted acid sites, but also generates local distortions inducing additional H-bond interactions between surface hydroxyl groups and framework O atoms. In this case, not only the Aluminum electronic valence is important for changing the surface acidity properties; differences in the atomic radius between Si and Al play a relevant role. Moreover, we observe a generalized decrease in OH-stretching frequencies after Ti^{4+} incorporation. In most of cases that was attributed to local distortions induced by substitution of tetrahedral sites near to surface hydroxyl groups. This generalized decrease in frequency could explain the observed increment on acidity strength in supported SBA-15 catalyst after Ti^{4+} incorporation.

Future work must be focused on determining changes of adsorption energies after isomorphic substitutions. The enhanced population of hydroxyl groups could be relevant for tuning bifunctional HPC catalysts.

The adsorption calculations of Pt clusters on surfaces with varying degrees of silanol number and Aluminum content were useful to infer that improvements on active phase dispersion after Al^{3+} incorporation are better achieved on surfaces with higher silanol number (lower pretreatment temperature), which is in agreement with reported experimental data.

We found that Al^{3+} incorporation does no change the Pt-O bonding mechanisms. Rather, the improvement in Pt dispersion is mainly due to the availability of bridging hydroxyl groups after isomorphic substitutions.

We observed significant charge depletion in Pt atoms around the cluster-silica interface. This stratified distribution of electronic charge suggests the existence of preferential adsorption sites on the cluster itself. Future work could be focused on determining the effects of this electronic distribution on adsorption of relevant molecules for HPC processes.

In all cases we observed that after adsorption the average coordination number of Pt cluster was lowered. Moreover, the average Pt-Pt distance was reduced as the number of Pt-O bonds increases, with the subsequence dependence of total electronic charge transfer between the Pt cluster and the surface. Additional work must be performed in order to elucidate the effect of these complex phenomena on catalytic activity; insights in tuning of energy position of d-band center and changes of frontier orbital can be obtained from these calculations.

8. REFERENCES

1. Union, E. Fuel Regulations European Union. https://www.dieselnet.com/standards/eu/fuel.php#intro (accessed 2015).
2. Furimsky, E.; Massoth, F. E., Deactivation of hydroprocessing catalysts. *Catalysis Today* **1999,** *52* (4), 381-495.
3. Salvi, B. L.; Subramanian, K. A.; Panwar, N. L., Alternative fuels for transportation vehicles: A technical review. *Renewable and Sustainable Energy Reviews* **2013,** *25*, 404-419.
4. Huirache-Acuña, R.; Nava, R.; Peza-Ledesma, C.; Lara-Romero, J.; Alonso-Núez, G.; Pawelec, B.; Rivera-Muñoz, E., SBA-15 Mesoporous Silica as Catalytic Support for Hydrodesulfurization Catalysts—Review. *Materials* **2013,** *6* (9), 4139-4167.
5. Ancheyta, J.; Rana, M. S.; Furimsky, E., Hydroprocessing of heavy oil fractions. *Catalysis Today* **2005,** *109* (1–4), 1-2.
6. Maity, S. K.; Blanco, E.; Ancheyta, J.; Alonso, F.; Fukuyama, H., Early stage deactivation of heavy crude oil hydroprocessing catalysts. *Fuel* **2012,** *100*, 17-23.
7. Rayo, P.; Ramírez, J.; Torres-Mancera, P.; Marroquín, G.; Maity, S. K.; Ancheyta, J., Hydrodesulfurization and hydrocracking of Maya crude with P-modified NiMo/Al2O3 catalysts. *Fuel* **2012,** *100*, 34-42.
8. Ding, L.; Zheng, Y.; Yang, H.; Parviz, R., LCO hydrotreating with Mo-Ni and W-Ni supported on nano- and micro-sized zeolite beta. *Applied Catalysis A: General* **2009,** *353* (1), 17-23.
9. Taguchi, A.; Schüth, F., Ordered mesoporous materials in catalysis. *Microporous and Mesoporous Materials* **2005,** *77* (1), 1-45.
10. Okamoto, Y.; Breysse, M.; Murali Dhar, G.; Song, C., Effect of support in hydrotreating catalysis for ultra clean fuels. *Catalysis Today* **2003,** *86* (1–4), 1-3.
11. Maclachlan, M. J.; Shopsowitz, K. E.; Hamad, W. Y.; Qi, H., Inorganic mesoporous materials with chiral nematic structures and preparation method thereof. Google Patents: 2011.
12. Huang, L.; Huang, Q.; Xiao, H.; Eic, M., Al-MCM-48 as a potential hydrotreating catalyst support: I – Synthesis and adsorption study. *Microporous and Mesoporous Materials* **2008,** *111* (1–3), 404-410.
13. Zhang, P.; Zhou, Y.; Fan, M.; Jiang, P., Catalytic performance of PdCl2/Cu-HMS: Influence of hydrophobicity and structure of molecular sieves. *Applied Surface Science* **2014,** *295*, 50-53.
14. Zhao, D.; Huo, Q.; Feng, J.; Chmelka, B. F.; Stucky, G. D., Nonionic Triblock and Star Diblock Copolymer and Oligomeric Surfactant Syntheses of Highly Ordered, Hydrothermally Stable, Mesoporous Silica Structures. *J. Am. Chem. Soc.* **1998,** *120* (24), 6024-6036.
15. Zhao, D.; Feng, J.; Huo, Q.; Melosh, N.; Fredrickson, G. H.; Chmelka, B. F.; Stucky, G. D., Triblock Copolymer Syntheses of Mesoporous Silica with Periodic 50 to 300 Angstrom Pores. *Science* **1998,** *279* (5350), 548-552.
16. Boahene, P. E.; Soni, K. K.; Dalai, A. K.; Adjaye, J., Application of different pore diameter SBA-15 supports for heavy gas oil hydrotreatment using FeW catalyst. *Applied Catalysis A: General* **2011,** *402* (1–2), 31-40.
17. Rahmat, N., A.Z. Abdullah and A.R. Mohamed, A review: Mesoporous santa barbara amorphous-15, types, synthesis and its applications towards biorefinery production. *American Journal of Applied Sciences* **2010,** *7* (12), 1579 - 1586.

18. Kruk, M.; Jaroniec, M.; Ko, C. H.; Ryoo, R., Characterization of the Porous Structure of SBA-15. *Chemistry of Materials* **2000,** *12* (7), 1961-1968.
19. Sundaramurthy, V.; Eswaramoorthi, I.; Dalai, A. K.; Adjaye, J., Hydrotreating of gas oil on SBA-15 supported NiMo catalysts. *Microporous and Mesoporous Materials* **2008,** *111* (1–3), 560-568.
20. Byambajav, E.; Ohtsuka, Y., Hydrocracking of asphaltene with metal catalysts supported on SBA-15. *Applied Catalysis A: General* **2003,** *252* (1), 193-204.
21. Olivas, A.; Zepeda, T. A., Impact of Al and Ti ions on the dispersion and performance of supported NiMo(W)/SBA-15 catalysts in the HDS and HYD reactions. *Catalysis Today* **2009,** *143* (1–2), 120-125.
22. Fedeyko, J. M.; Vlachos, D. G.; Lobo, R. F., Understanding the differences between microporous and mesoporous synthesis through the phase behavior of silica. *Microporous and Mesoporous Materials* **2006,** *90* (1–3), 102-111.
23. Nava, R.; Ortega, R. A.; Alonso, G.; Ornelas, C.; Pawelec, B.; Fierro, J. L. G., CoMo/Ti-SBA-15 catalysts for dibenzothiophene desulfurization. *Catalysis Today* **2007,** *127* (1–4), 70-84.
24. Lei, Z.; Gao, L.; Shui, H.; Chen, W.; Wang, Z.; Ren, S., Hydrotreatment of heavy oil from a direct coal liquefaction process on sulfided Ni–W/SBA-15 catalysts. *Fuel Processing Technology* **2011,** *92* (10), 2055-2060.
25. Benesi, H. A.; Winquist, B. H. C., Surface Acidity of Solid Catalysts. In *Advances in Catalysis*, D.D. Eley, H. P.; Paul, B. W., Eds. Academic Press: 1979; Vol. Volume 27, pp 97-182.
26. Kanda, Y.; Aizawa, T.; Kobayashi, T.; Uemichi, Y.; Namba, S.; Sugioka, M., Preparation of highly active AlSBA-15-supported platinum catalyst for thiophene hydrodesulfurization. *Applied Catalysis B: Environmental* **2007,** *77* (1–2), 117-124.
27. Martinez, U.; Pacchioni, G., Interaction of CO, CO2 and CH4 with mesoporous organosilica: Periodic DFT calculations with dispersion corrections. *Microporous and Mesoporous Materials* **2010,** *129* (1–2), 62-67.
28. Keil, F. J., Complexities in modeling of heterogeneous catalytic reactions. *Computers & Mathematics with Applications* **2013,** *65* (10), 1674-1697.
29. Hansen, N.; Keil, F. J., Multiscale Modeling of Reaction and Diffusion in Zeolites: From the Molecular Level to the Reactor. *Soft Materials* **2011,** *10* (1-3), 179-201.
30. Bucko, T.; Benco, L.; Demuth, T.; Hafner, J., Ab initio density functional investigation of the (001) surface of mordenite. *The Journal of Chemical Physics* **2002,** *117* (15), 7295-7305.
31. Hanwell, M.; Curtis, D.; Lonie, D.; Vandermeersch, T.; Zurek, E.; Hutchison, G., Avogadro: an advanced semantic chemical editor, visualization, and analysis platform. *J Cheminform* **2012,** *4* (1), 1-17.
32. Hafner, J., Materials simulations using VASP—a quantum perspective to materials science. *Computer Physics Communications* **2007,** *177* (1–2), 6-13.
33. Kresse, G.; Furthmüller, J., Efficient iterative schemes for \textit{ab initio} total-energy calculations using a plane-wave basis set. *Physical Review B* **1996,** *54* (16), 11169-11186.
34. Kresse, G.; Furthmüller, J., Efficiency of ab-initio total energy calculations for metals and semiconductors using a plane-wave basis set. *Computational Materials Science* **1996,** *6* (1), 15-50.
35. Perdew, J. P.; Burke, K.; Ernzerhof, M., Generalized Gradient Approximation Made Simple. *Physical Review Letters* **1996,** *77* (18), 3865-3868.

36. Hafner, J.; Benco, L.; Bučko, T., Acid-based Catalysis in Zeolites Investigated by Density-Functional Methods. *Top Catal* **2006,** *37* (1), 41-54.
37. Tielens, F.; Gervais, C.; Lambert, J. F.; Mauri, F.; Costa, D., Ab Initio Study of the Hydroxylated Surface of Amorphous Silica: A Representative Model. *Chemistry of Materials* **2008,** *20* (10), 3336-3344.
38. Ewing, C. S.; Hartmann, M. J.; Martin, K. R.; Musto, A. M.; Padinjarekutt, S. J.; Weiss, E. M.; Veser, G.; McCarthy, J. J.; Johnson, J. K.; Lambrecht, D. S., Structural and Electronic Properties of Pt13 Nanoclusters on Amorphous Silica Supports. *The Journal of Physical Chemistry C* **2015,** *119* (5), 2503-2512.
39. Islam, M. M.; Costa, D.; Calatayud, M.; Tielens, F., Characterization of Supported Vanadium Oxide Species on Silica: A Periodic DFT Investigation. *The Journal of Physical Chemistry C* **2009,** *113* (24), 10740-10746.
40. Ewing, C. S.; Bhavsar, S.; Veser, G.; McCarthy, J. J.; Johnson, J. K., Accurate Amorphous Silica Surface Models from First-Principles Thermodynamics of Surface Dehydroxylation. *Langmuir* **2014,** *30* (18), 5133-5141.
41. Zhuravlev, L. T., The surface chemistry of amorphous silica. Zhuravlev model. *Colloids and Surfaces A: Physicochemical and Engineering Aspects* **2000,** *173* (1–3), 1-38.
42. Lee, J. G., *Computational Materials Science: An Introduction*. Taylor & Francis: 2011.
43. Chao, M.-C.; Chang, C.-H.; Lin, H.-P.; Tang, C.-Y.; Lin, C.-Y., Morphological control on SBA-15 mesoporous silicas via a slow self-assembling rate. *J. Mater. Sci.* **2009,** *44* (24), 6453-6462.
44. Choi, M.; Heo, W.; Kleitz, F.; Ryoo, R., Facile synthesis of high quality mesoporous SBA-15 with enhanced control of the porous network connectivity and wall thickness. *Chemical Communications* **2003,** (12), 1340-1341.
45. Benamor, T.; Vidal, L.; Lebeau, B.; Marichal, C., Influence of synthesis parameters on the physico-chemical characteristics of SBA-15 type ordered mesoporous silica. *Microporous and Mesoporous Materials* **2012,** *153* (0), 100-114.
46. Koch, W.; Holthausen, M. C.; Baerends, E. J., *A Chemist's Guide to Density Functional Theory*. FVA-Frankfurter Verlagsanstalt GmbH: 2001.
47. Wang, Z.; Wang, D.; Zhao, Z.; Chen, Y.; Lan, J., A DFT study of the structural units in SBA-15 mesoporous molecular sieve. *Computational and Theoretical Chemistry* **2011,** *963* (2–3), 403-411.
48. Garg, S.; Soni, K.; Kumaran, G. M.; Kumar, M.; Gupta, J. K.; Sharma, L. D.; Dhar, G. M., Effect of Zr-SBA-15 support on catalytic functionalities of Mo, CoMo, NiMo hydrotreating catalysts. *Catal. Today* **2008,** *130* (2–4), 302-308.
49. Sugioka, M.; Aizawa, T.; Kanda, Y.; Kurosaka, T.; Uemichi, Y.; Namba, S., Catalytic performance of mesoporous silica SBA-15-supported noble metals for thiophene hydrodesulfurization. In *Studies in Surface Science and Catalysis*, R. Aiello, G. G.; Testa, F., Eds. Elsevier: 2002; Vol. Volume 142, pp 739-746.
50. Henkelman, G.; Arnaldsson, A.; Jónsson, H., A fast and robust algorithm for Bader decomposition of charge density. *Computational Materials Science* **2006,** *36* (3), 354-360.
51. Klimova, T.; Peña, L.; Lizama, L.; Salcedo, C.; Gutiérrez, O. Y., Modification of Activity and Selectivity of NiMo/SBA-15 HDS Catalysts by Grafting of Different Metal Oxides on the Support Surface. *Industrial & Engineering Chemistry Research* **2009,** *48* (3), 1126-1133.

52. Klimova, T.; Reyes, J.; Gutiérrez, O.; Lizama, L., Novel bifunctional NiMo/Al-SBA-15 catalysts for deep hydrodesulfurization: Effect of support Si/Al ratio. *Applied Catalysis A: General* **2008,** *335* (2), 159-171.
53. Chandra Mouli, K.; Soni, K.; Dalai, A.; Adjaye, J., Effect of pore diameter of Ni–Mo/Al-SBA-15 catalysts on the hydrotreating of heavy gas oil. *Applied Catalysis A: General* **2011,** *404* (1–2), 21-29.
54. Esquivel, G. M.; Ramírez, J.; Gutiérrez-Alejandre, A., HDS of 4,6-DMDBT over NiW/Al-SBA15 catalysts. *Catal. Today* **2009,** *148* (1–2), 36-41.
55. Gómez-Cazalilla, M.; Infantes-Molina, A.; Moreno-Tost, R.; Maireles-Torres, P. J.; Mérida-Robles, J.; Rodríguez-Castellón, E.; Jiménez-López, A., Al-SBA-15 as a support of catalysts based on chromium sulfide for sulfur removal. *Catal. Today* **2009,** *143* (1–2), 137-144.
56. Tang, Y. N.; Li, C. G.; Chen, W. G.; Dai, X. Q., Geometric Stability, Electronic Structure and Reactivity of Pt <inf>4</inf> Cluster Supported On Defective Graphene. *Integrated Ferroelectrics* **2015,** *159* (1), 57-65.
57. Chill, W. T. a. S. Bader Charge Analysis. http://theory.cm.utexas.edu/henkelman/research/bader/.
58. Carter, E. A., Challenges in Modeling Materials Properties Without Experimental Input. *Science* **2008,** *321* (5890), 800-803.
59. Tsybukh, R. A comparative study of platinum nanodeposits on HOPG (0001), MnO(100) and MnOx/MnO(100) surfaces by STM and AFM after heat treatment in UHV, O2 , CO and H2. Leiden University, Netherlands, 2010.
60. Arrouvel, C.; Breysse, M.; Toulhoat, H.; Raybaud, P., A density functional theory comparison of anatase (TiO2)- and γ-Al2O3-supported MoS2 catalysts. *Journal of Catalysis* **2005,** *232* (1), 161-178.
61. Schutte, C. J. H.; Pretorius, J. A., *A computational study of the molecular and crystal structure and selected physical properties of octahydridosilasequioxane–(Si2O3H2)4. I. Electronic and structural aspects*. 2011; Vol. 467, p 928-953.
62. Navarro, R.; Pawelec, B.; Fierro, J. L. G.; Vasudevan, P. T.; Cambra, J. F.; Guemez, M. B.; Arias, P. L., Dibenzothiophene hydrodesulfurization on HY-zeolite-supported transition metal sulfide catalysts. *Fuel Processing Technology* **1999,** *61* (1–2), 73-88.
63. Barrio, V. L.; Arias, P. L.; Cambra, J. F.; Güemez, M. B.; Pawelec, B.; Fierro, J. L. G., Modification of the Pd/SiO2–Al2O3 catalyst's thioresistance by the addition of a second metal (Pt, Ru, and Ni). *Catalysis Communications* **2004,** *5* (4), 173-178.
64. Al-Saleh, M. A.; Hossain, M. M.; Shalabi, M. A.; Kimura, T.; Inui, T., Hydrogen spillover effects on Pt–Rh modified Co–clay catalysts for heavy oil upgrading. *Applied Catalysis A: General* **2003,** *253* (2), 453-459.
65. Feuston, B. P.; Higgins, J. B., Model Structures for MCM-41 Materials: A Molecular Dynamics Simulation. *J. Phys. Chem.* **1994,** *98* (16), 4459-4462.
66. Coasne, B.; Galarneau, A.; Di Renzo, F.; Pellenq, R. J. M., Gas Adsorption in Mesoporous Micelle-Templated Silicas: MCM-41, MCM-48, and SBA-15. *Langmuir* **2006,** *22* (26), 11097-11105.
67. Liu, B.; Wang, D.; Wang, Z.; Zhao, Z.; Chen, Y.; Lan, J., The structure and activity of potassium supported on SBA-15 molecular sieve: Density functional theory study. *Journal of Theoretical and Computational Chemistry* **2014,** *13* (01), 1350076.
68. Sholl, D.; Steckel, J. A., *Density Functional Theory: A Practical Introduction*. Wiley: 2009.

69. Feuston, B. P.; Higgins, J. B., Model Structures for MCM-41 Materials: A Molecular Dynamics Simulation. *The Journal of Physical Chemistry* **1994,** *98* (16), 4459-4462.
70. Rozanska, X.; Delbecq, F.; Sautet, P., Reconstruction and stability of [small beta]-cristobalite 001, 101, and 111 surfaces during dehydroxylation. *Physical Chemistry Chemical Physics* **2010,** *12* (45), 14930-14940.
71. Li, W.-K.; Chu, L.-N.; Gong, X.-Q.; Lu, G., A comparative DFT study of adsorption and catalytic performance of Au nanoparticles at anatase and brookite TiO2 surfaces. *Surface Science* **2011,** *605* (15–16), 1369-1380.
72. Guesmi, H.; Tielens, F., Chromium Oxide Species Supported on Silica: A Representative Periodic DFT Model. *The Journal of Physical Chemistry C* **2012,** *116* (1), 994-1001.
73. Folliet, N.; Gervais, C.; Costa, D.; Laurent, G.; Babonneau, F.; Stievano, L.; Lambert, J.-F.; Tielens, F., A Molecular Picture of the Adsorption of Glycine in Mesoporous Silica through NMR Experiments Combined with DFT-D Calculations. *The Journal of Physical Chemistry C* **2013,** *117* (8), 4104-4114.
74. Feynman, R. P.; Leighton, R. B.; Sands, M. L., *The Feynman Lectures on Physics*. Pearson/Addison-Wesley: 1963.
75. Leach, A. R., *Molecular Modelling: Principles and Applications*. Prentice Hall: 2001.
76. McCallum, C. M., Statistical Mechanics: Fundamentals and Modern Applications (Wilde, Richard E.; Singh, Surjit). *Journal of Chemical Education* **1999,** *76* (6), 761.
77. McQuarrie, D. A., *Statistical Mechanics*. University Science Books: 2000.
78. Yoshioka, D., *Statistical Physics: An Introduction*. Springer: 2007.
79. Toton, D.; Lorenz, C. D.; Rompotis, N.; Martsinovich, N.; Kantorovich, L., Temperature control in molecular dynamic simulations of non-equilibrium processes. *Journal of Physics: Condensed Matter* **2010,** *22* (7), 074205.
80. Strachan, A. Molecular dynamics modeling of thermal and mechanical properties. http://www.mcc.uiuc.edu/summerschool/2006/presentations/Strachan_MD.ppt (accessed 24 june).
81. *Cerius2 User Guide*. Molecular Simulations Inc: San Diego, CA.
82. Brenner, D. W.; Shenderova, O. A.; Harrison, J. A.; Stuart, S. J.; Ni, B.; Sinnott, S. B., A second-generation reactive empirical bond order (REBO) potential energy expression for hydrocarbons. *Journal of Physics: Condensed Matter* **2002,** *14* (4), 783.
83. van Duin, A. C. T.; Dasgupta, S.; Lorant, F.; Goddard, W. A., ReaxFF: A Reactive Force Field for Hydrocarbons. *The Journal of Physical Chemistry A* **2001,** *105* (41), 9396-9409.
84. Rappe, A. K.; Casewit, C. J.; Colwell, K. S.; Goddard, W. A.; Skiff, W. M., UFF, a full periodic table force field for molecular mechanics and molecular dynamics simulations. *Journal of the American Chemical Society* **1992,** *114* (25), 10024-10035.
85. VASP code. http://www.vasp.at/.
86. Bachelet, G. B.; Hamann, D. R.; Schlüter, M., Pseudopotentials that work: From H to Pu. *Physical Review B* **1982,** *26* (8), 4199-4228.
87. Vanderbilt, D., Soft self-consistent pseudopotentials in a generalized eigenvalue formalism. *Physical Review B* **1990,** *41* (11), 7892-7895.
88. Blöchl, P. E., Projector augmented-wave method. *Physical Review B* **1994,** *50* (24), 17953-17979.
89. Marsman, M.; Kresse, G., Relaxed core projector-augmented-wave method. *The Journal of Chemical Physics* **2006,** *125* (10), 104101.
90. Monkhorst, H. J.; Pack, J. D., Special points for Brillouin-zone integrations. *Physical Review B* **1976,** *13* (12), 5188-5192.

91. Koekkoek, A. J. J.; van Veen, J. A. R.; Gerrtisen, P. B.; Giltay, P.; Magusin, P. C. M. M.; Hensen, E. J. M., Brønsted acidity of Al/SBA-15. *Microporous and Mesoporous Materials* **2012,** *151*, 34-43.
92. Tielens, F.; De Proft, F.; Geerlings, P., Density functional theory study of the conformation and energetics of silanol and disiloxane. *Journal of Molecular Structure: THEOCHEM* **2001,** *542* (1–3), 227-237.
93. Charif, I. E.; Mekelleche, S. M.; Villemin, D.; Mora-Diez, N., Correlation of aqueous pKa values of carbon acids with theoretical descriptors: A DFT study. *Journal of Molecular Structure: THEOCHEM* **2007,** *818* (1–3), 1-6.
94. Wang, C.-M.; Brogaard, R. Y.; Weckhuysen, B. M.; Nørskov, J. K.; Studt, F., Reactivity Descriptor in Solid Acid Catalysis: Predicting Turnover Frequencies for Propene Methylation in Zeotypes. *The Journal of Physical Chemistry Letters* **2014,** *5* (9), 1516-1521.
95. Bučko, T.; Hafner, J.; Benco, L., Adsorption and vibrational spectroscopy of ammonia at mordenite: Ab initio study. *The Journal of Chemical Physics* **2004,** *120* (21), 10263-10277.
96. Benco, L.; Bucko, T.; Hafner, J.; Toulhoat, H., Ab Initio Simulation of Lewis Sites in Mordenite and Comparative Study of the Strength of Active Sites via CO Adsorption. *The Journal of Physical Chemistry B* **2004,** *108* (36), 13656-13666.
97. Brändle, M.; Sauer, J., Acidity Differences between Inorganic Solids Induced by Their Framework Structure. A Combined Quantum Mechanics/Molecular Mechanics ab Initio Study on Zeolites. *Journal of the American Chemical Society* **1998,** *120* (7), 1556-1570.
98. Mihaleva, V. V.; van Santen, R. A.; Jansen, A. P. J., The heterogeneity of the hydroxyl groups in chabazite. *The Journal of Chemical Physics* **2003,** *119* (24), 13053-13060.
99. Demuth, T.; Hafner, J.; Benco, L.; Toulhoat, H., Structural and Acidic Properties of Mordenite. An ab Initio Density-Functional Study. *The Journal of Physical Chemistry B* **2000,** *104* (19), 4593-4607.
100. De Proft, F.; Van Alsenoy, C.; Peeters, A.; Langenaeker, W.; Geerlings, P., Atomic charges, dipole moments, and Fukui functions using the Hirshfeld partitioning of the electron density. *Journal of Computational Chemistry* **2002,** *23* (12), 1198-1209.
101. Bader, R. F. W., *Atoms in Molecules: A Quantum Theory*. Clarendon Press: 1990.
102. Heikkinen, O.; Pinto, H.; Sinha, G.; Hämäläinen, S. K.; Sainio, J.; Öberg, S.; Briddon, P. R.; Foster, A. S.; Lahtinen, J., Characterization of a Hexagonal Phosphorus Adlayer on Platinum (111). *Journal of Physical Chemistry C* **2015,** *119* (22), 12291-12297.
103. Kulish, V. V.; Malyi, O. I.; Persson, C.; Wu, P., Adsorption of metal adatoms on single-layer phosphorene. *Physical Chemistry Chemical Physics* **2015,** *17* (2), 992-1000.
104. Alex S. Côté, B. S. a. P. J. D. L. Democritus: A Molecular Dynamics tutorial http://www.ccp5.ac.uk/DL_POLY/Democritus/Basic/Democritus.html.
105. commission, E. Transport and environment http://ec.europa.eu/environment/air/transport/index.htm.
106. Lowenstein, W., The distribution of aluminium in the tetrahedra of silicates and aluminates. *American Mineralogist* **1954,** *39*, 92-96.
107. Pelmenschikov, A. G.; Paukshtis, E. A.; Edisherashvili, M. O.; Zhidomirov, G. M., On the Loewenstein rule and mechanism of zeolite dealumination. *The Journal of Physical Chemistry* **1992,** *96* (17), 7051-7055.

108. Yoshimura, Y.; Yasuda, H.; Sato, T.; Kijima, N.; Kameoka, T., Sulfur-tolerant Pd-Pt/Yb-USY zeolite catalysts used to reformulate diesel oils. *Applied Catalysis A: General* **2001,** *207* (1–2), 303-307.
109. Min, B. K.; Santra, A. K.; Goodman, D. W., Understanding silica-supported metal catalysts: Pd/silica as a case study. *Catalysis Today* **2003,** *85* (2–4), 113-124.
110. Moroz, È. M.; Kriventsov, V. V.; Kochubei, D. I., EuroPt-1 catalyst: Radial distribution of electron density X-ray diffraction and EXAFS studies. *J Struct Chem* **2009,** *50* (6), 1082-1087.
111. Schwartz, J. M.; Schmidt, L. D., Microstructures of Pt-Ce and Rh-Ce particles on alumina and silica. *Journal of Catalysis* **1992,** *138* (1), 283-293.
112. Campbell, C. T.; Sellers, J. R. V., Anchored metal nanoparticles: Effects of support and size on their energy, sintering resistance and reactivity. *Faraday Discussions* **2013,** *162* (0), 9-30.
113. Kleis, J.; Greeley, J.; Romero, N. A.; Morozov, V. A.; Falsig, H.; Larsen, A. H.; Lu, J.; Mortensen, J. J.; Dułak, M.; Thygesen, K. S.; Nørskov, J. K.; Jacobsen, K. W., Finite Size Effects in Chemical Bonding: From Small Clusters to Solids. *Catal Lett* **2011,** *141* (8), 1067-1071.
114. Mavrikakis, M.; Hammer, B.; Nørskov, J. K., Effect of Strain on the Reactivity of Metal Surfaces. *Physical Review Letters* **1998,** *81* (13), 2819-2822.
115. Stamatakis, M.; Christiansen, M. A.; Vlachos, D. G.; Mpourmpakis, G., Multiscale Modeling Reveals Poisoning Mechanisms of MgO-Supported Au Clusters in CO Oxidation. *Nano Letters* **2012,** *12* (7), 3621-3626.
116. Frantz, J. *g3data*, 1.5.2; 2000.
117. Staroverov, V. N., Density-Functional Approximations for Exchange and Correlation. In *A Matter of Density*, John Wiley & Sons, Inc.: 2012; pp 125-156.
118. Kresse, G.; Joubert, D., From ultrasoft pseudopotentials to the projector augmented-wave method. *Physical Review B* **1999,** *59* (3), 1758-1775.
119. Ramos-Sanchez, G.; Praserthdam, S.; Godinez-Salomon, F.; Barker, C.; Moerbe, M.; Calderon, H. A.; Lartundo, L. A.; Leyva, M. A.; Solorza-Feria, O.; Balbuena, P. B., Challenges of modelling real nanoparticles: Ni@Pt electrocatalysts for the oxygen reduction reaction. *Physical Chemistry Chemical Physics* **2015**.
120. Imaoka, T.; Kitazawa, H.; Chun, W.-J.; Omura, S.; Albrecht, K.; Yamamoto, K., Magic Number Pt13 and Misshapen Pt12 Clusters: Which One is the Better Catalyst? *Journal of the American Chemical Society* **2013,** *135* (35), 13089-13095.
121. Grimley, D. I.; Wright, A. C.; Sinclair, R. N., Neutron scattering from vitreous silica IV. Time-of-flight diffraction. *Journal of Non-Crystalline Solids* **1990,** *119* (1), 49-64.
122. Mozzi, R. L.; Warren, B. E., The structure of vitreous silica. *Journal of Applied Crystallography* **1969,** *2* (4), 164-172.
123. Da Silva, J. R. G.; Pinatti, D. G.; Anderson, C. E.; Rudee, M. L., A refinement of the structure of vitreous silica. *Philosophical Magazine* **1975,** *31* (3), 713-717.
124. Durig, J. R.; Flanagan, M. J.; Kalasinsky, V. F., The determination of the potential function governing the low frequency bending mode of disiloxane. *Journal of Chemical Physics* **1977,** *66* (7), 2775-2785.
125. A. Almenningen, O. B., V. Ewing, K. Hedberg and M. Tretteberg, The molecular structure of Disiloxane, (SiH3)2O. *Acta Chemica Scandinavica* **1963,** *17*, 2455-2460.
126. Arrouvel, C.; Toulhoat, H.; Breysse, M.; Raybaud, P., Effects of PH2O, PH2S, PH2 on the surface properties of anatase–TiO2 and γ-Al2O3: a DFT study. *Journal of Catalysis* **2004,** *226* (2), 260-272.

127. Daughtridge, K., gElemental 1.2.0: A periodic table viewer with detailed information on elements. **2007**.
128. Sierka, M.; Eichler, U.; Datka, J.; Sauer, J., Heterogeneity of Brønsted Acidic Sites in Faujasite Type Zeolites due to Aluminum Content and Framework Structure. *The Journal of Physical Chemistry B* **1998,** *102* (33), 6397-6404.
129. Zecchina, A.; Bordiga, S.; Spoto, G.; Marchese, L.; Petrini, G.; Leofanti, G.; Padovan, M., Silicalite characterization. 2. IR spectroscopy of the interaction of carbon monoxide with internal and external hydroxyl groups. *The Journal of Physical Chemistry* **1992,** *96* (12), 4991-4997.
130. Su, B.-L.; Norberg, V., Quantitative characterisation of H-Mordenite zeolite structure by infrared spectroscopy using benzene adsorption. *Colloids and Surfaces A: Physicochemical and Engineering Aspects* **2001,** *187–188*, 311-318.
131. BDEs of Ni(Ni ±)-, Pd(Pd ±)-, and Pt(Pt ±)-X bonds. In *Comprehensive Handbook of Chemical Bond Energies*, CRC Press: 2007; pp 903-966.
132. Wallace, W. T.; Whetten, R. L., Carbon Monoxide Adsorption on Selected Gold Clusters: Highly Size-Dependent Activity and Saturation Compositions. *The Journal of Physical Chemistry B* **2000,** *104* (47), 10964-10968.

BIBLIOGRAPHY

A, Almenningen, O. B., V. Ewing, K. Hedberg and M. Tretteberg, The molecular structure of Disiloxane, (SiH3)2O. *Acta Chemica Scandinavica* **1963,** *17*, 2455-2460.

Alex S Côté, B. S. a. P. J. D. L. Democritus: A Molecular Dynamics tutorial http://www.ccp5.ac.uk/DL_POLY/Democritus/Basic/Democritus.html.

Al-Saleh, M. A.; Hossain, M. M.; Shalabi, M. A.; Kimura, T.; Inui, T., Hydrogen spillover effects on Pt–Rh modified Co–clay catalysts for heavy oil upgrading. *Applied Catalysis A: General* **2003,** *253* (2), 453-459.

Ancheyta, J.; Rana, M. S.; Furimsky, E., Hydroprocessing of heavy oil fractions. *Catalysis Today* **2005,** *109* (1–4), 1-2.

Arrouvel, C.; Breysse, M.; Toulhoat, H.; Raybaud, P., A density functional theory comparison of anatase (TiO2)- and γ-Al2O3-supported MoS2 catalysts. *Journal of Catalysis* **2005,** *232* (1), 161-178.

Arrouvel, C.; Toulhoat, H.; Breysse, M.; Raybaud, P., Effects of PH2O, PH2S, PH2 on the surface properties of anatase–TiO2 and γ-Al2O3: a DFT study. *Journal of Catalysis* **2004,** *226* (2), 260-272.

Bachelet, G. B.; Hamann, D. R.; Schlüter, M., Pseudopotentials that work: From H to Pu. *Physical Review B* **1982,** *26* (8), 4199-4228.

Bader, R. F. W., *Atoms in Molecules: A Quantum Theory*. Clarendon Press: 1990.

Barrio, V. L.; Arias, P. L.; Cambra, J. F.; Güemez, M. B.; Pawelec, B.; Fierro, J. L. G., Modification of the Pd/SiO2–Al2O3 catalyst's thioresistance by the addition of a second metal (Pt, Ru, and Ni). *Catalysis Communications* **2004,** *5* (4), 173-178.

BDEs of Ni(Ni ±)-, Pd(Pd ±)-, and Pt(Pt ±)-X bonds. In *Comprehensive Handbook of Chemical Bond Energies*, CRC Press: 2007; pp 903-966.

Benamor, T.; Vidal, L.; Lebeau, B.; Marichal, C., Influence of synthesis parameters on the physico-chemical characteristics of SBA-15 type ordered mesoporous silica. *Microporous and Mesoporous Materials* **2012,** *153* (0), 100-114.

Benco, L.; Bucko, T.; Hafner, J.; Toulhoat, H., Ab Initio Simulation of Lewis Sites in Mordenite and Comparative Study of the Strength of Active Sites via CO Adsorption. *The Journal of Physical Chemistry B* **2004,** *108* (36), 13656-13666.

Benesi, H. A.; Winquist, B. H. C., Surface Acidity of Solid Catalysts. In *Advances in Catalysis*, D.D. Eley, H. P.; Paul, B. W., Eds. Academic Press: 1979; Vol. Volume 27, pp 97-182.

Blöchl, P. E., Projector augmented-wave method. *Physical Review B* **1994,** *50* (24), 17953-17979.

Boahene, P. E.; Soni, K. K.; Dalai, A. K.; Adjaye, J., Application of different pore diameter SBA-15 supports for heavy gas oil hydrotreatment using FeW catalyst. *Applied Catalysis A: General* **2011,** *402* (1–2), 31-40.

Brändle, M.; Sauer, J., Acidity Differences between Inorganic Solids Induced by Their Framework Structure. A Combined Quantum Mechanics/Molecular Mechanics ab Initio Study on Zeolites. *Journal of the American Chemical Society* **1998,** *120* (7), 1556-1570.

Brenner, D. W.; Shenderova, O. A.; Harrison, J. A.; Stuart, S. J.; Ni, B.; Sinnott, S. B., A second-generation reactive empirical bond order (REBO) potential energy expression for hydrocarbons. *Journal of Physics: Condensed Matter* **2002,** *14* (4), 783.

Bucko, T.; Benco, L.; Demuth, T.; Hafner, J., Ab initio density functional investigation of the (001) surface of mordenite. *The Journal of Chemical Physics* **2002,** *117* (15), 7295-7305.

Bučko, T.; Hafner, J.; Benco, L., Adsorption and vibrational spectroscopy of ammonia at mordenite: Ab initio study. *The Journal of Chemical Physics* **2004,** *120* (21), 10263-10277.

Byambajav, E.; Ohtsuka, Y., Hydrocracking of asphaltene with metal catalysts supported on SBA-15. *Applied Catalysis A: General* **2003,** *252* (1), 193-204.

Campbell, C. T.; Sellers, J. R. V., Anchored metal nanoparticles: Effects of support and size on their energy, sintering resistance and reactivity. *Faraday Discussions* **2013,** *162* (0), 9-30.

Carter, E. A., Challenges in Modeling Materials Properties Without Experimental Input. *Science* **2008,** *321* (5890), 800-803.

Cerius2 User Guide. Molecular Simulations Inc: San Diego, CA.

Chandra Mouli, K.; Soni, K.; Dalai, A.; Adjaye, J., Effect of pore diameter of Ni–Mo/Al-SBA-15 catalysts on the hydrotreating of heavy gas oil. *Applied Catalysis A: General* **2011,** *404* (1–2), 21-29.

Chao, M.-C.; Chang, C.-H.; Lin, H.-P.; Tang, C.-Y.; Lin, C.-Y., Morphological control on SBA-15 mesoporous silicas via a slow self-assembling rate. *J. Mater. Sci.* **2009,** *44* (24), 6453-6462.

Charif, I. E.; Mekelleche, S. M.; Villemin, D.; Mora-Diez, N., Correlation of aqueous pKa values of carbon acids with theoretical descriptors: A DFT study. *Journal of Molecular Structure: THEOCHEM* **2007,** *818* (1–3), 1-6.

Chill, W. T. a. S. Bader Charge Analysis. http://theory.cm.utexas.edu/henkelman/research/bader/.

Choi, M.; Heo, W.; Kleitz, F.; Ryoo, R., Facile synthesis of high quality mesoporous SBA-15 with enhanced control of the porous network connectivity and wall thickness. *Chemical Communications* **2003,** (12), 1340-1341.

Coasne, B.; Galarneau, A.; Di Renzo, F.; Pellenq, R. J. M., Gas Adsorption in Mesoporous Micelle-Templated Silicas: MCM-41, MCM-48, and SBA-15. *Langmuir* **2006,** *22* (26), 11097-11105.

Commission, E. Transport and environment http://ec.europa.eu/environment/air/transport/index.htm.

Da Silva, J. R. G.; Pinatti, D. G.; Anderson, C. E.; Rudee, M. L., A refinement of the structure of vitreous silica. *Philosophical Magazine* **1975,** *31* (3), 713-717.

Daughtridge, K., gElemental 1.2.0: A periodic table viewer with detailed information on elements. **2007**.

De Proft, F.; Van Alsenoy, C.; Peeters, A.; Langenaeker, W.; Geerlings, P., Atomic charges, dipole moments, and Fukui functions using the Hirshfeld partitioning of the electron density. *Journal of Computational Chemistry* **2002,** *23* (12), 1198-1209.

Demuth, T.; Hafner, J.; Benco, L.; Toulhoat, H., Structural and Acidic Properties of Mordenite. An ab Initio Density-Functional Study. *The Journal of Physical Chemistry B* **2000,** *104* (19), 4593-4607.

Ding, L.; Zheng, Y.; Yang, H.; Parviz, R., LCO hydrotreating with Mo-Ni and W-Ni supported on nano- and micro-sized zeolite beta. *Applied Catalysis A: General* **2009,** *353* (1), 17-23.

Durig, J. R.; Flanagan, M. J.; Kalasinsky, V. F., The determination of the potential function governing the low frequency bending mode of disiloxane. *Journal of Chemical Physics* **1977,** *66* (7), 2775-2785.

Esquivel, G. M.; Ramírez, J.; Gutiérrez-Alejandre, A., HDS of 4,6-DMDBT over NiW/Al-SBA15 catalysts. *Catal. Today* **2009,** *148* (1–2), 36-41.

Ewing, C. S.; Bhavsar, S.; Veser, G.; McCarthy, J. J.; Johnson, J. K., Accurate Amorphous Silica Surface Models from First-Principles Thermodynamics of Surface Dehydroxylation. *Langmuir* **2014,** *30* (18), 5133-5141.

Ewing, C. S.; Hartmann, M. J.; Martin, K. R.; Musto, A. M.; Padinjarekutt, S. J.; Weiss, E. M.; Veser, G.; McCarthy, J. J.; Johnson, J. K.; Lambrecht, D. S., Structural and Electronic Properties of Pt13 Nanoclusters on Amorphous Silica Supports. *The Journal of Physical Chemistry C* **2015,** *119* (5), 2503-2512.

Fedeyko, J. M.; Vlachos, D. G.; Lobo, R. F., Understanding the differences between microporous and mesoporous synthesis through the phase behavior of silica. *Microporous and Mesoporous Materials* **2006,** *90* (1–3), 102-111.

Feuston, B. P.; Higgins, J. B., Model Structures for MCM-41 Materials: A Molecular Dynamics Simulation. *J. Phys. Chem.* **1994,** *98* (16), 4459-4462.

Feuston, B. P.; Higgins, J. B., Model Structures for MCM-41 Materials: A Molecular Dynamics Simulation. *The Journal of Physical Chemistry* **1994,** *98* (16), 4459-4462.

Feynman, R. P.; Leighton, R. B.; Sands, M. L., *The Feynman Lectures on Physics*. Pearson/Addison-Wesley: 1963.

Folliet, N.; Gervais, C.; Costa, D.; Laurent, G.; Babonneau, F.; Stievano, L.; Lambert, J.-F.; Tielens, F., A Molecular Picture of the Adsorption of Glycine in

Mesoporous Silica through NMR Experiments Combined with DFT-D Calculations. *The Journal of Physical Chemistry C* **2013,** *117* (8), 4104-4114.

Frantz, J. *g3data*, 1.5.2; 2000.

Furimsky, E.; Massoth, F. E., Deactivation of hydroprocessing catalysts. *Catalysis Today* **1999,** *52* (4), 381-495.

Garg, S.; Soni, K.; Kumaran, G. M.; Kumar, M.; Gupta, J. K.; Sharma, L. D.; Dhar, G. M., Effect of Zr-SBA-15 support on catalytic functionalities of Mo, CoMo, NiMo hydrotreating catalysts. *Catal. Today* **2008,** *130* (2–4), 302-308.

Gómez-Cazalilla, M.; Infantes-Molina, A.; Moreno-Tost, R.; Maireles-Torres, P. J.; Mérida-Robles, J.; Rodríguez-Castellón, E.; Jiménez-López, A., Al-SBA-15 as a support of catalysts based on chromium sulfide for sulfur removal. *Catal. Today* **2009,** *143* (1–2), 137-144.

Grimley, D. I.; Wright, A. C.; Sinclair, R. N., Neutron scattering from vitreous silica IV. Time-of-flight diffraction. *Journal of Non-Crystalline Solids* **1990,** *119* (1), 49-64.

Guesmi, H.; Tielens, F., Chromium Oxide Species Supported on Silica: A Representative Periodic DFT Model. *The Journal of Physical Chemistry C* **2012,** *116* (1), 994-1001.

Hafner, J., Materials simulations using VASP—a quantum perspective to materials science. *Computer Physics Communications* **2007,** *177* (1–2), 6-13.

Hafner, J.; Benco, L.; Bučko, T., Acid-based Catalysis in Zeolites Investigated by Density-Functional Methods. *Top Catal* **2006,** *37* (1), 41-54.

Hansen, N.; Keil, F. J., Multiscale Modeling of Reaction and Diffusion in Zeolites: From the Molecular Level to the Reactor. *Soft Materials* **2011,** *10* (1-3), 179-201.

Hanwell, M.; Curtis, D.; Lonie, D.; Vandermeersch, T.; Zurek, E.; Hutchison, G., Avogadro: an advanced semantic chemical editor, visualization, and analysis platform. *J Cheminform* **2012,** *4* (1), 1-17.

Heikkinen, O.; Pinto, H.; Sinha, G.; Hämäläinen, S. K.; Sainio, J.; Öberg, S.; Briddon, P. R.; Foster, A. S.; Lahtinen, J., Characterization of a Hexagonal Phosphorus Adlayer on Platinum (111). *Journal of Physical Chemistry C* **2015,** *119* (22), 12291-12297.

Henkelman, G.; Arnaldsson, A.; Jónsson, H., A fast and robust algorithm for Bader decomposition of charge density. *Computational Materials Science* **2006,** *36* (3), 354-360.

Huang, L.; Huang, Q.; Xiao, H.; Eic, M., Al-MCM-48 as a potential hydrotreating catalyst support: I – Synthesis and adsorption study. *Microporous and Mesoporous Materials* **2008,** *111* (1–3), 404-410.

Huirache-Acuña, R.; Nava, R.; Peza-Ledesma, C.; Lara-Romero, J.; Alonso-Núez, G.; Pawelec, B.; Rivera-Muñoz, E., SBA-15 Mesoporous Silica as Catalytic Support for Hydrodesulfurization Catalysts—Review. *Materials* **2013,** *6* (9), 4139-4167.

Imaoka, T.; Kitazawa, H.; Chun, W.-J.; Omura, S.; Albrecht, K.; Yamamoto, K., Magic Number Pt13 and Misshapen Pt12 Clusters: Which One is the Better Catalyst? *Journal of the American Chemical Society* **2013,** *135* (35), 13089-13095.

Islam, M. M.; Costa, D.; Calatayud, M.; Tielens, F., Characterization of Supported Vanadium Oxide Species on Silica: A Periodic DFT Investigation. *The Journal of Physical Chemistry C* **2009,** *113* (24), 10740-10746.

Kanda, Y.; Aizawa, T.; Kobayashi, T.; Uemichi, Y.; Namba, S.; Sugioka, M., Preparation of highly active AlSBA-15-supported platinum catalyst for thiophene hydrodesulfurization. *Applied Catalysis B: Environmental* **2007,** *77* (1–2), 117-124.

Keil, F. J., Complexities in modeling of heterogeneous catalytic reactions. *Computers & Mathematics with Applications* **2013,** *65* (10), 1674-1697.

Kleis, J.; Greeley, J.; Romero, N. A.; Morozov, V. A.; Falsig, H.; Larsen, A. H.; Lu, J.; Mortensen, J. J.; Dułak, M.; Thygesen, K. S.; Nørskov, J. K.; Jacobsen, K. W., Finite Size Effects in Chemical Bonding: From Small Clusters to Solids. *Catal Lett* **2011,** *141* (8), 1067-1071.

Klimova, T.; Peña, L.; Lizama, L.; Salcedo, C.; Gutiérrez, O. Y., Modification of Activity and Selectivity of NiMo/SBA-15 HDS Catalysts by Grafting of Different Metal Oxides on the Support Surface. *Industrial & Engineering Chemistry Research* **2009,** *48* (3), 1126-1133.

Klimova, T.; Reyes, J.; Gutiérrez, O.; Lizama, L., Novel bifunctional NiMo/Al-SBA-15 catalysts for deep hydrodesulfurization: Effect of support Si/Al ratio. *Applied Catalysis A: General* **2008,** *335* (2), 159-171.

Koch, W.; Holthausen, M. C.; Baerends, E. J., *A Chemist's Guide to Density Functional Theory*. FVA-Frankfurter Verlagsanstalt GmbH: 2001.

Koekkoek, A. J. J.; van Veen, J. A. R.; Gerrtisen, P. B.; Giltay, P.; Magusin, P. C. M. M.; Hensen, E. J. M., Brønsted acidity of Al/SBA-15. *Microporous and Mesoporous Materials* **2012,** *151*, 34-43.

Kresse, G.; Furthmüller, J., Efficiency of ab-initio total energy calculations for metals and semiconductors using a plane-wave basis set. *Computational Materials Science* **1996,** *6* (1), 15-50.

Kresse, G.; Furthmüller, J., Efficient iterative schemes for \textit{ab initio} total-energy calculations using a plane-wave basis set. *Physical Review B* **1996,** *54* (16), 11169-11186.

Kresse, G.; Joubert, D., From ultrasoft pseudopotentials to the projector augmented-wave method. *Physical Review B* **1999,** *59* (3), 1758-1775.

Kruk, M.; Jaroniec, M.; Ko, C. H.; Ryoo, R., Characterization of the Porous Structure of SBA-15. *Chemistry of Materials* **2000,** *12* (7), 1961-1968.

Kulish, V. V.; Malyi, O. I.; Persson, C.; Wu, P., Adsorption of metal adatoms on single-layer phosphorene. *Physical Chemistry Chemical Physics* **2015,** *17* (2), 992-1000.

Leach, A. R., *Molecular Modelling: Principles and Applications*. Prentice Hall: 2001.

Lee, J. G., *Computational Materials Science: An Introduction*. Taylor & Francis: 2011.

Lei, Z.; Gao, L.; Shui, H.; Chen, W.; Wang, Z.; Ren, S., Hydrotreatment of heavy oil from a direct coal liquefaction process on sulfided Ni–W/SBA-15 catalysts. *Fuel Processing Technology* **2011,** *92* (10), 2055-2060.

Li, W.-K.; Chu, L.-N.; Gong, X.-Q.; Lu, G., A comparative DFT study of adsorption and catalytic performance of Au nanoparticles at anatase and brookite TiO2 surfaces. *Surface Science* **2011,** *605* (15–16), 1369-1380.

Liu, B.; Wang, D.; Wang, Z.; Zhao, Z.; Chen, Y.; Lan, J., The structure and activity of potassium supported on SBA-15 molecular sieve: Density functional theory study. *Journal of Theoretical and Computational Chemistry* **2014,** *13* (01), 1350076.

Lowenstein, W., The distribution of aluminium in the tetrahedra of silicates and aluminates. *American Mineralogist* **1954,** *39*, 92-96.

Maclachlan, M. J.; Shopsowitz, K. E.; Hamad, W. Y.; Qi, H., Inorganic mesoporous materials with chiral nematic structures and preparation method thereof. Google Patents: 2011.

Maity, S. K.; Blanco, E.; Ancheyta, J.; Alonso, F.; Fukuyama, H., Early stage deactivation of heavy crude oil hydroprocessing catalysts. *Fuel* **2012,** *100*, 17-23.

Marsman, M.; Kresse, G., Relaxed core projector-augmented-wave method. *The Journal of Chemical Physics* **2006,** *125* (10), 104101.

Martinez, U.; Pacchioni, G., Interaction of CO, CO2 and CH4 with mesoporous organosilica: Periodic DFT calculations with dispersion corrections. *Microporous and Mesoporous Materials* **2010,** *129* (1–2), 62-67.

Mavrikakis, M.; Hammer, B.; Nørskov, J. K., Effect of Strain on the Reactivity of Metal Surfaces. *Physical Review Letters* **1998,** *81* (13), 2819-2822.

McCallum, C. M., Statistical Mechanics: Fundamentals and Modern Applications (Wilde, Richard E.; Singh, Surjit). *Journal of Chemical Education* **1999,** *76* (6), 761.

McQuarrie, D. A., *Statistical Mechanics*. University Science Books: 2000.

Mihaleva, V. V.; van Santen, R. A.; Jansen, A. P. J., The heterogeneity of the hydroxyl groups in chabazite. *The Journal of Chemical Physics* **2003,** *119* (24), 13053-13060.

Min, B. K.; Santra, A. K.; Goodman, D. W., Understanding silica-supported metal catalysts: Pd/silica as a case study. *Catalysis Today* **2003,** *85* (2–4), 113-124.

Monkhorst, H. J.; Pack, J. D., Special points for Brillouin-zone integrations. *Physical Review B* **1976,** *13* (12), 5188-5192.

Moroz, È. M.; Kriventsov, V. V.; Kochubei, D. I., EuroPt-1 catalyst: Radial distribution of electron density X-ray diffraction and EXAFS studies. *J Struct Chem* **2009,** *50* (6), 1082-1087.

Mozzi, R. L.; Warren, B. E., The structure of vitreous silica. *Journal of Applied Crystallography* **1969,** *2* (4), 164-172.

Nava, R.; Ortega, R. A.; Alonso, G.; Ornelas, C.; Pawelec, B.; Fierro, J. L. G., CoMo/Ti-SBA-15 catalysts for dibenzothiophene desulfurization. *Catalysis Today* **2007,** *127* (1–4), 70-84.

Navarro, R.; Pawelec, B.; Fierro, J. L. G.; Vasudevan, P. T.; Cambra, J. F.; Guemez, M. B.; Arias, P. L., Dibenzothiophene hydrodesulfurization on HY-zeolite-supported transition metal sulfide catalysts. *Fuel Processing Technology* **1999,** *61* (1–2), 73-88.

Okamoto, Y.; Breysse, M.; Murali Dhar, G.; Song, C., Effect of support in hydrotreating catalysis for ultra clean fuels. *Catalysis Today* **2003,** *86* (1–4), 1-3.

Olivas, A.; Zepeda, T. A., Impact of Al and Ti ions on the dispersion and performance of supported NiMo(W)/SBA-15 catalysts in the HDS and HYD reactions. *Catalysis Today* **2009,** *143* (1–2), 120-125.

Pelmenschikov, A. G.; Paukshtis, E. A.; Edisherashvili, M. O.; Zhidomirov, G. M., On the Loewenstein rule and mechanism of zeolite dealumination. *The Journal of Physical Chemistry* **1992,** *96* (17), 7051-7055.

Perdew, J. P.; Burke, K.; Ernzerhof, M., Generalized Gradient Approximation Made Simple. *Physical Review Letters* **1996,** *77* (18), 3865-3868.

Rahmat, N., A.Z. Abdullah and A.R. Mohamed, A review: Mesoporous santa barbara amorphous-15, types, synthesis and its applications towards biorefinery production. *American Journal of Applied Sciences* **2010,** *7* (12), 1579 - 1586.

Ramos-Sanchez, G.; Praserthdam, S.; Godinez-Salomon, F.; Barker, C.; Moerbe, M.; **Calderon, H. A.**; Lartundo, L. A.; Leyva, M. A.; Solorza-Feria, O.; Balbuena, P.

B., Challenges of modelling real nanoparticles: Ni@Pt electrocatalysts for the oxygen reduction reaction. *Physical Chemistry Chemical Physics* **2015**.

Rappe, A. K.; Casewit, C. J.; Colwell, K. S.; Goddard, W. A.; Skiff, W. M., UFF, a full periodic table force field for molecular mechanics and molecular dynamics simulations. *Journal of the American Chemical Society* **1992,** *114* (25), 10024-10035.

Rayo, P.; Ramírez, J.; Torres-Mancera, P.; Marroquín, G.; Maity, S. K.; Ancheyta, J., Hydrodesulfurization and hydrocracking of Maya crude with P-modified NiMo/Al2O3 catalysts. *Fuel* **2012,** *100*, 34-42.

Rozanska, X.; Delbecq, F.; Sautet, P., Reconstruction and stability of [small beta]-cristobalite 001, 101, and 111 surfaces during dehydroxylation. *Physical Chemistry Chemical Physics* **2010,** *12* (45), 14930-14940.

Salvi, B. L.; Subramanian, K. A.; Panwar, N. L., Alternative fuels for transportation vehicles: A technical review. *Renewable and Sustainable Energy Reviews* **2013,** *25*, 404-419.

Schutte, C. J. H.; Pretorius, J. A., *A computational study of the molecular and crystal structure and selected physical properties of octahydridosilasequioxane–(Si2O3H2)4. I. Electronic and structural aspects*. 2011; Vol. 467, p 928-953.

Schwartz, J. M.; Schmidt, L. D., Microstructures of Pt-Ce and Rh-Ce particles on alumina and silica. *Journal of Catalysis* **1992,** *138* (1), 283-293.

Sholl, D.; Steckel, J. A., *Density Functional Theory: A Practical Introduction*. Wiley: 2009.

Sierka, M.; Eichler, U.; Datka, J.; Sauer, J., Heterogeneity of Brønsted Acidic Sites in Faujasite Type Zeolites due to Aluminum Content and Framework Structure. *The Journal of Physical Chemistry B* **1998,** *102* (33), 6397-6404.

Stamatakis, M.; Christiansen, M. A.; Vlachos, D. G.; Mpourmpakis, G., Multiscale Modeling Reveals Poisoning Mechanisms of MgO-Supported Au Clusters in CO Oxidation. *Nano Letters* **2012,** *12* (7), 3621-3626.

Staroverov, V. N., Density-Functional Approximations for Exchange and Correlation. In *A Matter of Density*, John Wiley & Sons, Inc.: 2012; pp 125-156.

Strachan, A. Molecular dynamics modeling of thermal and mechanical properties. http://www.mcc.uiuc.edu/summerschool/2006/presentations/Strachan_MD.ppt (accessed 24 june).

Su, B. L.; Norberg, V., Quantitative characterisation of H-Mordenite zeolite structure by infrared spectroscopy using benzene adsorption. *Colloids and Surfaces A: Physicochemical and Engineering Aspects* **2001,** *187–188*, 311-318.

Sugioka, M.; Aizawa, T.; Kanda, Y.; Kurosaka, T.; Uemichi, Y.; Namba, S., Catalytic performance of mesoporous silica SBA-15-supported noble metals for thiophene hydrodesulfurization. In *Studies in Surface Science and Catalysis*, R. Aiello, G. G.; **Testa, F.**, Eds. Elsevier: 2002; Vol. Volume 142, pp 739-746.

Sundaramurthy, V.; Eswaramoorthi, I.; Dalai, A. K.; Adjaye, J., Hydrotreating of gas oil on SBA-15 supported NiMo catalysts. *Microporous and Mesoporous Materials* **2008,** *111* (1–3), 560-568.

Taguchi, A.; Schüth, F., Ordered mesoporous materials in catalysis. *Microporous and Mesoporous Materials* **2005,** *77* (1), 1-45.

Tang, Y. N.; Li, C. G.; Chen, W. G.; Dai, X. Q., Geometric Stability, Electronic Structure and Reactivity of Pt <inf>4</inf> Cluster Supported On Defective Graphene. *Integrated Ferroelectrics* **2015,** *159* (1), 57-65.

Tielens, F.; De Proft, F.; Geerlings, P., Density functional theory study of the conformation and energetics of silanol and disiloxane. *Journal of Molecular Structure: THEOCHEM* **2001,** *542* (1–3), 227-237.

Tielens, F.; Gervais, C.; Lambert, J. F.; Mauri, F.; Costa, D., Ab Initio Study of the Hydroxylated Surface of Amorphous Silica: A Representative Model. *Chemistry of Materials* **2008,** *20* (10), 3336-3344.

Toton, D.; Lorenz, C. D.; Rompotis, N.; Martsinovich, N.; Kantorovich, L., Temperature control in molecular dynamic simulations of non-equilibrium processes. *Journal of Physics: Condensed Matter* **2010,** *22* (7), 074205.

Tsybukh, R. A comparative study of platinum nanodeposits on HOPG (0001), MnO(100) and MnOx/MnO(100) surfaces by STM and AFM after heat treatment in UHV, O2 , CO and H2. Leiden University, Netherlands, 2010.

Union, Europea. Fuel Regulations European Union. https://www.dieselnet.com/standards/eu/fuel.php#intro (accessed 2015).

Van Duin, A. C. T.; Dasgupta, S.; Lorant, F.; Goddard, W. A., ReaxFF: A Reactive Force Field for Hydrocarbons. *The Journal of Physical Chemistry A* **2001,** *105* (41), 9396-9409.

Vanderbilt, D., Soft self-consistent pseudopotentials in a generalized eigenvalue formalism. *Physical Review B* **1990,** *41* (11), 7892-7895.

VASP code. http://www.vasp.at/.

Wallace, W. T.; Whetten, R. L., Carbon Monoxide Adsorption on Selected Gold Clusters: Highly Size-Dependent Activity and Saturation Compositions. *The Journal of Physical Chemistry B* **2000,** *104* (47), 10964-10968.

Wang, C.-M.; Brogaard, R. Y.; Weckhuysen, B. M.; Nørskov, J. K.; Studt, F., Reactivity Descriptor in Solid Acid Catalysis: Predicting Turnover Frequencies for Propene Methylation in Zeotypes. *The Journal of Physical Chemistry Letters* **2014,** *5* (9), 1516-1521.

Wang, Z.; Wang, D.; Zhao, Z.; Chen, Y.; Lan, J., A DFT study of the structural units in SBA-15 mesoporous molecular sieve. *Computational and Theoretical Chemistry* **2011,** *963* (2–3), 403-411.

Yoshimura, Y.; Yasuda, H.; Sato, T.; Kijima, N.; Kameoka, T., Sulfur-tolerant Pd-Pt/Yb-USY zeolite catalysts used to reformulate diesel oils. *Applied Catalysis A: General* **2001,** *207* (1–2), 303-307.

Yoshioka, D., *Statistical Physics: An Introduction*. Springer: 2007.

Zecchina, A.; Bordiga, S.; Spoto, G.; Marchese, L.; Petrini, G.; Leofanti, G.; Padovan, M., Silicalite characterization. 2. IR spectroscopy of the interaction of carbon monoxide with internal and external hydroxyl groups. *The Journal of Physical Chemistry* **1992,** *96* (12), 4991-4997.

Zhang, P.; Zhou, Y.; Fan, M.; Jiang, P., Catalytic performance of PdCl2/Cu-HMS: Influence of hydrophobicity and structure of molecular sieves. *Applied Surface Science* **2014,** *295*, 50-53.

Zhao, D.; Feng, J.; Huo, Q.; Melosh, N.; Fredrickson, G. H.; Chmelka, B. F.; Stucky, G. D., Triblock Copolymer Syntheses of Mesoporous Silica with Periodic 50 to 300 Angstrom Pores. *Science* **1998,** *279* (5350), 548-552.

Zhao, D.; Huo, Q.; Feng, J.; Chmelka, B. F.; Stucky, G. D., Nonionic Triblock and Star Diblock Copolymer and Oligomeric Surfactant Syntheses of Highly Ordered, Hydrothermally Stable, Mesoporous Silica Structures. *J. Am. Chem. Soc.* **1998,** *120* (24), 6024-6036.

Zhuravlev, L. T., The surface chemistry of amorphous silica. Zhuravlev model. *Colloids and Surfaces A: Physicochemical and Engineering Aspects* **2000,** *173* (1–3), 1-38.